Fiber-Optic-Based Laser Vapor Screen Flow Visualization System for Aerodynamic Research in Larger Scale Subsonic and Transonic Wind Tunnels

Gary E. Erickson and Andrew S. Inenaga

Fiber-Optic-Based Laser Vapor Screen Flow Visualization System for Aerodynamic Research in Larger Scale Subsonic and Transonic Wind Tunnels

Gary E. Erickson
Langley Research Center • Hampton, Virginia

Andrew S. Inenaga
Aerometrics, Inc. • Sunnyvale, California

National Aeronautics and
Space Administration
Code JTT
Washington, D.C.
20546-0001

Abstract

Laser vapor screen (LVS) flow visualization systems that are fiber-optic based have been developed and installed for aerodynamic research in the Langley 8-Foot Transonic Pressure Tunnel and the Langley 7- by 10-Foot High-Speed Tunnel. Fiber optics are used to deliver the laser beam through the plenum shell that surrounds the test section of each facility and to the light-sheet-generating optics positioned in the ceiling window of the test section. Water is injected into the wind tunnel diffuser section to increase the relative humidity and promote condensation of the water vapor in the flow field about the model. The condensed water vapor is then illuminated with an intense sheet of laser light to reveal features of the flow field. The plenum shells are optically sealed; therefore, video-based systems are used to observe and document the flow field. Operational experience shows that the fiber-optic-based systems provide safe, reliable, and high-quality off-surface flow visualization in smaller and larger scale subsonic and transonic wind tunnels. The design, the installation, and the application of the Langley Research Center (LaRC) LVS flow visualization systems in larger scale wind tunnels are highlighted in the present paper. The efficiency of the fiber optic LVS systems and their insensitivity to wind tunnel vibration, the tunnel operating temperature and pressure variations, and the airborne contaminants are discussed.

Introduction

The laser vapor screen (LVS) method of flow visualization was first employed in 1951 in the National Advisory Committee for Aeronautics (NACA) 1- by 3-Foot Supersonic Wind Tunnels at the Ames Aeronautical Laboratory to study the vortical flows about slender inclined bodies of revolution at high angles of attack (ref. 1). In this experiment, a small amount of water was injected downstream of the nozzle, and vaporization was nearly instantaneous. The temperature drop from the expansion in the supersonic nozzle caused the water vapor to condense into a fine fog. A light sheet (or screen) produced by a high-pressure mercury-vapor lamp was projected through a glass window in the side of the test section in a plane perpendicular to the axis of the tunnel. This light sheet was used to illuminate the fog as it was entrained in the flow field over the model. A representative installation of the vapor screen flow visualization is sketched in figure 1. The distribution of condensed water vapor and, consequently, the amount of scattered light within the plane of the light sheet were affected by the flow disturbances created by the model at a high angle of attack. This phenomenon permitted the observation and the documentation of body vortex cross sections, which appeared as black dots within a light background in the vapor screen image; these dots were caused by the absence of scattered light.

Similar experimental techniques and apparatus were used in reference 2 to visualize vortices, vortex sheets, lines of flow separation and reattachment, and shock waves at higher subsonic, transonic, and supersonic speeds. These tests were conducted, beginning in the late 1950's, in the 3-Foot Supersonic Wind Tunnel of the Royal Aeronautical Establishment (RAE). The studies suggested that the lowest free-stream Mach number at which the vapor screen technique was practicable was approximately 0.85. At lower Mach numbers, continuous injection of water was required to maintain a satisfactory visualization level, and dense white patches caused by local condensation about the model obscured the images when viewed from a downstream location.

Flow visualization using the vapor screen method was extended to lower subsonic Mach numbers ($M_\infty = 0.60$) in experimental investigations of symmetric forebodies initiated in the 1970's in the 6- by 6-Foot Supersonic Wind Tunnel (ref. 3) at the Ames Research Center. At subsonic Mach numbers, the body vortices appeared as white spots surrounded by a dark background; these white spots resulted from the water vapor condensing first near the vortex cores. Improved water injection control and more uniform free-stream temperature distribution compared with the experiments in reference 2 enabled the observation and the documentation of the vortices at Mach numbers of less than 0.85.

Lasers superseded the mercury-vapor lamps as the primary light-sheet source beginning in the late 1970's. Lasers provided a thinner, more intense sheet of light which enhanced the details of the vapor screen images. The flow visualization method was accordingly referred to as LVS. The LVS method is designed for use at high subsonic through supersonic speeds, and it is distinguished from low-speed laser light-sheet techniques that use different seeding particles to visualize the cross-flow patterns. References 4 through 6 are representative of the high-quality results obtained in low-speed wind tunnels ($M_\infty < 0.3$) using smoke or propylene glycol as the light-scattering medium.

The use of the LVS method as a standard tool to visualize the vortex-dominated flow fields about subscale models of fighter aircraft configurations at subsonic through supersonic speeds evolved from several experimental investigations conducted by NASA in cooperation with the United States Air Force and Navy beginning in the mid-1980's. The initial testing was conducted in the 6- by 6-Foot Supersonic Wind Tunnel at the Ames Research Center and the 7- by 10-Foot Transonic Tunnel (7- by 10-Foot TT) at the David Taylor Research Center (DTRC) using subscale models of generalized and specific fighter configurations. Representative results from these studies (refs. 7 through 9) are presented in figures 2 through 4. The LVS method was used successfully to establish a flow visualization data base on multiple-vortex development, vortex-tail and vortex-shock interactions, vortex breakdown, and vortex control concepts at free-stream Mach numbers from 0.30 to 1.80. Continuous injection of water was required at low Mach numbers to promote the desired condensation patterns, while intermittent injection of water in smaller amounts was sufficient at high Mach numbers. Consistent with earlier studies (refs. 1 through 3), researchers found that the vortices appeared as white regions surrounded by a dark background at the subsonic speeds and as dark regions in a white background at supersonic speeds. At transonic speeds, a combination of the two light-scattering patterns typically occurred.

The testing in NASA and Navy facilities revealed deficiencies in the LVS experimental setup employed in larger scale wind tunnels. A mirror-based system was used to direct, or steer, the laser beam to the light-sheet-generating optics located on the sidewall or the ceiling of the wind tunnel test section. The laser was located outside the pressure, or plenum, shell surrounding the test section of the DTRC facility because of laser operational considerations. As a result, the laser beam was directed over a large distance, and several mirrors were required to steer the beam to the light-sheet optics. Tunnel vibration at high speeds promoted a misalignment of the laser beam and optical components, while airborne contaminants (oil, for example) settling onto the mirror surfaces reduced the quality and the intensity of the light sheet at the model. These effects sometimes caused significant reductions in tunnel efficiency and productivity because access to the optics inside the plenum region was generally required to realign or clean the system. In most cases, 2 to 3 hours were required to vent the plenum region to atmospheric pressure, realign or clean the optics, and repressurize the plenum to the desired operating conditions. In addition, the exposed laser beam and the use of multiple mirrors posed a safety hazard, particularly during the alignment process, because the laser had to be aligned at high power.

Fiber optics (ref. 10) provided a solution to the inherent problems of mirror-based beam delivery systems. A fiber optic cable extending from the laser head to the light-sheet optics provided an effective beam delivery and containment system with enough power in the beam to produce a light sheet. A prototype system consisting of a 150-ft-long fiber optic cable and a continuous-wave (CW) argon-ion laser was installed and successfully applied by NASA in 1989 for use in a test of a 0.06-scale F/A-18 model with forebody yaw control strakes in the 7- by 10-Foot TT (ref. 11) at the DTRC. A nonpulsed laser is well suited for visualizing low-dynamic vortical flows, such as those generated by the F/A-18 configuration in steady-flow conditions. A pulsed laser is required to visualize high-dynamic flows as would be encountered, for example, about a helicopter rotor blade. Results from using this prototype system are shown in figure 5. The flow visualization results were obtained at $M_\infty = 0.80$ using a video camera that was mounted aft of the model on the sting support system and looking upstream along the model centerline. Figure 5(a) shows the interaction of the wing leading-edge extension (LEX) vortices with the twin vertical tails. The complex vortical flow features along the forward fuselage section with the left forebody yaw control strake installed are illustrated in figure 5(b). Permanent fiber-optic-based LVS flow visualization systems were developed after the DTRC testing and the systems were installed in 1990 in the Langley 8-Foot Transonic Pressure Tunnel (8-Foot TPT) and the Langley 7- by 10-Foot High-Speed Tunnel (7- by 10-Foot HST). Similar systems are now standard tools for aerodynamic research in several Langley Research Center (LaRC) wind tunnels. The present paper will describe the experimental

apparatus and its operation and show representative results from the 8-Foot TPT and 7- by 10-Foot HST facilities.

Symbols and Abbreviations

b	wing span, in.
C_D	drag coefficient, $\frac{\text{Drag}}{q_\infty S_{\text{ref}}}$
C_L	lift coefficient, $\frac{\text{Lift}}{q_\infty S_{\text{ref}}}$
C_l	body-axis rolling-moment coefficient, $\frac{\text{Rolling moment}}{q_\infty S_{\text{ref}} b}$
C_{l_β}	lateral stability derivative, $\frac{\partial C_l}{\partial \beta}$, calculated by $\frac{C_{l_{(\beta=+5^\circ)}} - C_{l_{(\beta=-5^\circ)}}}{10^\circ}$, per deg
C_m	pitching-moment coefficient referenced to $0.40\bar{c}$, $\frac{\text{Pitching moment}}{q_\infty S_{\text{ref}} \bar{c}}$
C_n	body-axis yawing-moment coefficient, $\frac{\text{Yawing moment}}{q_\infty S_{\text{ref}} b}$
C_{n_β}	directional stability derivative, $\frac{\partial C_n}{\partial \beta}$, calculated by $\frac{C_{n_{(\beta=+5^\circ)}} - C_{n_{(\beta=-5^\circ)}}}{10^\circ}$, per deg
$C_{p,u}$	wing upper-surface static pressure coefficient, $\frac{p - p_\infty}{q_\infty}$
C_Y	side-force coefficient, $\frac{\text{Side force}}{q_\infty S_{\text{ref}}}$
C_{Y_β}	side force caused by sideslip derivative, $\frac{\partial C_Y}{\partial \beta}$, calculated by $\frac{C_{Y_{(\beta=+5^\circ)}} - C_{Y_{(\beta=-5^\circ)}}}{10^\circ}$, per deg
c	wing centerline chord, in.
$\bar{c}$	wing mean aerodynamic chord, in.
M_∞	free-stream Mach number
p	local upper-surface static pressure, lb/in^2
p_∞	free-stream static pressure, lb/in^2
q_∞	free-stream dynamic pressure, lb/in^2
S_{ref}	reference wing area, in^2
s	wing local semispan distance from fuselage centerline to wing leading edge, in.
$\mathbf{V}_\infty$	free-stream velocity, ft/sec
x	distance along wing centerline chord measured from wing apex, in.
y	distance along wing local semispan measured from fuselage centerline, in.
α	angle of attack, deg
β	angle of sideslip, deg
δ_v	vertical tail cant angle, deg

Abbreviations:

CFD	computational fluid dynamics
CW	continuous wave
DTRC	David Taylor Research Center
HSCT	high-speed civil transport
HST	High-Speed Tunnel
LaRC	Langley Research Center
LEX	wing leading-edge extension
LVS	laser vapor screen
NACA	National Advisory Committee for Aeronautics
NASA	National Aeronautics and Space Administration
NIRC	Nonionizing Radiation Committee
OCS	outboard control surface
RAE	Royal Aeronautical Establishment
SMA	small/miniature/type A connector
TE	trailing edge
TPT	Transonic Pressure Tunnel
TT	Transonic Tunnel

Wind Tunnel Facilities

The two LaRC facilities discussed are the Langley 8-Foot Transonic Pressure Tunnel (8-Foot TPT) and the Langley 7- by 10-Foot High-Speed Tunnel (7- by 10-Foot HST). The 8-Foot TPT is a continuous-flow, closed-return, slotted-throat pressure tunnel (fig. 6) that is capable of operating at pressures between 0.25 and 2.0 atm over a Mach number range from 0.2 to 1.2. The 7- by 10-Foot HST is a continuous-flow, solid-wall, subsonic-transonic atmospheric wind tunnel (fig. 7). The Mach number range is from $M_\infty \approx 0.06$ to $M_\infty \approx 0.94$. The tunnel operates at ambient temperature and pressure and continuously exchanges air with the surrounding atmosphere. Detailed descriptions of the 8-Foot

TPT and the 7- by 10-Foot HST are provided in references 12 and 13, respectively.

These facilities are used primarily to conduct fundamental research related to the exploration of new aerodynamic concepts. The studies include concepts to improve the understanding and the control of flow phenomena associated with civil and military aircraft configurations and experiments to assist in the development and the validation of computational fluid dynamics (CFD) methods. These facilities are also used in cooperative programs with the United States Department of Defense and industry to develop and validate new aircraft designs as well as modifications to existing aircraft.

Laser Safety at LaRC

The LaRC safety policy is to (1) exercise centralized control over operations involving the use of hazardous radiation-producing equipment; (2) assure that exposure of personnel to nonionizing radiation from such equipment is kept to a safe level; and (3) assure that compliance with applicable Federal, state, and local regulations is maintained. Reference 14 describes the organization, the training, and the responsibilities for radiological health and safety activity at LaRC. This document also defines procedures and requirements for procurement, use, and handling of sources of nonionizing radiation. The procedures and the practices are intended primarily for the use of lasers and laser sources, although they are applicable to other hazardous noncoherent sources of nonionizing radiation, such as radar, solar simulators, and high-intensity arc lamps.

Personnel at LaRC established a Nonionizing Radiation Committee (NIRC) to review and approve all procurement, handling, and use of lasers and laser sources. The NIRC is also required to audit and inspect the possession and the use of lasers of each facility on an annual basis.

The responsibility for implementing the LaRC policies is divided among five safety and health functions. These functions include the organizational facility safety head for each facility, the radiation safety officer, the safety manager for LaRC, the occupational health officer, and the radiation workers. Procurement of any hazardous source of nonionizing radiation must be approved by the organizational facility safety head, the radiation safety officer, and the safety manager. In addition, safety permits are required for all class 4 lasers and for class 3b lasers where a significant possibility exists that its users and operators will be exposed to radiation levels in excess of the applicable maximum permissible exposure (ref. 14). Class 4 lasers are high-power systems that not only produce a hazardous direct or specularly reflected beam but also a hazardous diffuse reflection and a significant skin hazard. Continuous-wave class 4 lasers are categorized as those that have wavelengths of 200 to 400 nm (the ultraviolet range), 1400 nm to 1 mm and 400 nm to 700 nm (the visible range), and 700 nm to 1400 nm (the near-infrared range) and that emit an average accessible radiant power of 0.5 W or greater for periods greater than 0.25 sec. Class 3b consists of lasers that can produce accidental injury if viewed directly. Intrabeam viewing of either a direct or a mirror-like (specular) reflection of the beam is also considered hazardous. For CW class 3b lasers, the average radiant power does not exceed 0.5 W for exposure time greater than 0.25 sec. The safety permit request is submitted by the organizational facility safety head, and the request is reviewed and approved by the radiation safety officer, the NIRC, and the safety manager. Personnel appointed to each facility laser system and identified in the safety permit must be educated, trained, and certified as radiation workers. Personnel must also be given an initial complete eye examination and subsequent annual laser eye examinations. Medical records are specifically identified for certified nonionizing radiation workers.

The high-power class 4 lasers require the most rigid control measures because of the greater likelihood of injury caused by specular and diffuse reflections. The entire beam path that is capable of producing hazardous diffuse reflections must be controlled. These controls rely primarily on positive methods, such as enclosures and interlocks, and secondarily on procedural safeguards. Class 4 lasers require isolation in an area designated for laser operations, and access to such an area requires appropriate authorization.

The electrical installation and connection to the power supply circuit must meet the American National Standards Institute National Electrical Codes (ref. 14). Class 3b and class 4 lasers and laser systems must also have appropriate warning labels and laser control area posting.

The fiber-optic-based LVS systems discussed in this report represent a significant improvement in laser system safety because the beam is always contained within the fiber cable or within the optically sealed plenum shell surrounding the wind tunnel test section. The simplicity and the reliability of the LVS systems also facilitate the education and the training of personnel. Details of the fiber optic LVS systems are provided in the next section.

Technical Discussion

Fiber-Optic-Based LVS Systems

The discussion of the fiber-optic-based LVS systems will focus on the 8-Foot TPT installation. The system components and setup in the 8-Foot TPT closely resemble those in the 7- by 10-Foot HST. Figure 8 presents a schematic of the 8-Foot TPT, and figure 9 shows a sketch of the major fiber-optic-based LVS system components. The major components include laser light source, fiber optic beam delivery system, light-sheet optics, water injection system to increase the wind tunnel humidity, and video equipment for observation and documentation of the LVS images.

A 36-ft-diameter plenum shell encloses the test section of the 8-Foot TPT. Because of laser operational considerations, the laser head is located outside the plenum region in an optically sealed room abutting the plenum shell (fig. 9). The layout of the laser room is sketched in figure 10. The laser system components, which are shown in the photographs in figure 11, include a 6-W argon-ion laser, a power supply, a remote control module, a heat exchanger for laser cooling, and a city water supply for heat exchanger cooling. (Note that fig. 11(e) is from the 7- by 10-Foot HST and that it more clearly shows the city water supply system.) A higher power laser was selected for use in the 8-Foot TPT and the 7- by 10-Foot HST on the basis of previous LVS wind tunnel testing by NASA (refs. 7 through 9 and 11). The level of water vapor condensate about any model depends on the wind tunnel test conditions and the associated flow field generated by the model. A strong leading-edge vortex shed from the wing of a fighter aircraft model, for example, induces large changes in local pressure, temperature, and relative humidity (ref. 15). Lower laser output power is required to illuminate features of the flow under these conditions. A transport model flow field may be characterized by less dramatic changes in the local flow conditions; therefore, this situation requires higher laser power to extract useful flow visualization information. NASA testing conducted in the 6- by 6-Foot Supersonic Wind Tunnel at the Ames Research Center (ref. 8) and the 7- by 10-Foot TT at the DTRC (refs. 7, 9, and 11) on generic and specific fighter aircraft models showed that laser output power from approximately 0.5 W to 5 W was required to provide adequate flow visualization at subsonic through supersonic speeds. Note that the specific application determines the selection of the laser. The laser optics are configured for all-spectral-lines, multimode operation to maximize output power. The laser head is positioned on an optical table mounted to four pneumatic vibration-isolation legs. This setup minimizes the effect of tunnel vibration on the laser optical alignment. The remote module features a 50-ft electronics cable extension to allow the control of the laser from a location such as the wind tunnel control room. The laser cooling water system consists of the heat exchanger with an internal 5-gal reservoir of deionized and deoxygenated water. The heat exchanger provides cooling water in a closed loop to the laser head. Cooling of the 5-gal reservoir is accomplished by routing city water to the heat exchanger. The city water is pumped into a 50-gal reservoir. The discharge flow from the 50-gal reservoir to the heat exchanger is augmented by a 1-hp pump. The city water supply is an open-loop system, and it is drained after thermal contact with the heat exchanger. The laser system features several safety interlocks among the city water supply, the heat exchanger, the laser room entry door, and the laser power supply to safeguard personnel and equipment. In addition, a voltage monitor unit continuously monitors the facility three-phase voltage supply to the laser room. An audible alarm system in the wind tunnel control room alerts the laser operator if the facility voltage supply is outside a specified range, as would occur in a power "brown-out" or over-voltage situation. The laser beam is contained in an armored fiber optic cable (fig. 11(a)) which penetrates the optically sealed plenum shell. As a result, the operating environment in the laser room is free of exposed laser radiation.

The photographs in figure 12 show the penetration of the fiber optic cable into the plenum region through an aluminum porthole blank installed in the plenum shell (fig. 12(a)). The armored fiber optic cable is contained in copper tubing for strain relief. The copper tubing is supported by a U-channel (fig. 12(a)) extending from the inside surface of the plenum shell to the top of the wind tunnel test section. The fiber optic cable and copper tubing assembly is then routed to a box beam in the test section ceiling (fig. 12(b)) which contains the light-sheet-generating optics. Note that the control room observation windows shown in figure 12(a) are optically sealed by metal shutters during laser operation.

The fiber-optic-based beam delivery system contains five principal components: laser-to-fiber coupler, armored fiber optic cable, remote line projector, scanning mirror, and motor controller. The components are shown in the photographs in figure 13, and they are sketched in figure 14. The system is designed to be used with virtually any argon-ion laser operating in either CW or multimode with beam diameters of 0.0315 in. to 0.0709 in. The beam is directed into

the fiber core via the laser-to-fiber coupler (fig. 15). This coupler has four knobs that provide vertical, horizontal, and angular adjustments of the beam relative to the fiber core. The range of vertical and horizontal adjustments is ±0.05 in., and the angular adjustment range is ±3°. A small/miniature/type A (SMA) connector is used to anchor the fiber optic cable to the laser-to-fiber coupler as well as to house a focusing lens.

As indicated in reference 16, optical fibers are circular dielectric waveguides that can transport optical energy and information. In the present application, the objective is to transport optical energy as efficiently as possible. The optical fibers have a central core surrounded by a concentric cladding. The refractive index of the core is approximately 1 percent higher than the refractive index of the outer cladding. As a result, light will be confined to the core if the angular condition for total internal reflectance is satisfied (ref. 10). The cladding and the core are encased in a jacket and an armored sheath for protection. A multimode step-index fiber with fused silica core is used in the LaRC systems. The numerical aperture of the fiber is 0.22. Multimode step-index fibers have a 50- to 1000-μm-diameter core with a constant refractive index. The LaRC optical fibers have a 200-μm core diameter. This class of optical fibers is inexpensive, and their large core diameter is desirable for ease of use and good light collection efficiency. These fibers also provide a high-quality light sheet by forming a homogeneous beam at the output end of the fiber. The numerical aperture of the fiber refers to the sine of the half angle of the cone of light which enters or exits the fiber ends multiplied by the refractive index of the medium in which the cone is located. In the present case, the refractive index is 1. The numerical aperture can also be viewed as the largest angle that an incident ray can have for total internal reflectance in the core (ref. 16). A higher numerical aperture fiber features better light-gathering ability and facilitates coupling of light into the fiber. The cable length is 60 ft in the 8-Foot TPT. A 30-ft long cable is used in the 7- by 10-Foot HST because of the smaller plenum diameter and reduced distance from the laser head to the light-sheet optics. The fiber cable length is specific to the test facility and is determined by the proximity of the laser head to the test section and the required cable routing.

Alignment of the laser beam with respect to the fiber core is accomplished by connecting the output end of the fiber optic cable to a detector head and laser power meter assembly (fig. 16). The laser output power during the preliminary alignment is limited to 0.5 W or less. Operation at higher out-put power levels with an initially misaligned beam can scorch the outer sheathing and cause permanent damage to the fiber core. Beam alignment is obtained by adjusting the four translation and rotation knobs on the laser-to-fiber coupler in sequence until the output reading on the power meter is maximized. A throughput (the ratio of power out to power in) of 75 percent to 80 percent is typical and depends on the fiber optic cable length and the condition of the fiber. Figure 17(a) illustrates the transmission loss, or attenuation, in decibels versus the fiber optic cable length using the manufacturer's specification of 0.0073 dB/ft attenuation through a 0.22 numerical aperture fiber. The laser throughput can be estimated using the following relationship from reference 10:

$$\text{Attenuation} = -10\log_{10}\left(\frac{\text{Power out}}{\text{Power in}}\right) \qquad (1)$$

$$\frac{\text{Power out}}{\text{Power in}} = 10^{-[0.1(\text{Attenuation})]} \qquad (2)$$

Figure 17(b) shows the effect of fiber optic cable length on the throughput. Additional sources of transmission loss are from the two ends of the fiber and from the front and back surfaces of the focusing lens in the fiber coupler. Laboratory testing at Aerometrics, Inc., Sunnyvale, California, indicates that a loss of approximately 4 percent is incurred through each end of the fiber. The transmission loss through the focusing lens can be reduced to approximately 2 percent per side by applying a suitable antireflective coating. These additional losses are accounted for in the second curve in figure 17(b). The actual throughputs achieved in the initial testing in the 7- by 10-Foot HST and the 8-Foot TPT at LaRC using 30-ft and 60-ft cables, respectively, and in the 7- by 10-Foot TT at the DTRC using a 150-ft cable (ref. 11) are also shown in figure 17(b). The actual throughputs for the 30-ft and 60-ft cables are very close to the estimates. The lower throughput of the 150-ft cable is probably the result of manufacturing flaws in the fiber end connections. The 150-ft cable was a "first-generation" cable fabricated for the DRTC testing prior to the development of the LaRC systems. Periodic checks of the throughputs of the 30-ft and 60-ft cables since 1990 have shown a decrease of approximately 1 percent per year. This decrease may be caused by microbending in the fiber core arising from frequent handling of the cable ends. Some deterioration of the fiber end faces may also be caused by a periodic cleaning process using lapping film and methanol.

Experience has shown that the laser-to-fiber coupler alignment is maintained indefinitely and is insensitive to large vibrations caused by wind tunnel operation at high subsonic and transonic speeds. This characteristic significantly improves the productivity of LVS flow visualization testing.

Test results at Aerometrics, Inc., show that the fiber optic cable can accept a beam with a maximum output power of 20 W. The maximum output power of the lasers used in the 8-Foot TPT and the 7- by 10-Foot HST is typically 10 W. Laser-to-fiber coupler alignment has been conducted to the maximum power without incident.

The output end of the fiber optic cable is anchored to the remote line projector unit using an SMA connector. The line projector is a compact, self-contained unit that generates the light sheet and provides control of the sheet divergence (spread angle) and sheet focus (thickness). The unit is portable, and it can be positioned wherever there is optical access to the test section. A ceiling location was selected in both wind tunnels to provide maximum illumination of the model upper-surface flow field. The line projector unit is installed in a window that is 4 in. wide and 16 in. long in the 8-Foot TPT and in a window that is 9.38 in. wide and 47.38 in. long in the 7- by 10-Foot HST. The unit can be positioned in any of three identical windows along the centerline of the 8-Foot TPT ceiling, depending on the model length and location in the test section. The unit can be positioned anywhere in the longer window of the 7- by 10-Foot HST or in a second window that has the same dimensions farther forward in the test section. The line projector optics consist of a three-lens system (fig. 18) featuring an achromatic doublet lens and two identical plano-cylindrical lenses. The output of the fiber optics in the present systems is an extended luminous source as opposed to a point source of light. Because of this characteristic, the diverging output of the fiber cannot be truly focused but only imaged to a waist. The imaging is accomplished using a special two-element lens, or an achromatic doublet. The 3.15-in. focal length achromatic lens also corrects for coma and cancels chromatic aberration (ref. 16). Translation of the achromatic lens relative to the plano-cylindrical lenses controls the laser light-sheet thickness, or focus (fig. 19(a)). The minimum thickness at the model surface is approximately 0.06 in. Refocusing is required at all model stations and model pitch attitudes. In practice, however, the minimum light-sheet thickness is obtained at a selected combination of model station and pitch angle, and refocusing of the light sheet is performed as needed during the testing. A thin light sheet is preferred because it provides better clarity of the flow features. This clarity is particularly important when viewing cross-flow details where the flow structure changes rapidly in a streamwise direction along the wing. For this reason, cross-flow images obtained using a thick light sheet may appear smeared. NASA testing suggests that fiber optics reduce the thickness of the light sheet at the model compared with a mirror-based beam delivery system in which the laser beam is unassisted or freely expanding. The plano-cylindrical lenses produce magnification or focus in one direction only (fig. 19(b)). The light-sheet divergence, or spread, is controlled through the use of two cylindrical lenses in tandem. By translating the first cylindrical lens relative to the second, fixed lens (fig. 19), the sheet half angle can be varied from 4° to 55°. To reduce back reflections, an anti-reflection coating is applied to the two exposed surfaces of each lens. The line projector optics are enclosed within a cylindrical cover to protect the lens surfaces and the end face of the fiber optic cable from airborne contaminants. Contaminants settling onto the end of the fiber optics can cause local scorching and may ultimately lead to the destruction of the fiber core.

Fore and aft scanning of the light sheet is produced by a 3- by 3-in. plane mirror positioned near the output end of the line projector (figs. 13(c) and 14). The mirror is mounted onto a rotational stage with 360° of continuous rotation. The mirror directs the light sheet through a glass window located along the centerline of the test section ceiling and to the desired station on the model. The light-sheet optics are located in the ceiling window at the beginning of a test such that the light sheet is perpendicular to the model surface at a selected model station and pitch angle. Because the light sheet sweeps in an arc along the model, it is generally nonorthogonal with respect to the model surface at all other conditions.

The motor controller (figs. 13(d) and 14) provides the light-sheet focus (thickness), divergence (spread), and sweep control from a remote station, which is usually the wind tunnel control room. The focus control is varied until the thickness of the light sheet projected onto the model surface is minimum. The light-sheet divergence is also "tailored" to the model, and it typically spans from wing tip to wing tip. The light-sheet characteristics are observed on a video monitor because the test area is optically sealed. The light sheet can be scanned continuously from the model nose to a position downstream of the model base, or it can be fixed at any desired model station. Model stations are typically identified using white correction fluid applied in thin, narrow

strips perpendicular to the model centerline. These identifier marks flash prominently during testing as the laser light sheet passes each station.

Vapor screen flow visualization is made possible by injecting water into the diffuser section of the wind tunnel circuit. A 150-gal tank of deionized water is located in a room atop the plenum shell of the 8-Foot TPT (fig. 9). A solenoid switch and a 1-hp pump positioned on the discharge side of the water tank are activated from the wind tunnel control room. The switch and the pump route the water through a high-pressure hose that penetrates the plenum shell. The water is directed to a manifold and then to an array of six atomizer spray nozzles installed in the ceiling of the wind tunnel diffuser (fig. 9). The nozzles emit full-cone spray patterns that encompass most of the diffuser cross section under static (wind-off) conditions. The diffuser section was selected because of the relatively high cross flow relative to the injected spray patterns that would assist in the atomization of the water particles. A video camera was installed during the initial LVS testing in the 8-Foot TPT to view the interaction of the diffuser flow and the water spray patterns. The camera was located in the floor of the tunnel just downstream of the arc sector (fig. 9) and viewed through a window along the floor centerline. The results were inconclusive, however, regarding the coverage and plumes of the spray patterns or whether the injected water particles vaporized in the diffuser. Incomplete vaporization is a concern because of possible water impact and erosion damage to the fiberglass fan blades in the 8-Foot TPT and the wooden fan blades in the 7- by 10-Foot HST. As a safeguard, the leading edges of the blades have been treated with a special erosion coating. The 8-Foot TPT dryer system is used immediately after the flow visualization to safeguard the facility electronic equipment and to reduce the risk of corrosion to the tunnel structure. A two-unit dryer system using silica gel as the dessicant is employed (ref. 12). Each unit has the capacity of 2500 ft^3/min at pressures up to 4 atm. The air output from the dryer has a dew point not exceeding $-70°\text{F}$. For initial drying of the tunnel and rapid drying of the test section and surrounding tank, a 10 000 ft^3/min compressor of compression ratio 4 is provided. Qualitative guidelines that help to establish the amount of water injection necessary for suitable flow visualization are shown by the onset of a visible plane of light in the test section or a local condensation within the vortex flows about the model. The LVS flow visualization is typically conducted in the 8-Foot TPT at free-stream Mach numbers from 0.60 to 1.20. Up to 25 gal of water may be required at $M_\infty = 0.60$ to achieve ade-

quate flow visualization for a range of angle of attack. This quantity diminishes to approximately 5 gal at $M_\infty = 1.20$. The approximate volume of the 8-Foot TPT circuit is 370 000 ft^3. Note that the required water injection will also depend on the flow field generated by the model. Relative humidity levels are determined in the 7- by 10-Foot HST from hygrometer measurements made in the settling chamber of the tunnel. The capability to conduct similar measurements in the 8-Foot TPT is a planned upgrade. These measurements provide an indication of (1) the possible need to inject water and (2) the efficiency of the water injection system to increase the humidity. In many applications where a model generates strong vortical flows, relative humidity levels measured in the settling chamber of the 7- by 10-Foot HST as low as 30 percent are sufficient to yield satisfactory flow visualization. The vortices can induce significant increases in the local relative humidity (ref. 15), and can thereby cause local condensation even at very low free-stream relative humidity levels. Water injection is frequently unnecessary in the 7- by 10-Foot HST. This facility exchanges up to 10 percent of the tunnel airflow by volume with the outside air. Exchange with humid outside air is often sufficient to increase the relative humidity in the test section to acceptable levels for flow visualization. As a result, LVS flow visualization has frequently been obtained on vortex-dominated models at M_∞ as low as 0.20 and up to $M_\infty = 0.85$ without water injection. The LVS flow visualization has been performed concurrently with the measurements of the model surface static pressures and forces and moments. However, this procedure has been employed only at subsonic speeds for models that develop strong vortex flows at high angles of attack. Experience has shown that model surface static pressures and force and moment data are unaffected by varying humidity levels where the flow field is dominated by vortices. Test data in reference 9 show that increased relative humidity has no observable effect on forebody and wing LEX surface static pressures and total forces and moments on an F/A-18 configuration at $M_\infty = 0.60$ and high angles of attack. In this case, water was injected into the settling chamber of the tunnel in a sufficient quantity to cause local condensation within the strong LEX vortices. The weaker forebody vortices were not visible. This procedure is not recommended on models that are dominated by attached flow or that develop shock waves at transonic and supersonic speeds because of the adverse effect of a "moist" tunnel on the boundary layer and shock behavior.

Observation and documentation of the laser light-sheet characteristics during the alignment process

and of the model flow field revealed by the laser light sheet during tunnel operation are accomplished exclusively with color video-based systems. A miniature video camera that has 360 television lines of horizontal resolution and a fixed focal length lens (fig. 20) is contained in a cylindrical housing that is mounted onto the model sting support system (fig. 9). This camera provides a perspective aft of the model which looks upstream along the model centerline. The video image perspective remains constant throughout the pitch angle range because there is no relative motion between the camera and the model. The video image perspective does change, however, throughout yaw angle and roll angle ranges. A second video camera (fig. 21) with 560 television lines of horizontal resolution and a variable focal-length lens is located outside the test section in approximately a right three-quarter rear position (fig. 9). The lens focal length, the focus, and the iris are remotely controlled. The camera head is mounted to a tilt/pan table that features remotely controlled angular displacement about two axes. Each camera is connected to a color video monitor and videocassette recorder. Title generators interface with the wind tunnel data acquisition system and provide real-time test conditions superimposed on the video images. Hard copies of any selected recorded video frame or real-time image are obtained using a color video printer unit. This unit allows the acquisition of only single frames. Digital cameras combined with imaging enhancement tools offer a significant improvement to the resolution obtained with the present video camera system. Still photography is available in the 8-Foot TPT and the 7- by 10-Foot HST. However, this capability has not been employed during LVS operation. The size of a still camera and its protective housing is prohibitive for installation on the model support system because of the flow disturbances that may propagate upstream to the model. A still camera mounted outside the test section is inaccessible for adjustments during tunnel operation to account for varying light levels or the movement of the model through the test section caused by varying pitch, roll, and yaw angles.

The fiber optics, the optically sealed plenum shell, and the video-based equipment provide an LVS system that isolates the user from the laser beam and from the laser light sheet during all phases of its operation. Application has shown that approximately 5 min are required to bring the LVS system on-line for observation and documentation of the flow field. The training required to operate the LVS systems is minimal. Furthermore, a single user can operate the entire LVS system. The laser remote module, the line projector and scanning mirror motor controller, the

camera controls, the video monitors and recorders, and the title generators are consolidated at a work station in the wind tunnel control room.

Representative LVS Results

The 7- by 10-Foot HST fiber-optic-based LVS system became operational in January 1990, whereas the 8-Foot TPT system was used for the first time in March 1990. Figure 22 presents planform sketches of several models that have been tested since 1990 in LaRC wind tunnels in conjunction with the LVS flow visualization technique. Representative LVS results obtained on these models are presented in figures 23 through 29. The test conditions correspond to free-stream Mach numbers from 0.40 to 1.20, tunnel total pressures ranging from approximately 0.25 atm to 1.0 atm, tunnel total temperatures from approximately 60°F to 100°F, and angles of attack between 9° and 22°. Whenever possible, LVS flow visualization is conducted at tunnel total temperatures of 100°F or less. The flow visualization quality diminishes at higher operating temperatures. Hot tunnel air can contain more water vapor before condensation occurs. As a result, greater quantities of water are required to promote condensation. Under these conditions, condensation can occur in the free stream as well as locally within the vortical flows. This condensation pattern provides a poor contrast and correspondingly decreases the flow details. The models are typically painted with a flat black paint to reduce glare and to increase the contrast between the illuminated cross-flow patterns and the model surface.

The first LVS results in the 7- by 10-Foot HST were obtained using a generalized fighter model featuring chine-like forebody strakes and a 55° cropped delta wing (figs. 22(a) and 23). The LVS photographs in figure 23 correspond to $M_\infty = 0.40$, $\alpha = 20°$, and two selected stations along the wing. The perspective is from a right, three-quarter rear position. Tunnel airflow exchange with humid outside air increased the relative humidity in the test section so that local condensation occurred in the vortex flows. Water was not injected through the atomizer nozzles in the diffuser section during this test. The strake and wing vortices are visible as regions of high scattered light with approximately circular cross section surrounding hollow cores. The interaction of the strake and wing vortices and the breakdown of the wing vortical flow are illustrated in figure 23(c). Onset of vortex breakdown is apparent in the real-time LVS images by the appearance of condensed water vapor in the core of the vortex and an expansion and unsteadiness of the vortex cross section. A laser output power of 1 W was sufficient to produce the

results shown in figure 23. This laser output power produces approximately 0.80 W at the output end of the fiber optic cable. The same model was tested in the 7- by 10-Foot TT (ref. 7) at the DTRC at $M_\infty = 0.40$ using a mirror-based beam delivery system. These preliminary results suggested that the fiber-optic-based LVS system provides a thinner and more uniform light sheet, yields flow features at lower laser output power, and is safer and more reliable compared with a mirror-based system.

The LVS results obtained in the 7- by 10-Foot HST at $M_\infty = 0.50$ and $\alpha = 25°$ on a 65° cropped delta wing model (fig. 22(b)) with LEX and twin canted tails are shown in figure 24. An objective of this test was to determine the effect of vertical tail cant angle δ_v on the vortex flow behavior and the overall aerodynamic and stability characteristics. The cant angle is measured relative to the wing surface normal and is positive outward. The photographs depict the cross sections of wing and LEX vortices observed from a three-quarter right rear position (figs. 24(a) through 24(d)) and from a position aft of the model which looks upstream along the model centerline (figs. 24(e) through 24(h)). The mutual interaction of wing and LEX vortices and the vortex interaction with the twin tails canted to 30° are shown in figures 24(a) through 24(f). The vortex-vortex and vortex-tail interactions in sideslip are revealed in figures 24(g) and 24(h). Note that a combination of model pitch and roll angles is used in this test to provide the desired angles of attack and sideslip. A typical application of LVS flow visualization is to assist in the interpretation of the model surface static-pressure distributions and six-component forces and moments in figures 24(i) through 24(k). The effect of δ_v on the right wing upper-surface pressure distributions at $M_\infty = 0.50$ and $\alpha = 25°$ is shown in figure 24(i). The spanwise pressure distributions display a single suction peak at all three model stations despite the presence of two primary vortices (i.e., data corresponding to $\delta_v = 30°$ which are shown by the square symbols). The LVS flow visualization near $x/c = 0.30$ (fig. 24(a)) indicates that the suction peak near the leading edge is caused by the wing vortex, while the LEX vortex is too high above the surface to induce a direct suction peak. The LVS result near the tail (fig. 24(c)) indicates that LEX and wing vortices are coiled about each other with the wing vortex situated directly above the LEX vortex. This flow situation is consistent with the single suction peak in the spanwise pressure distributions at $x/c = 0.80$. The tails canted to 30° are situated in the path of the interacting vortices (fig. 24(e)). This cant angle causes

an upward displacement of the vortices from the wing surface, which can be inferred from the LVS photographs at two stations along the tails in figures 24(c) through 24(f). Test results (not shown) also indicate that the tails canted outward 30° cause an early breakdown of the vortical flows. The vortex displacement diminishes the vortex-induced pressure signatures at $x/c = 0.60$ and 0.80 (fig. 24(i)) compared with the results obtained at the other cant angles. The diminished vortex-induced suction pressures and early vortex breakdown cause a reduction in lift, increased drag, and increased nose-up pitching moment as shown in figure 24(j). In sideslip, the tails canted to 30° promote vortex breakdown asymmetry. This asymmetry is shown in figures 24(g) and 24(h) at $\beta = 5°$. The photograph in figure 24(h) shows that vortex breakdown occurs at the windward tail (i.e., the right side in the photograph), while the vortices are stable and pass outboard of the tail on the leeward (left) side. This vortex-tail interaction causes an unstable break in the static lateral stability derivative C_{l_β} (fig. 24(k)) at an earlier angle of attack compared with the model that has other tail cant angles. The photograph in figure 24(h) suggests that the leeward tail is embedded in a favorable vortex flow field. The vortex-induced suction pressures on the outside surface of the leeward tail promote a negative increment to C_{Y_β} (i.e., negative side force acting to the left; fig. 24(k)) and a corresponding stable increment to the directional stability derivative C_{n_β}.

The LEX vortex flows about a 0.06-scale model of the U.S. Navy/McDonnell Douglas Corporation/Northrop Corporation F/A-18 (fig. 22(c)) at $M_\infty = 0.45$ and $\alpha = 20°$ are illustrated in figure 25. The LVS images correspond to a view aft of the model looking upstream along the model centerline. This experiment provided information on the LEX vortex flow behavior and vortex-tail interactions compared with flight and CFD results obtained in an on-going NASA High-Alpha Technology Program (ref. 17). Reference 9 shows that the LEX vortex breakdown characteristics observed in LVS wind tunnel testing of a 0.06-scale F/A-18 model compare well with in-flight flow visualization results obtained on the full-scale F/A-18 (ref. 18).

The flow features obtained in the 7- by 10-Foot HST at $M_\infty = 0.50$ and $\alpha = 20°$ and in the 8-Foot TPT at $M_\infty = 1.20$ and $\alpha = 20°$ on a generalized Northrop fighter configuration with outboard control surface (OCS) (fig. 22(d)) are shown in figure 26. The photographs reveal the combined wing and OCS leading-edge vortices in the near wake of the model. Symmetric and differential deflections of the OCS

panels were tested to determine their effectiveness as pitch, roll, and yaw control devices. The left-hand OCS panel was intrumented with a three-component strain-gauge balance to measure OCS normal force, bending moment, and hinge moment. The LVS flow visualization was particularly useful in evaluating the induced effects of wing and OCS vortices on OCS force and moment characteristics.

Figure 27 shows the vortex flows about a generalized supersonic fighter/interceptor model (fig. 22(e)) tested in the 8-Foot TPT and observed from the model support system. The photograph in figure 27(a) corresponds to $M_\infty = 0.85$ and $\alpha = 18°$ and reveals the vortices shed from the leading edges of the highly swept wings. Figure 27(b) illustrates the tip vortices from the horizontal tails and the wake from the wing-mounted engine nacelles at $M_\infty = 1.19$ and $\alpha = 9°$. Figures 27(c) and 27(d) illustrate the complexity of the cross flow in the near wake of the model at $M_\infty = 1.19$, $\alpha = 18°$, and $\beta = 8°$ and $-8°$, respectively. The LVS results assisted in the evaluation of a new aircraft design and provided flow-field features to guide CFD computations.

The complex vortex flow-field interactions about a variable-sweep fighter/bomber model (fig. 22(f)) are illustrated in the LVS photographs in figure 28. The flow visualization was conducted in the 8-Foot TPT at Mach numbers of 0.85 and 1.20. The perspective of the LVS images is aft of the model looking upstream along the model centerline. The photographs in figures 28(a) and 28(b) correspond to $M_\infty = 0.85$, $\alpha = 18°$, and $\beta = 0°$ and $-4°$, respectively, at a light-sheet location near the base of the model. The wing leading-edge sweep is approximately 71°, which is shown by the dashed lines in the planform sketch (fig. 22(f)). The vortices shed from forebody, engine inlets, wing gloves, and wing leading edges interact and form a complex cross-flow pattern near the model base. Nonuniform temperature distribution in the tunnel test section caused the vortices on the right side of the model to be brighter compared with those on the left side of the model, as shown in figure 28(a). Partial obstruction in the water flow through the tunnel cooling coils was identified as the source of the nonuniform temperature distribution. The flow-field interactions are also complex at higher Mach numbers. The photographs in figures 28(c) and 28(d) were obtained at $M_\infty = 1.20$, $\alpha = 22°$, and $\beta = 0°$ and $-8°$, respectively. The dark areas above the wings define vortex regions from engine inlet, wing glove, wing leading edge, and horizontal tail. The bright lines of condensation near the centerline vertical tail are caused by high flow veloc-ities induced by the vortical flows. Condensation of water vapor in the free stream provides good definition of the outer edges of the laser light sheet in figures 28(c) and 28(d). The LVS results were used in the evaluation of aerodynamic, stability, and control characteristics of this aircraft configuration for a wide range of simulated flight conditions.

The wing leading-edge vortex cross sections in the wake region of a generic high-speed civil transport (HSCT) model (fig. 22(g)) at $M_\infty = 0.90$ and $\alpha = 9°$ are shown in figure 29. The flow visualization was performed in the 8-Foot TPT to assess the aerodynamics of a supersonic transport configuration at off-design conditions and to compare CFD-computed flow fields.

Concluding Remarks

Laser vapor screen (LVS) flow visualization systems that are fiber-optic based have been developed and installed for aerodynamic research in the Langley 8-Foot Transonic Pressure Tunnel and the Langley 7- by 10-Foot High-Speed Tunnel. These facilities feature a plenum shell that surrounds the test section and an operating environment within the plenum that poses severe operational concerns for a laser source. The use of fiber optics allows the laser source to be located outside the plenum and simultaneously provides a safe and reliable means of delivering the laser beam over a significant distance to the light-sheet-generating optics inside the plenum. The Langley Research Center LVS systems expand the use of fiber optics in conjunction with a laser light-sheet flow visualization method to larger scale subsonic and transonic facilities that have limited access to the test section and the harsh operating environments for laser-based systems. The LVS systems have been effectively used to visualize the vortex-dominated flows about numerous advanced aircraft configurations at low subsonic through supersonic speeds. Experience has shown that the LVS method works well when the local flow is in the compressible regime. The high local velocities induced by vortical flows, for example, promote good condensation patterns even at low subsonic free-stream speeds. The flow visualization results complement the model force and moment and surface static pressure measurements that are typically obtained in wind tunnel tests. The LVS results also improve the understanding of trends in aerodynamic, stability, and control characteristics.

Results from 3 years of operating experience in the Langley Research Center wind tunnels suggest that the use of fiber optics yields a thinner and more uniform light sheet and requires lower laser output power to achieve satisfactory flow features compared

with a free-expanding laser beam steered by mirrors. The alignment of the laser beam to the fiber optic core is maintained indefinitely. In addition, the fiber optic system is insensitive to large vibrations caused by tunnel operation at high speeds and to variations in tunnel temperature and pressure. These features increase wind tunnel productivity by decreasing setup time and eliminating problems during operation. The compactness of the fiber optics and light-sheet-generating package facilitates the installation and the implementation of LVS systems in larger scale wind tunnel facilities. Most importantly, the use of fiber optics represents a significant advancement in laser safety.

NASA Langley Research Center
Hampton, VA 23681-0001
November 2, 1993

References

1. Allen, H. Julian; and Perkins, Edward W.: *A Study of Effects of Viscosity on Flow Over Slender Inclined Bodies of Revolution.* NACA Rep. 1048, 1951. (Supersedes NACA TN 2044.)

2. McGregor, I.: The Vapor-Screen Method of Flow Visualization. *J. Fluid Mech.*, vol. 11, pt. 4, Dec. 1961, pp. 481–511.

3. Keener, Earl R.: *Flow-Separation Patterns on Symmetric Forebodies.* NASA TM-86016, 1986.

4. Verhaagen, N. G.: An Experimental Investigation of the Vortex Flow Over Delta and Double-Delta Wings at Low Speed. *Aerodynamics of Vortical Type Flows in Three Dimensions*, AGARD-CP-342, July 1983, pp. 7-1–7-16.

5. Payne, F. M.; Ng, T. T.; Nelson, R. C.; and Schiff, L. B.: Visualization and Flow Surveys of the Leading Edge Vortex Structure on Delta Wing Planforms. AIAA-86-0330, Jan. 1986.

6. Kjelgaard, Scott O.; Sellers, William L., III; and Weston, Robert P.: Flowfield Survey Over a 75° Swept Delta Wing at an Angle of Attack of 20.5°. AIAA-86-1775, June 1986.

7. Erickson, Gary E.; and Rogers, Lawrence W.: *Effects of Forebody Strakes and Mach Number on Overall Aerodynamic Characteristics of Configuration With 55° Cropped Delta Wing.* NASA TP-3253, 1992.

8. Erickson, Gary E.: *Wind Tunnel Investigation of the Interaction and Breakdown Characteristics of Slender-Wing Vortices at Subsonic, Transonic, and Supersonic Speeds.* NASA TP-3114, 1991.

9. Erickson, Gary E.: *Wind Tunnel Investigation of Vortex Flows on F/A-18 at Subsonic Through Transonic Speeds.* NASA TP-3111, 1991.

10. Hecht, Jeff: *Understanding Fiber Optics.* Howard W. Sams & Co., 1987.

11. Erickson, Gary E.; and Murri, Daniel G.: Forebody Strakes for High-Angle-of-Attack Vortex Flow Control: Mach Number and Strake Planform Effects. *High-Angle-of-Attack Technology*, Volume I, Joseph R. Chambers, William P. Gilbert, and Luat T. Nguyen, eds., NASA CP-3149, Part 1, 1992, pp. 381–480.

12. Staff, Performance Aerodynamics Section: *A Description of the NASA-Langley Eight-Foot Transonic Pressure Tunnel.* NASA Langley Research Center, Nov. 1973.

13. Fox, Charles H., Jr.; and Huffman, Jarrett K.: *Calibration and Test Capabilities of the Langley 7- by 10-Foot High Speed Tunnel.* NASA TM X-74027, 1977.

14. *Nonionizing Radiation.* LHB 1710.8, NASA Langley Research Center, Sept. 1982.

15. Campbell, James F.; Chambers, Joseph R.; and Rumsey, Christopher L.: Observation of Airplane Flow Fields by Natural Condensation Effects. AIAA-88-0191, Jan. 1988.

16. *Precision Laser & Optics Products.* Newport Corp., c.1989.

17. Gilbert, William P.; and Gatlin, Donald H.: Review of the NASA High-Alpha Technology Program. *High-Angle-of-Attack Technology*, Volume I, Joseph R. Chambers, William P. Gilbert, and Luat T. Nguyen, eds., NASA CP-3149, Part 1, 1992, pp. 23-59.

18. Fisher, David F.; Del Frate, John H.; and Richwine, David M.: *In-Flight Flow Visualization Characteristics of the NASA F-18 High Alpha Research Vehicle at High Angles of Attack.* NASA TM-4193, 1990.

Light plane

Light source

Video and
still cameras

Video camera

Figure 1. Sketch of representative vapor screen flow visualization installation.

(a) $M_\infty = 0.90$; $\alpha = 20°$.
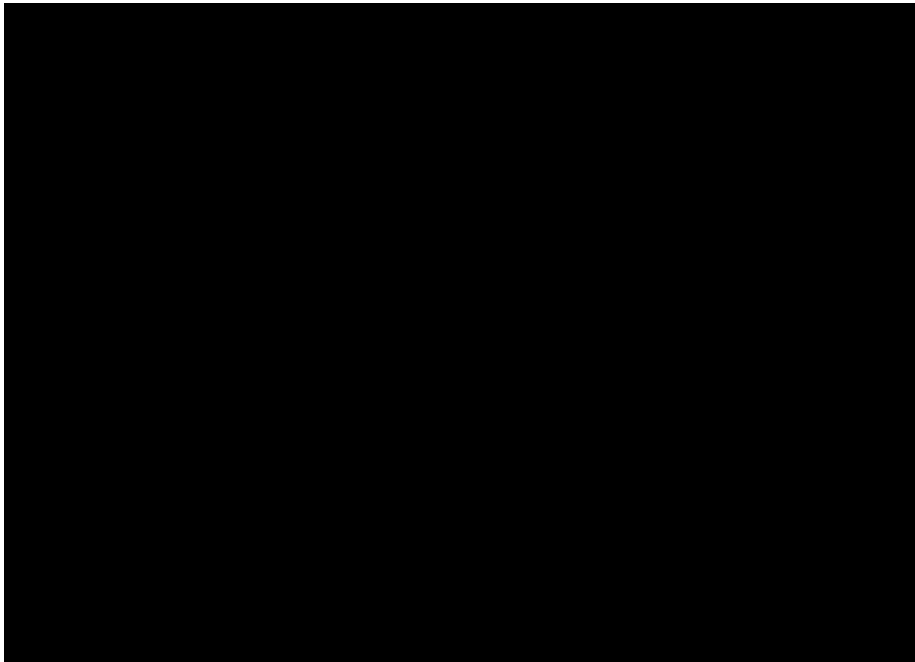
(b) $M_\infty = 1.05$; $\alpha = 24°$.

Figure 2. Laser vapor screen flow visualization on 55° cropped delta wing model in 7- by 10-Foot Transonic Tunnel at David Taylor Research Center (ref. 7).
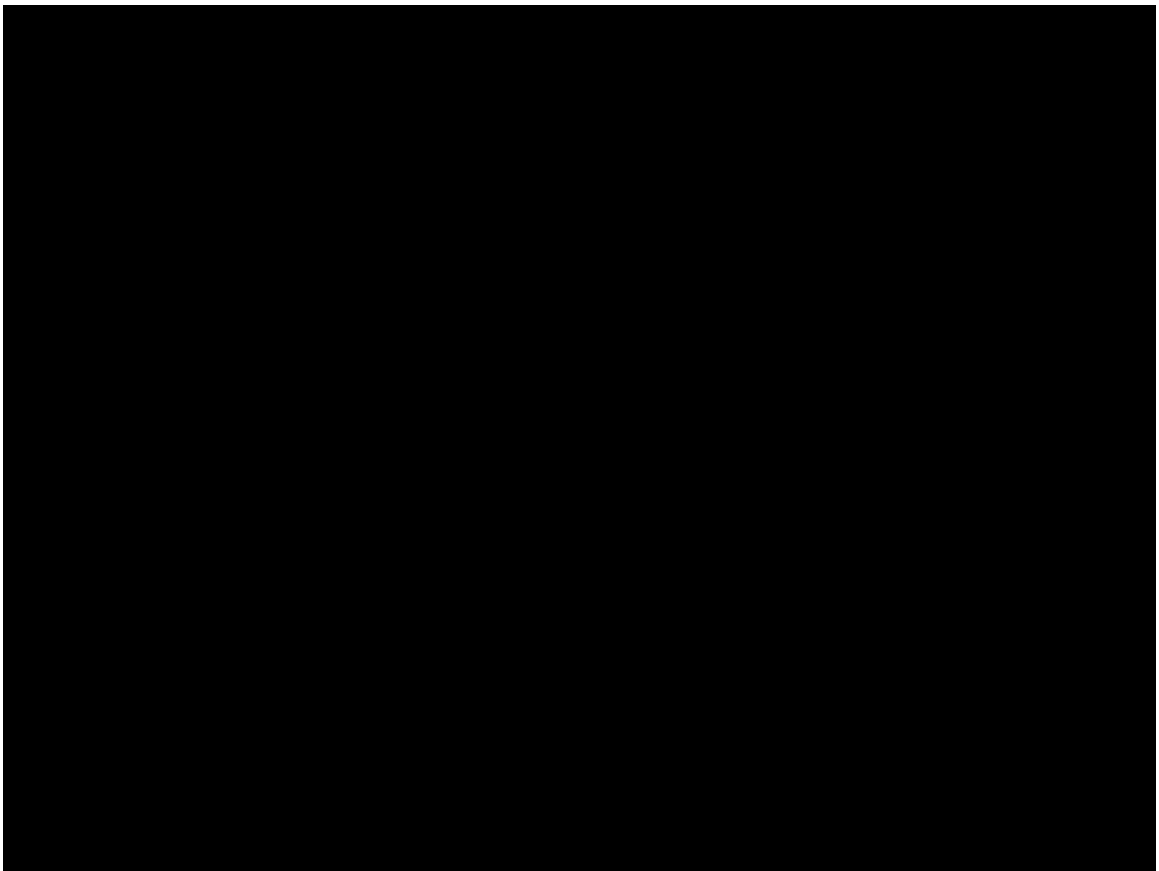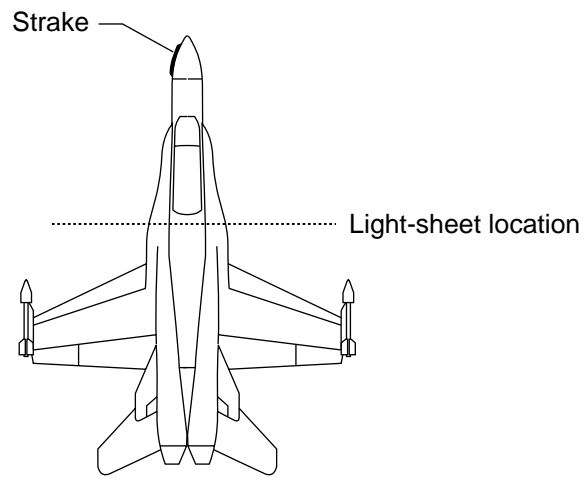
Light-sheet location
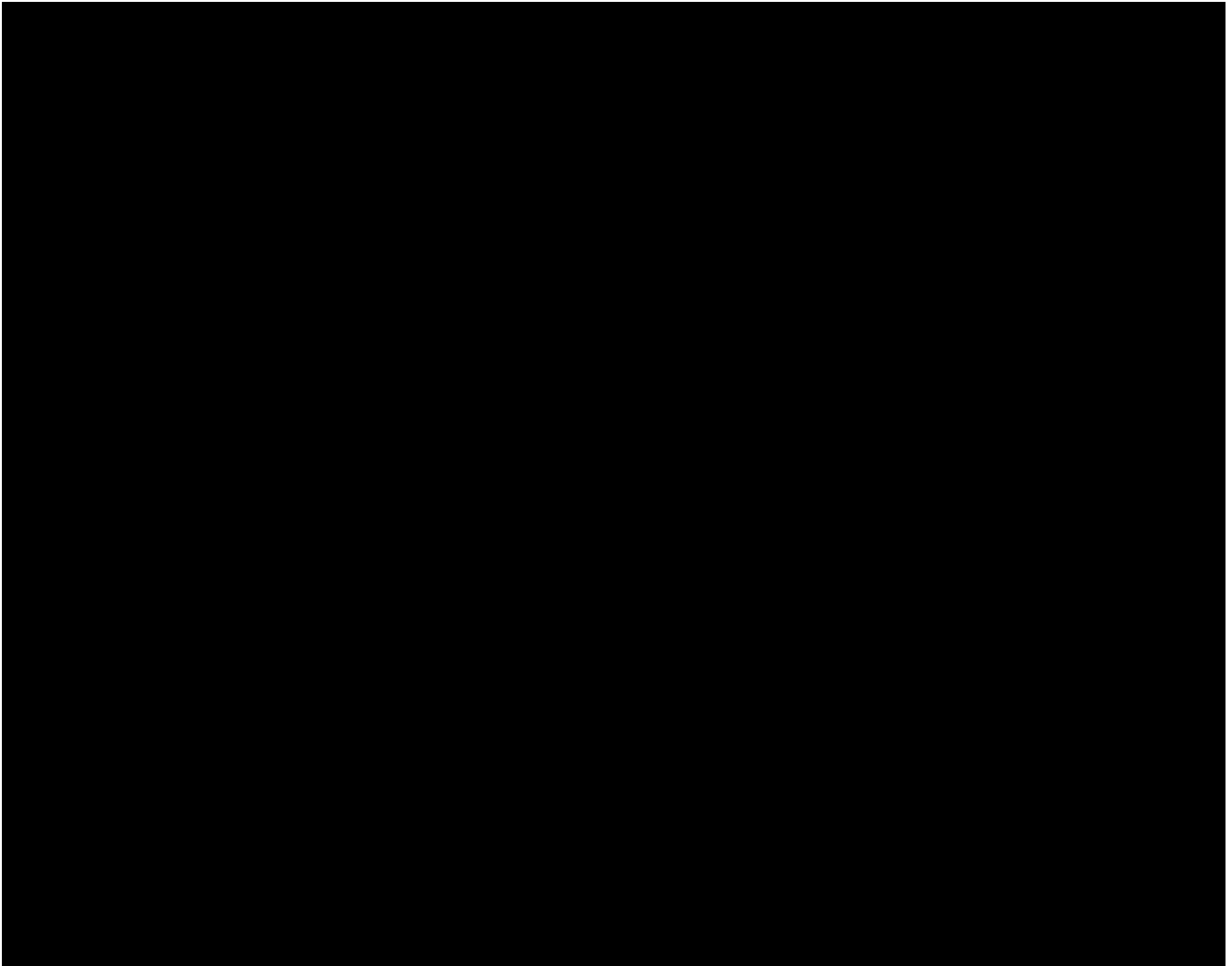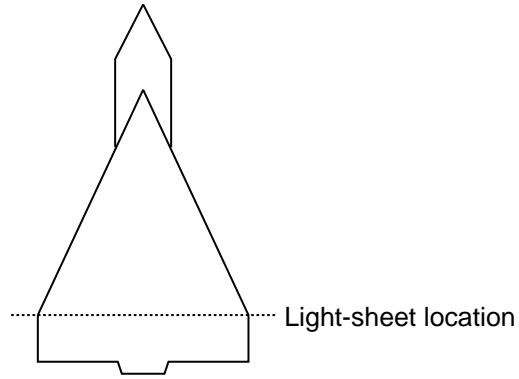
(a) $M_\infty = 0.60$; $\alpha = 16°$.

Figure 3. Laser vapor screen flow visualization on 65° cropped delta wing-LEX model in 6- by 6-Foot Supersonic Wind Tunnel at Ames Research Center (ref. 8).

Light-sheet location
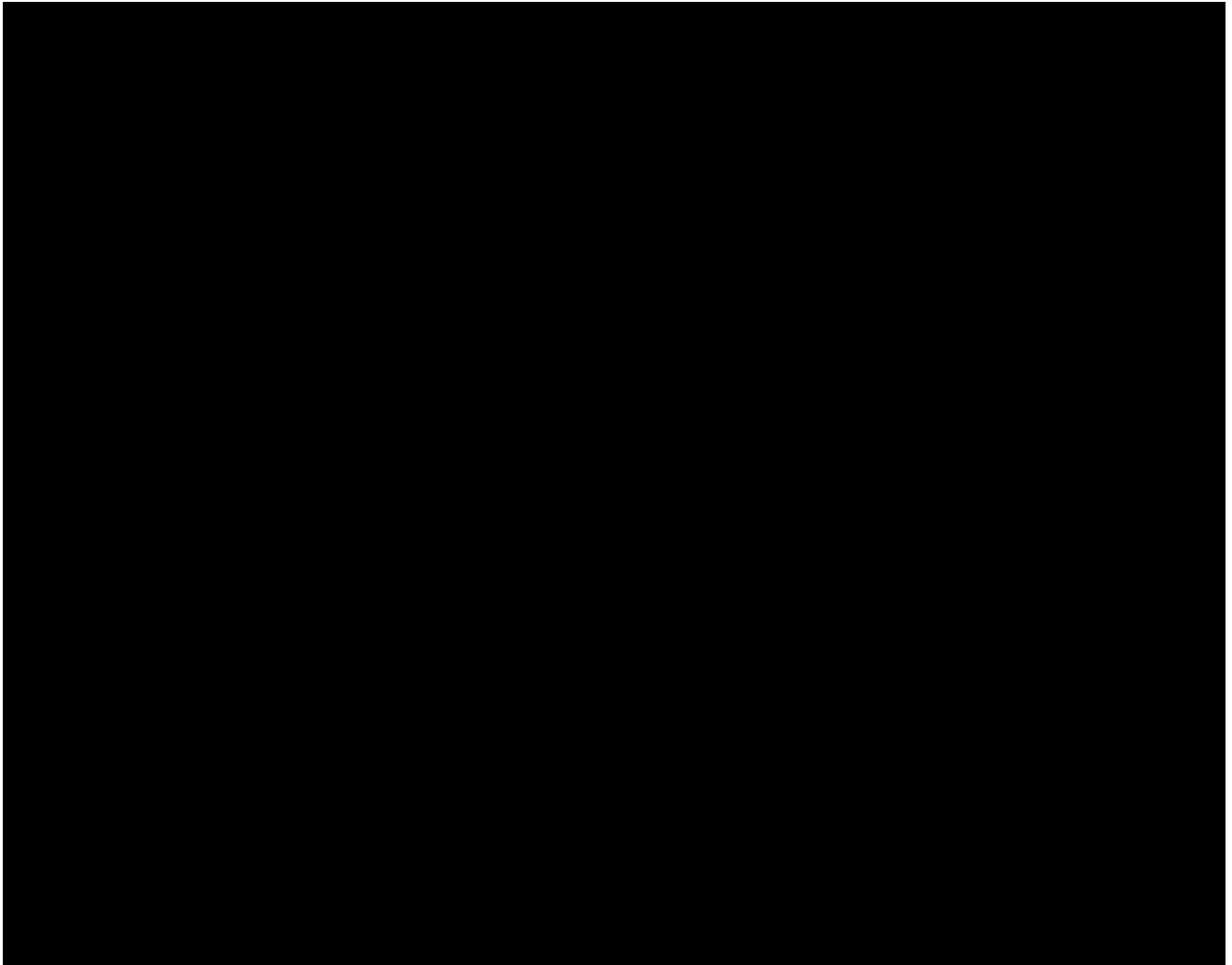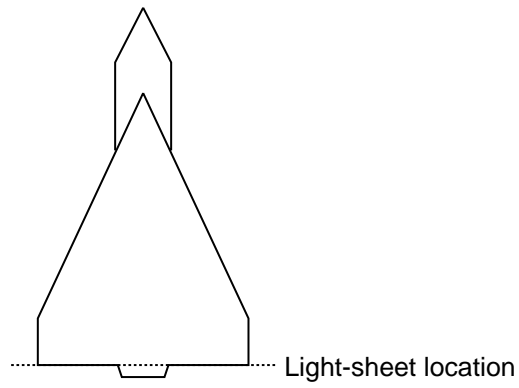
(b) $M_\infty = 0.85$; $\alpha = 20°$.

Figure 3. Concluded.

Light-sheet location
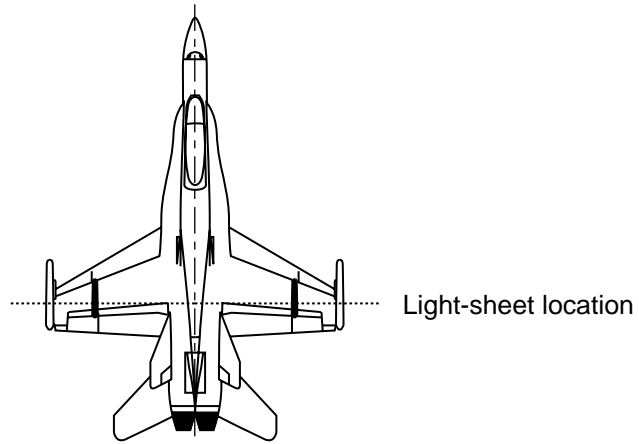
(a) $M_\infty = 0.60;\ \alpha = 20°$.

Figure 4. Laser vapor screen flow visualization on 0.06-scale F/A-18A model in 7- by 10-Foot Transonic Tunnel at David Taylor Research Center (ref. 9).

Light-sheet location
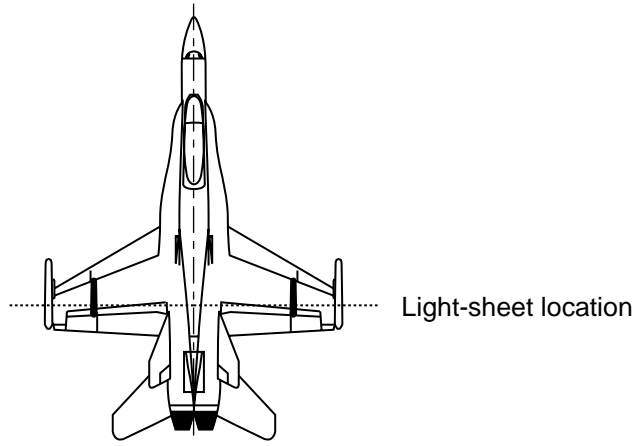
(b) $M_{\infty} = 0.60$; $\alpha = 25°$.

Figure 4. Concluded.

Strake

Light-sheet location
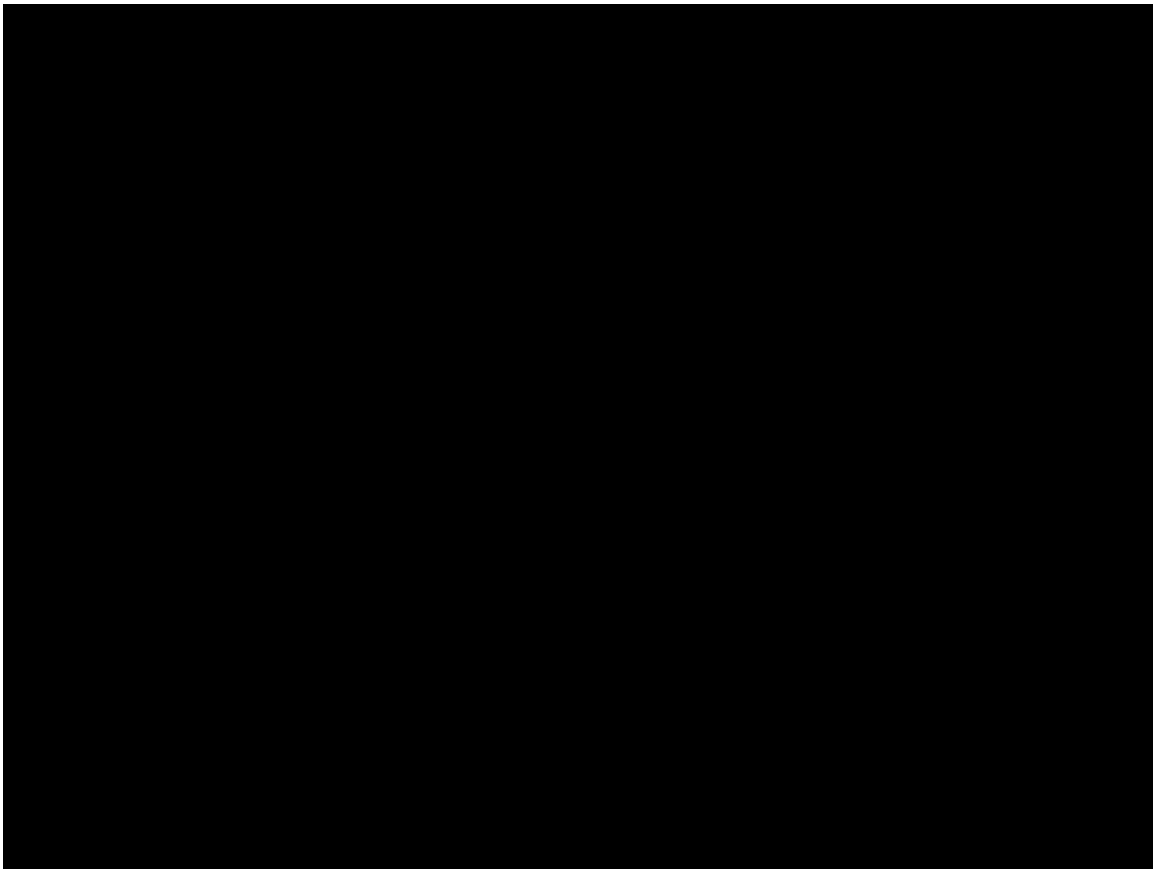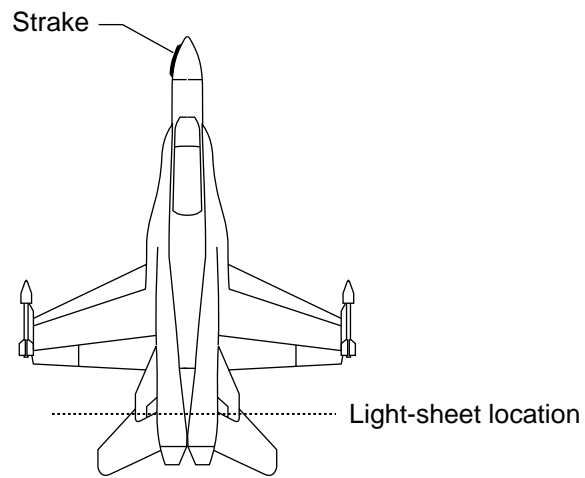
(a) $M_\infty = 0.80$; $\alpha = 20°$.

Figure 5. Fiber-optic-based LVS flow visualization on 0.06-scale F/A-18A model in 7- by 10-Foot Transonic Tunnel at David Taylor Research Center (ref. 11).

Strake

Light-sheet location

(b) $M_\infty = 0.80$; $\alpha = 40°$.

Figure 5. Concluded.

150-gal
water supply tank

Penetration through plenum shell

Atomizer
nozzles (6)
in diffuser
ceiling

Fiber optic cable

Laser

Laser room (external to
plenum shell)

Full-cone
spray pattern

Test section ceiling window

Rotating mirror

Light-sheet
optics

Manifold

Beginning
of diffuser
section

Plenum
shell

Light sheet

Airflow

Note: Test section
ceiling and floor
slots not shown

Test section window

Arc sector

Video camera
outside test section

Miniature video camera
on model sting support system

Figure 9. Sketch of fiber-optic-based LVS system in Langley 8-Foot Transonic Pressure Tunnel.

City water supply
inlet flow

→
Denotes water
flow direction

50-gal water tank

1-hp pump

Heat exchanger

Laser head

Laser-to-fiber coupler

③

City
water
to
drain

① Fiber optic cable

② Umbilical
line

④

Cable penetration
through plenum shell

Closed-loop cooling
water supply from
heat exchanger to laser
(①,②,③,④)

Laser power supply
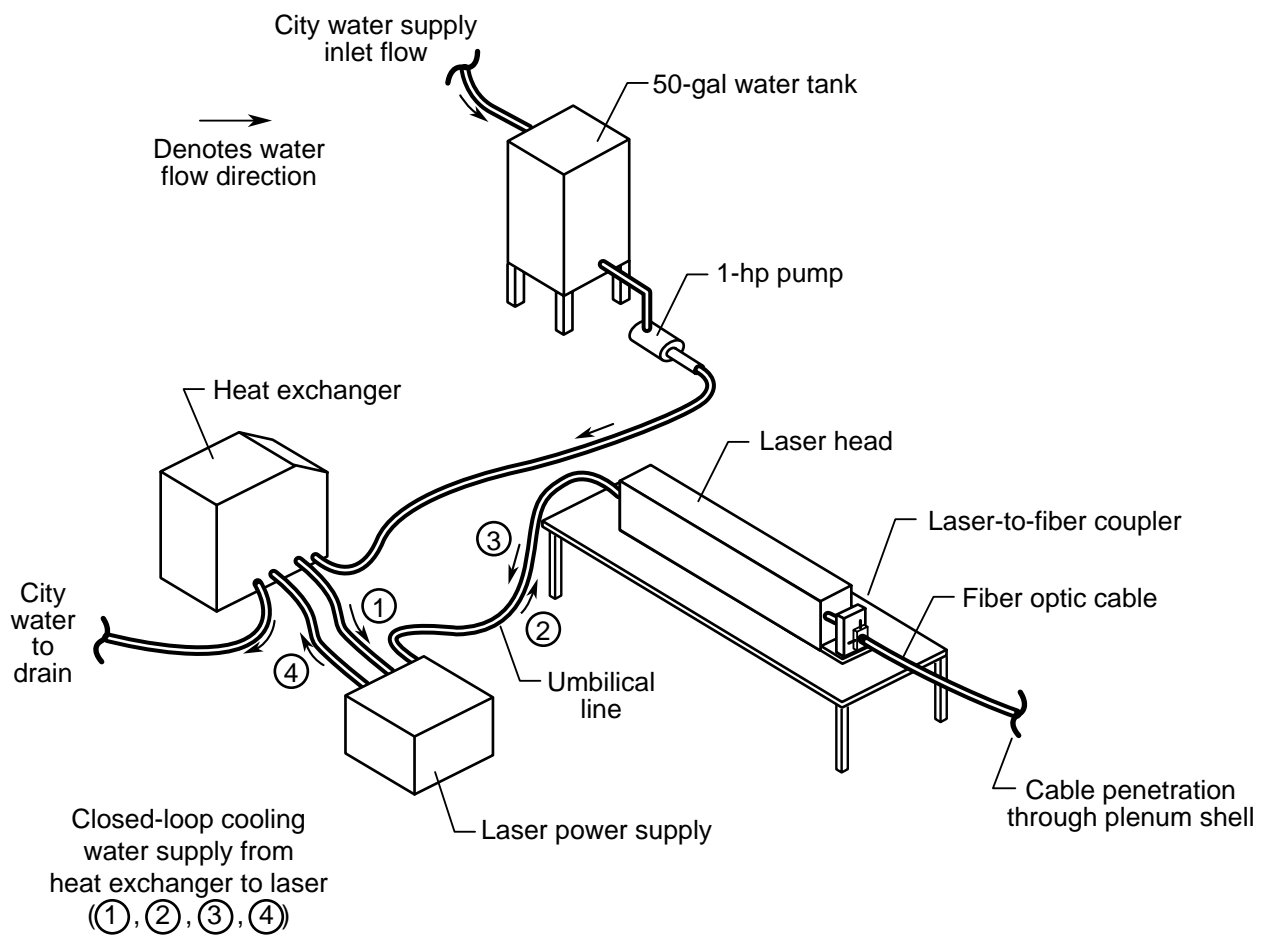
Figure 10. Sketch of laser room layout.

33
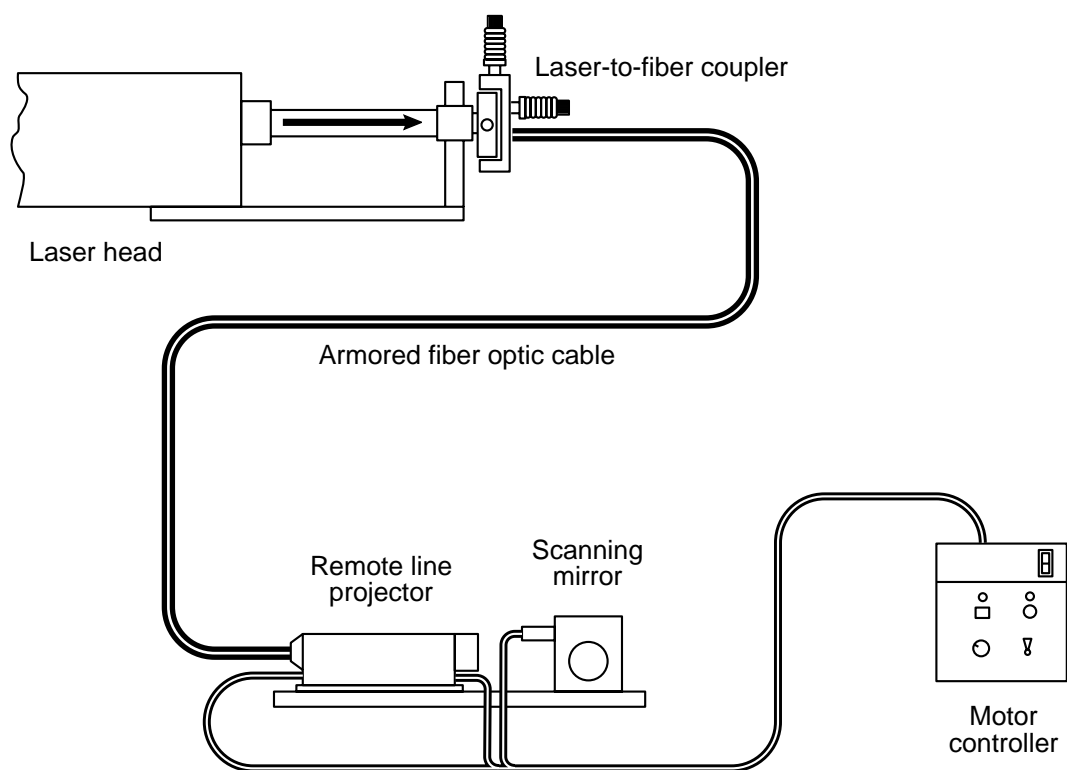
Figure 14. Sketch of fiber-optic-based beam delivery system.
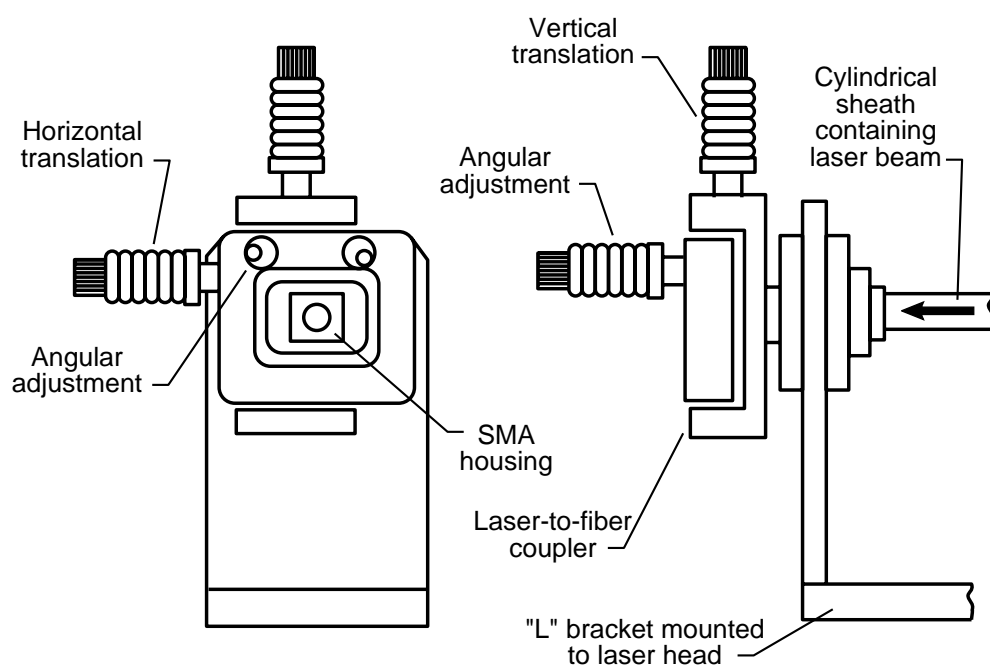
Figure 15. Sketch of laser-to-fiber coupler.

Transmission loss

——— 0.0073 dB/ft
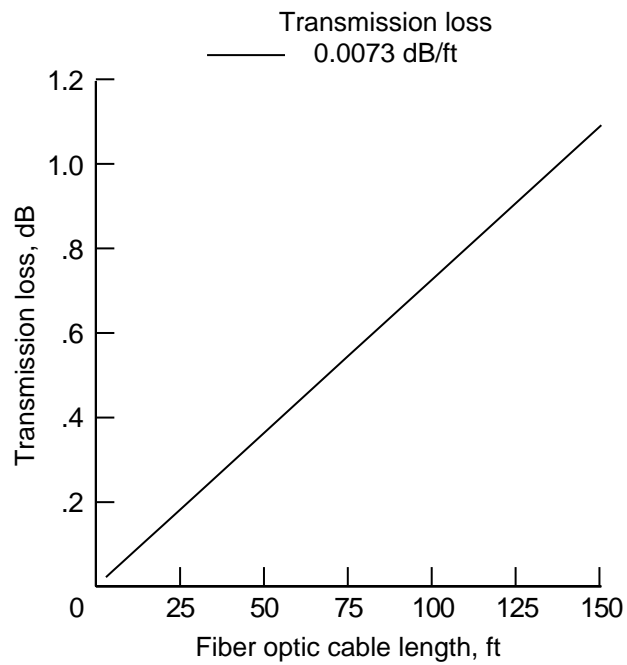
(a) Effect on transmission loss.

Fiber optic throughput

——— From equation (1) (ref. 10)
– – – Additional losses
● LaRC 7- by 10-Foot HST
■ LaRC 8-Foot TPT
◆ DTRC 7- by 10-Foot TT
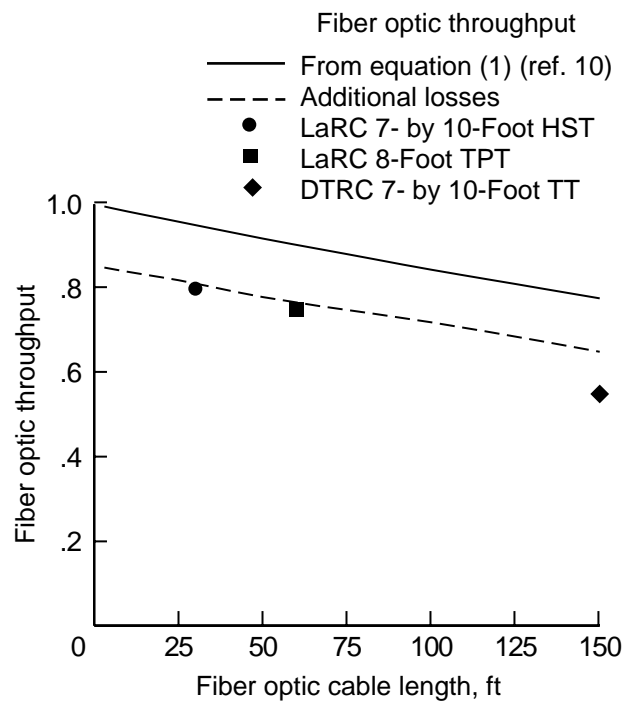
(b) Effect on fiber optic throughput.

Figure 17. Effects of fiber optic cable length on transmission loss and fiber optic throughput.
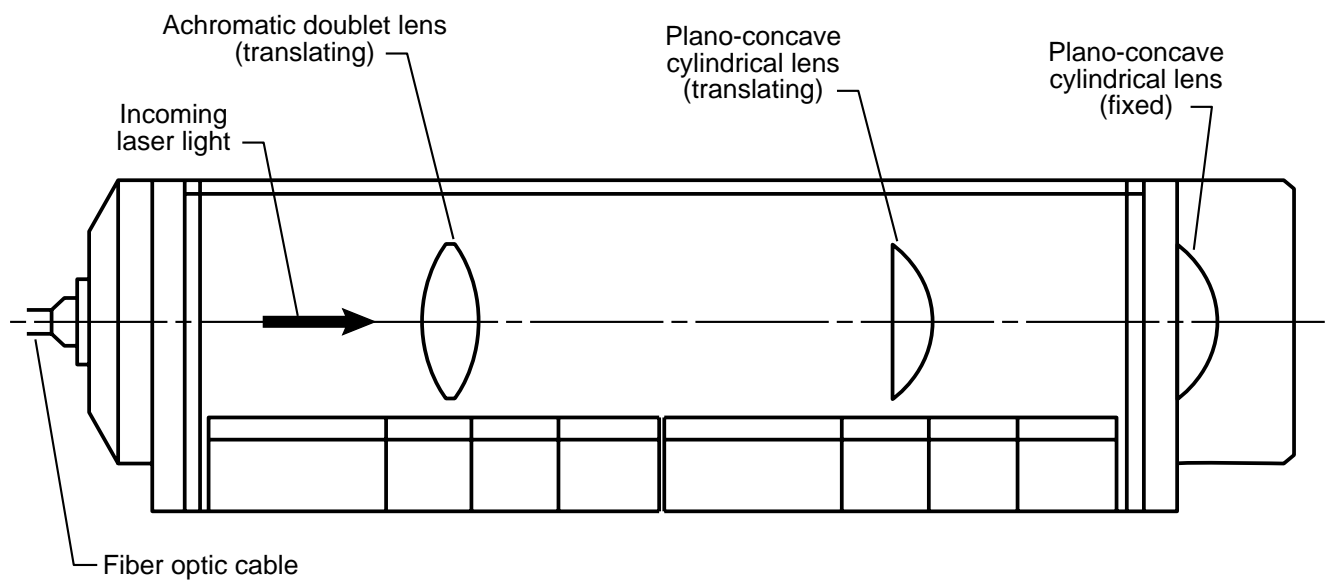
Figure 18. Sketch of line projector optics.
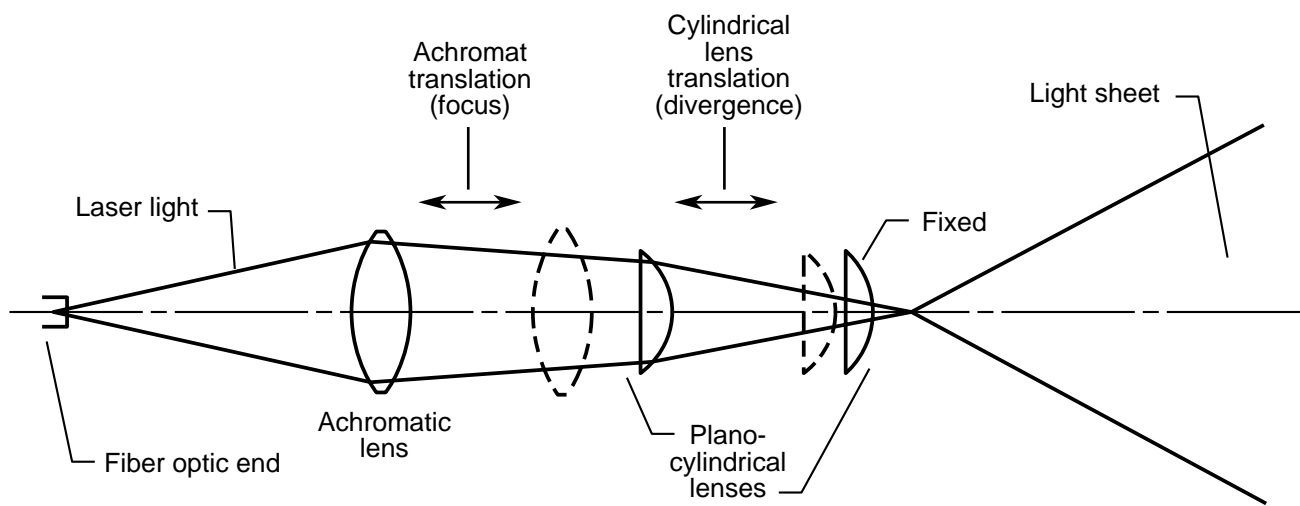
(a) Planview of optics arrangement.
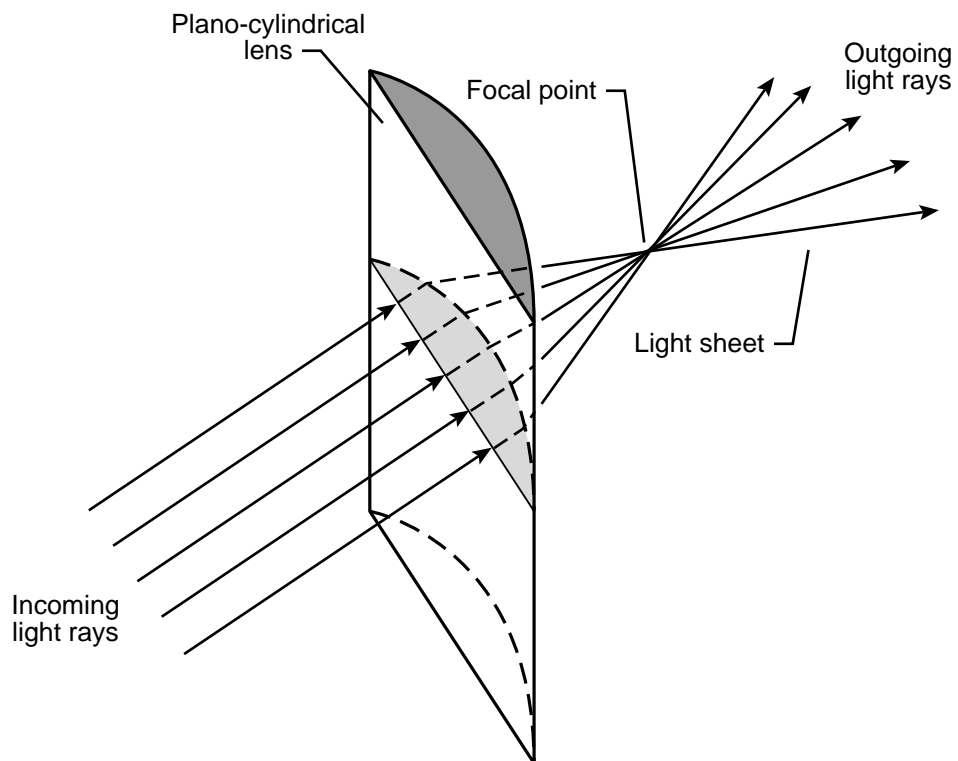
(b) Isometric view of light-sheet generation.

Figure 19. Sketch of light-sheet generation.
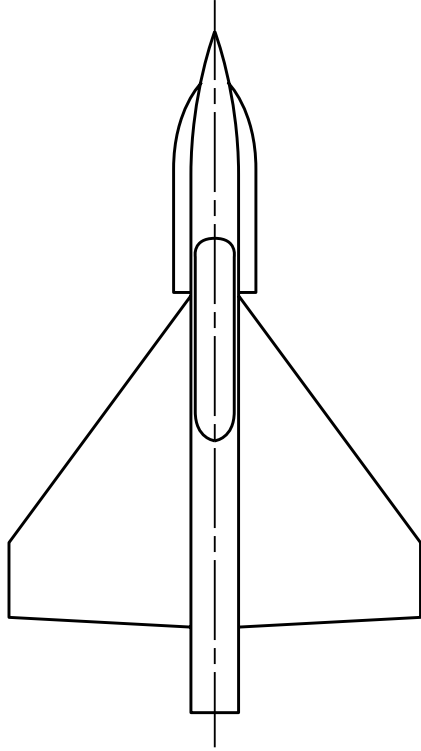
(a) 55° cropped delta wing.
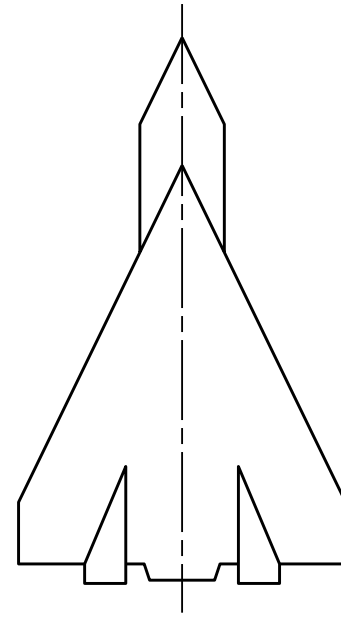
(b) 65° cropped delta wing-LEX.
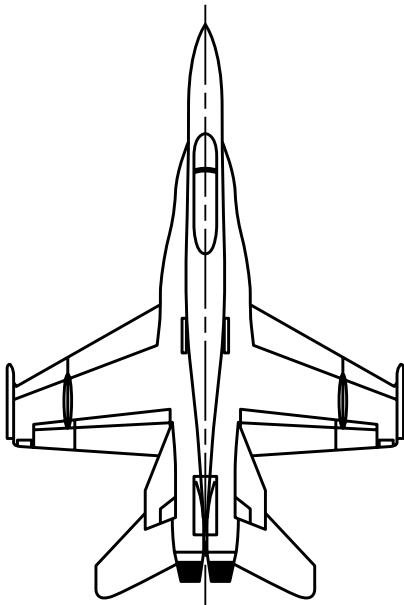
(c) F/A-18A.
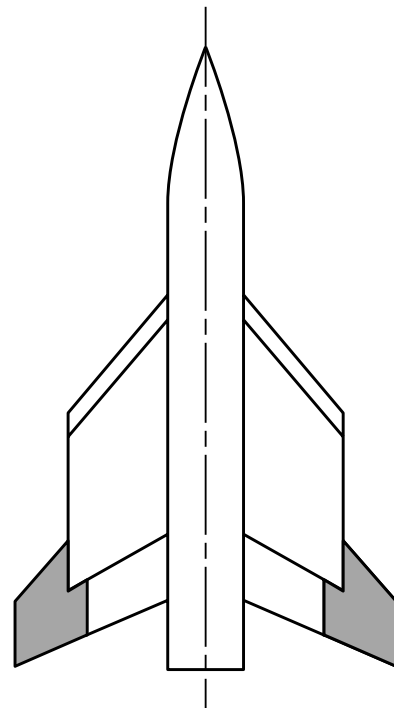
(d) Outboard control surface wing.

Figure 22. Wind tunnel model planform sketches. (Sketches are not to scale.)
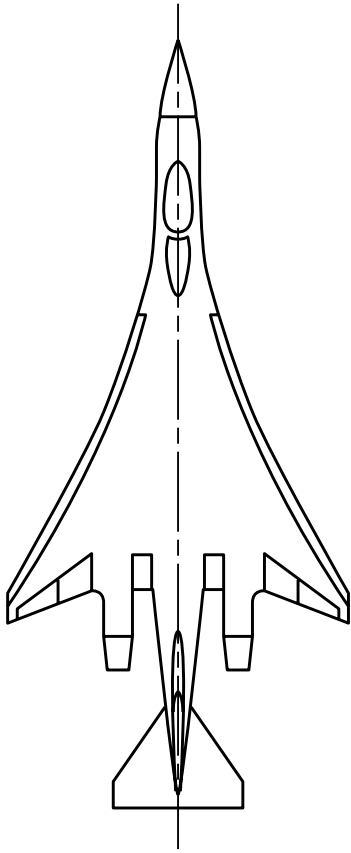
(e) Supersonic fighter/interceptor.
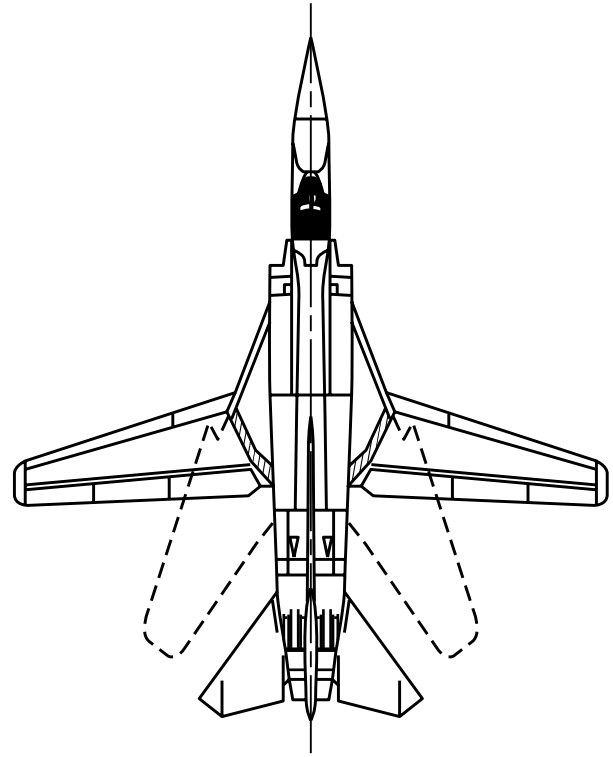
(f) Variable-sweep fighter/bomber.
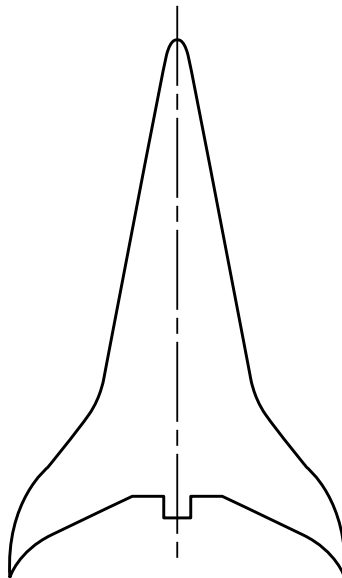
(g) Generic high-speed civil transport.

Figure 22. Concluded.

Light-sheet location
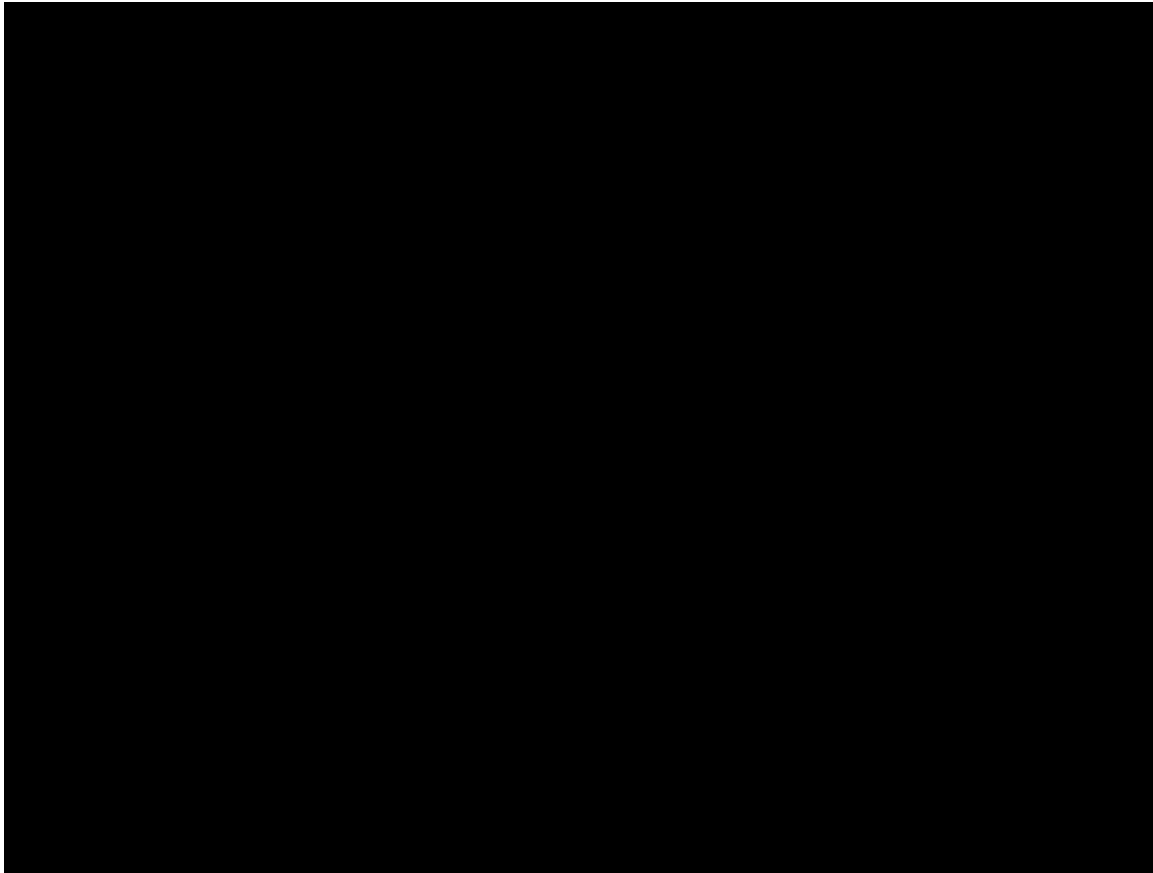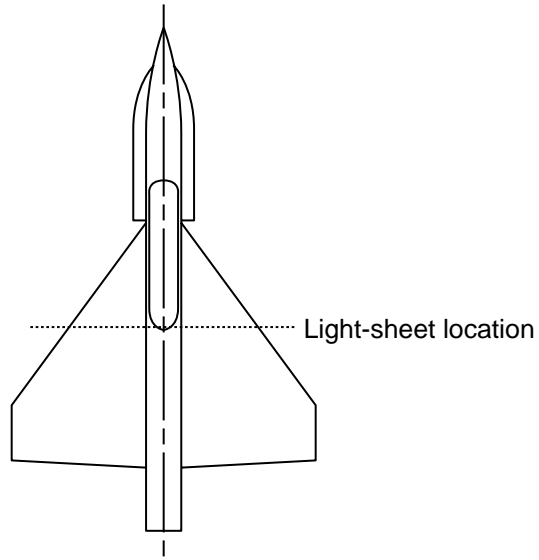
(a) Strake and wing vortices.

Figure 23. LVS results of 55° cropped delta wing model at $M_\infty = 0.40$ and $\alpha = 20°$ from Langley 7- by 10-Foot High-Speed Tunnel.

Light-sheet location
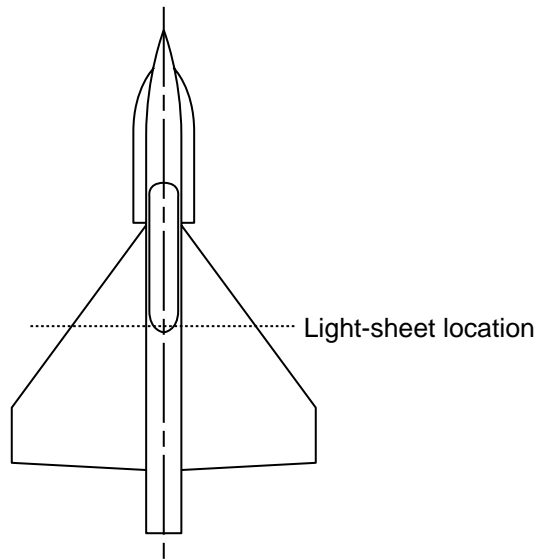
(b) Close-up view of strake and wing vortices.

Figure 23. Continued.

Light-sheet location
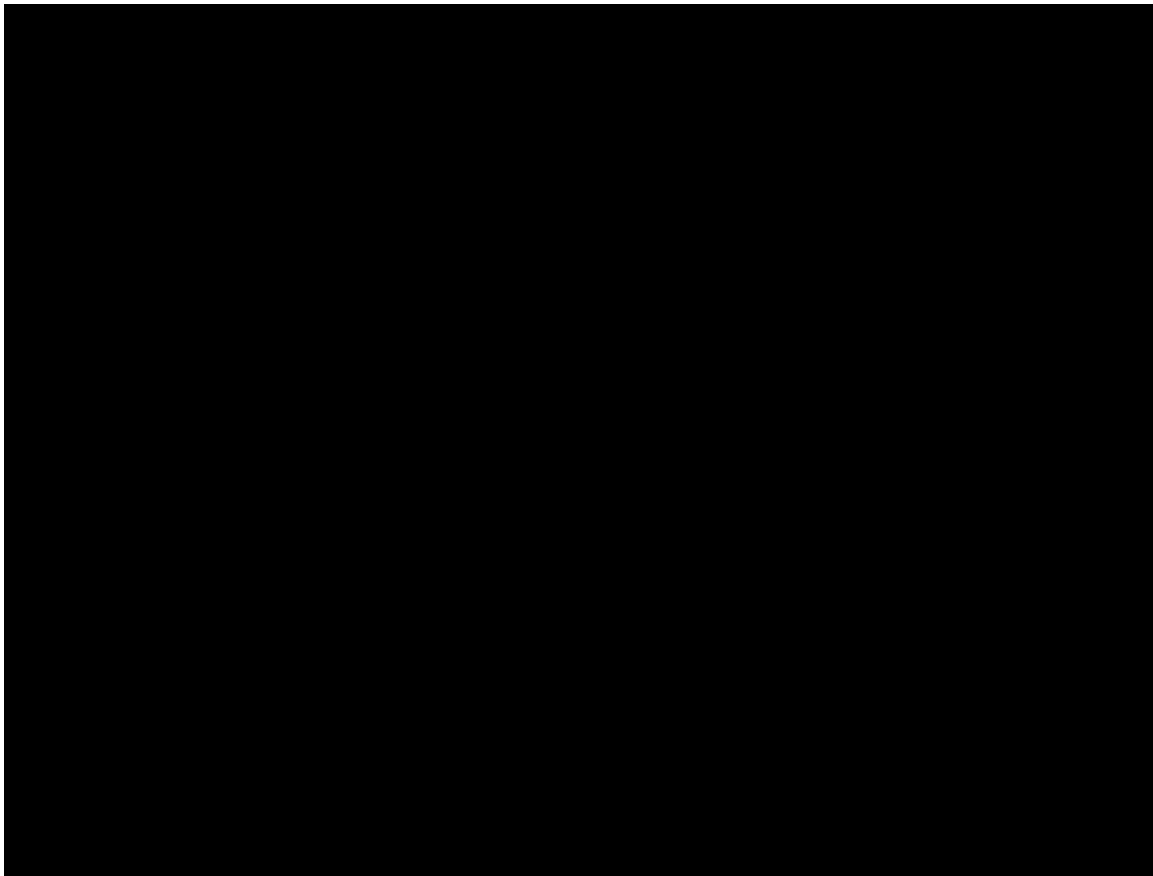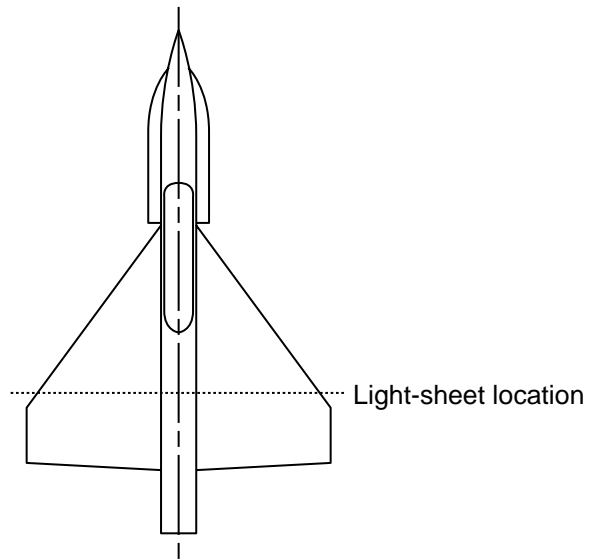
(c) Interacting vortices and wing vortex breakdown.

Figure 23. Concluded.

.... Light-sheet location
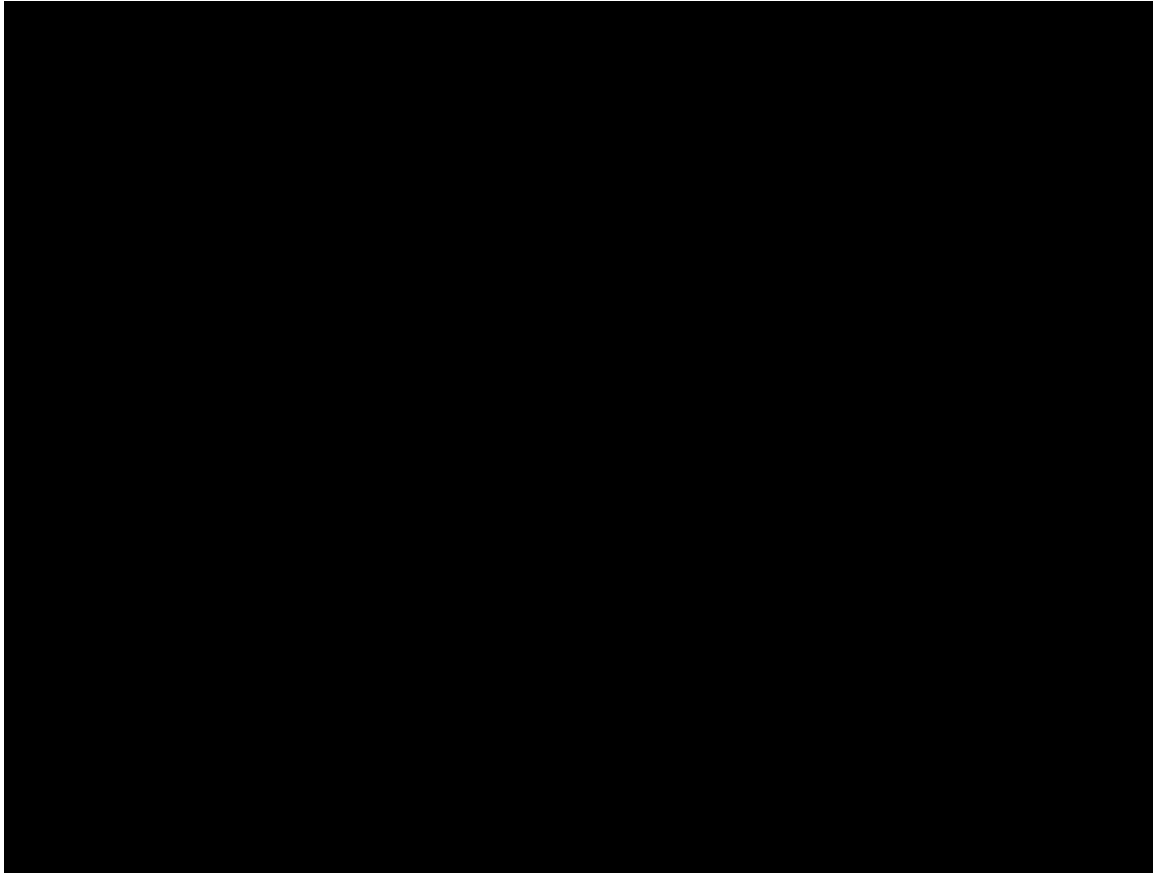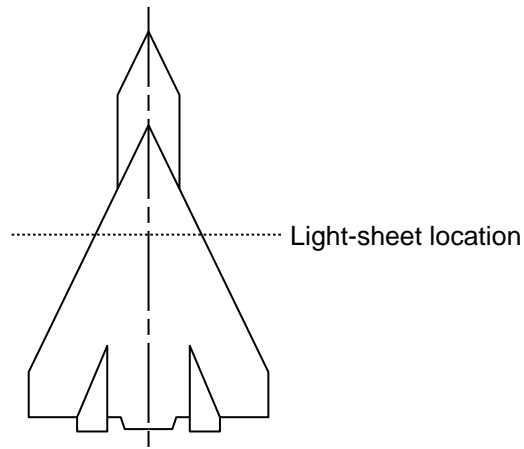
(a) Wing and LEX vortex flows.

Figure 24. LVS results of 65° cropped delta wing-LEX model at $M_\infty = 0.50$ and $\alpha = 25°$ from Langley 7- by 10-Foot High-Speed Tunnel.
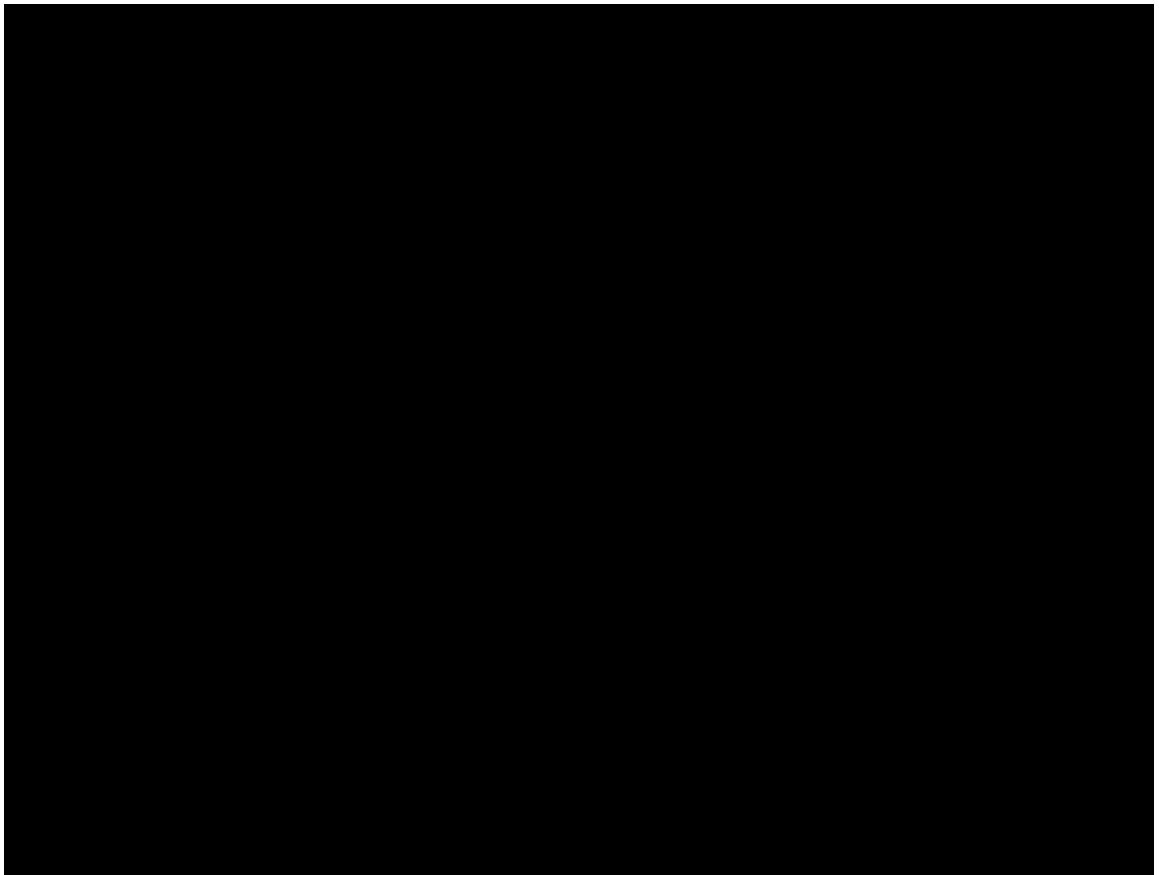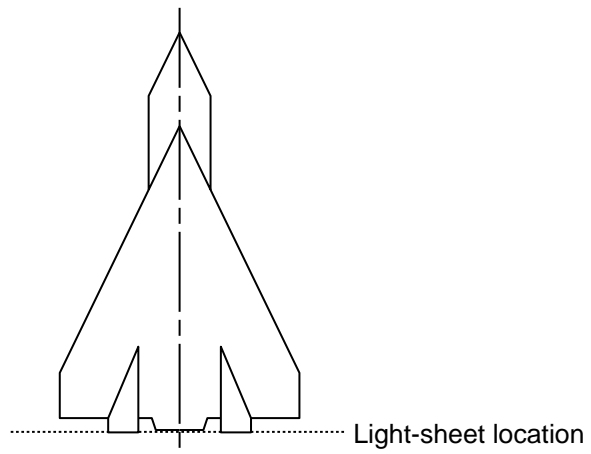
Light-sheet location
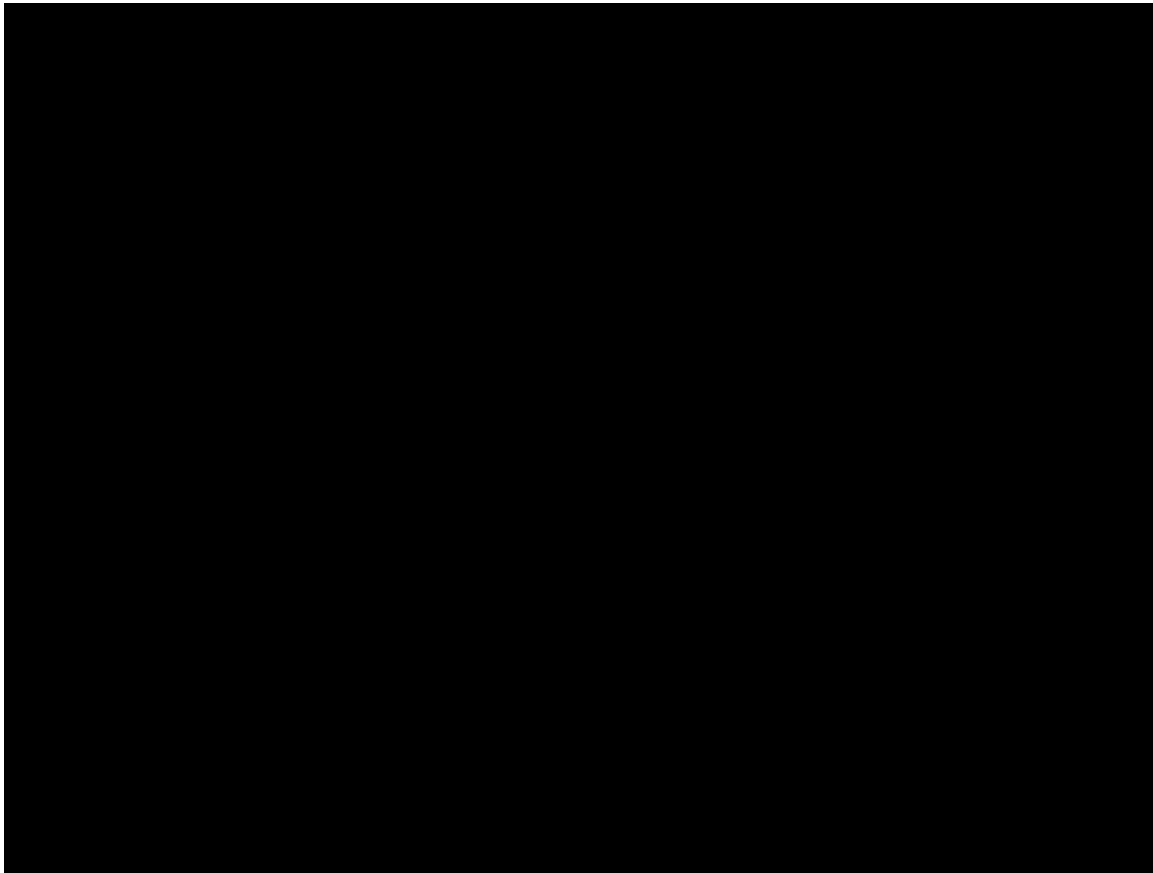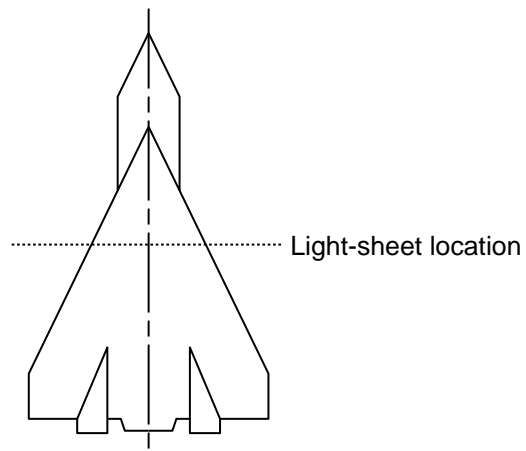
(b) Close-up view of wing and LEX vortex flows.

Figure 24. Continued.

Light-sheet location
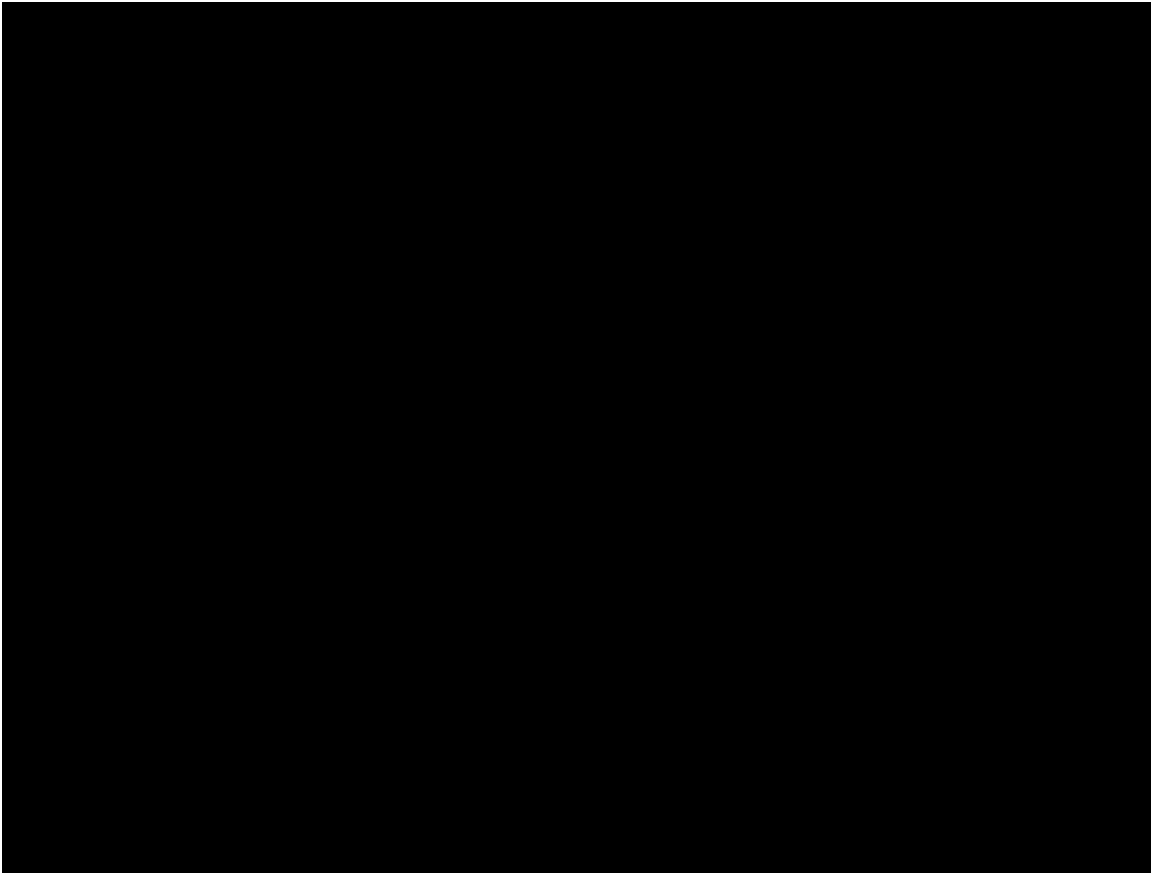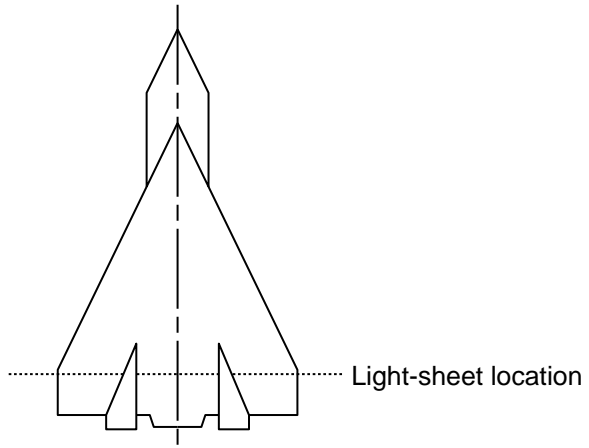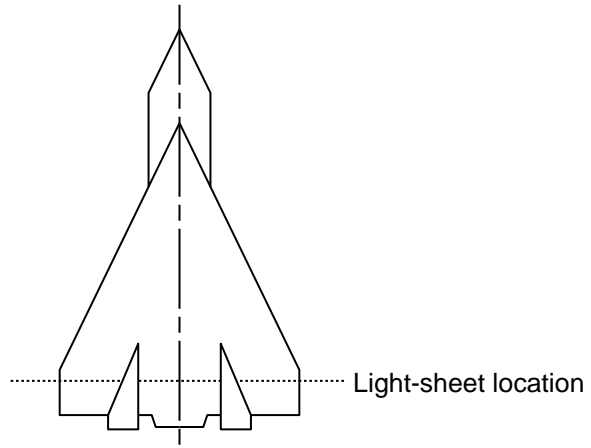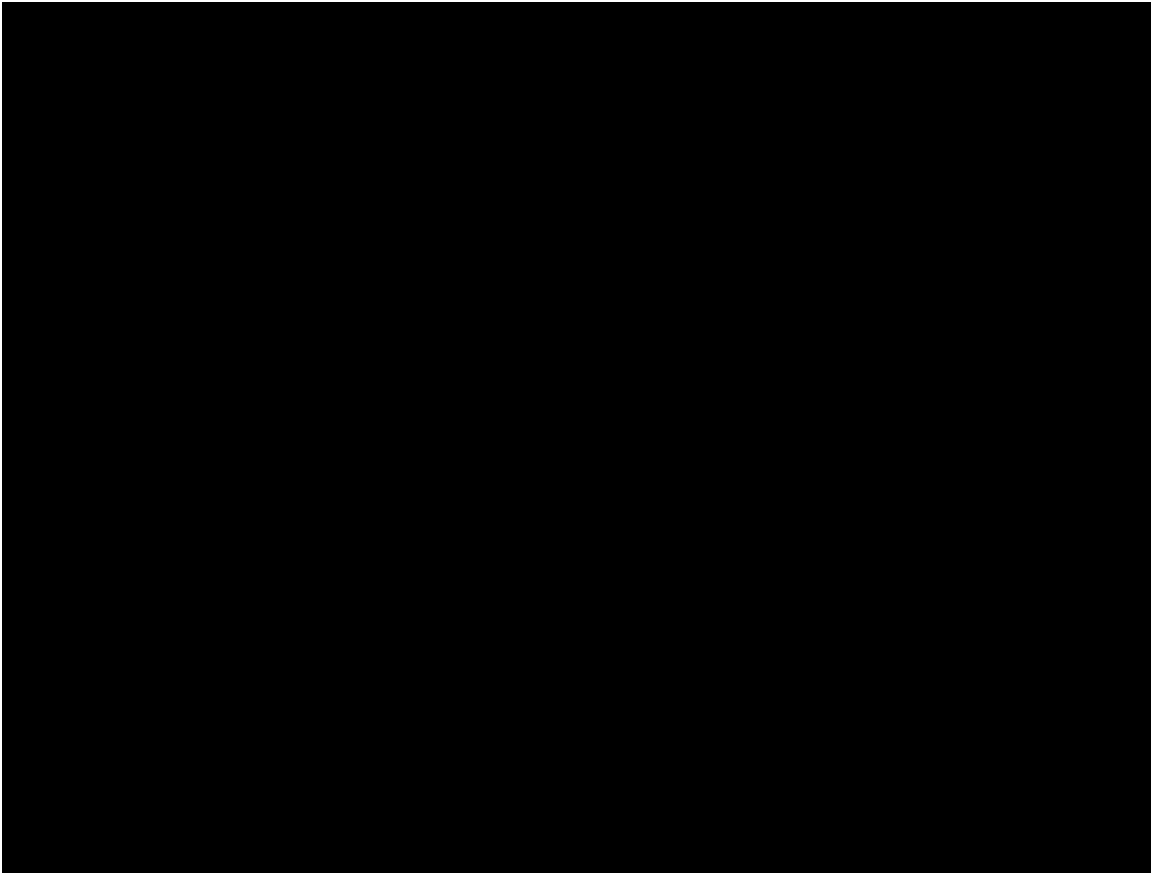
(c) Vortex-vortex and vortex-tail interactions at tails.

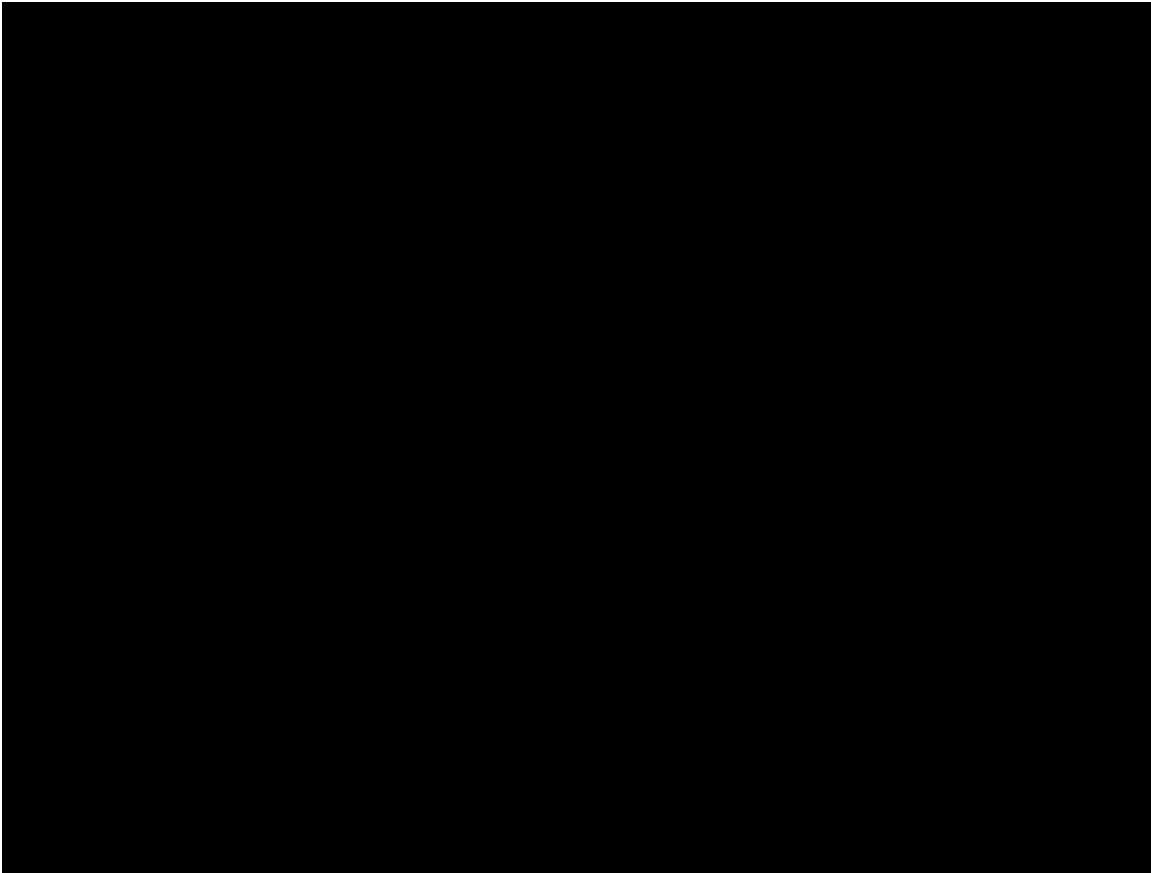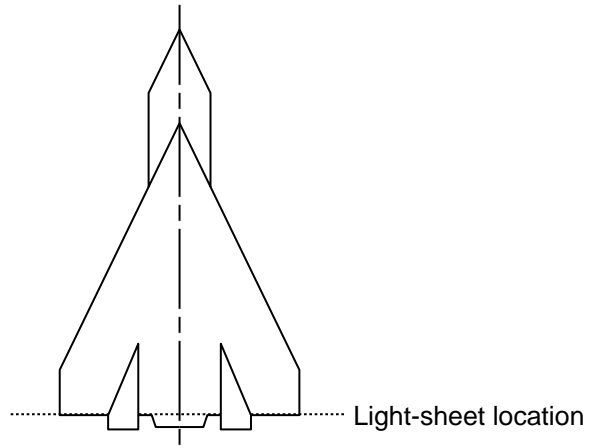Figure 24. Continued.

Light-sheet location

(d) Vortex-vortex and vortex-tail interactions aft of tails.

Figure 24. Continued.

Light-sheet location

(e) Vortex-vortex and vortex-tail interactions near tail apex.

Figure 24. Continued.

Light-sheet location
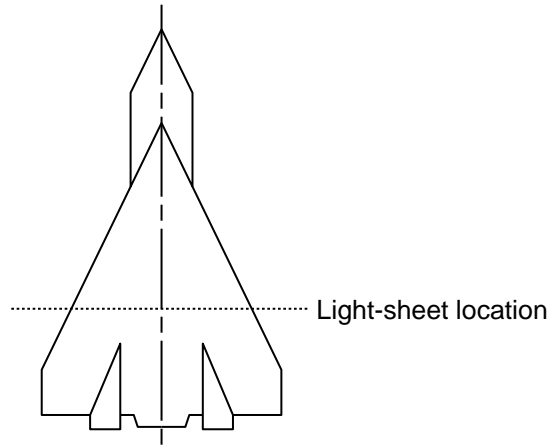
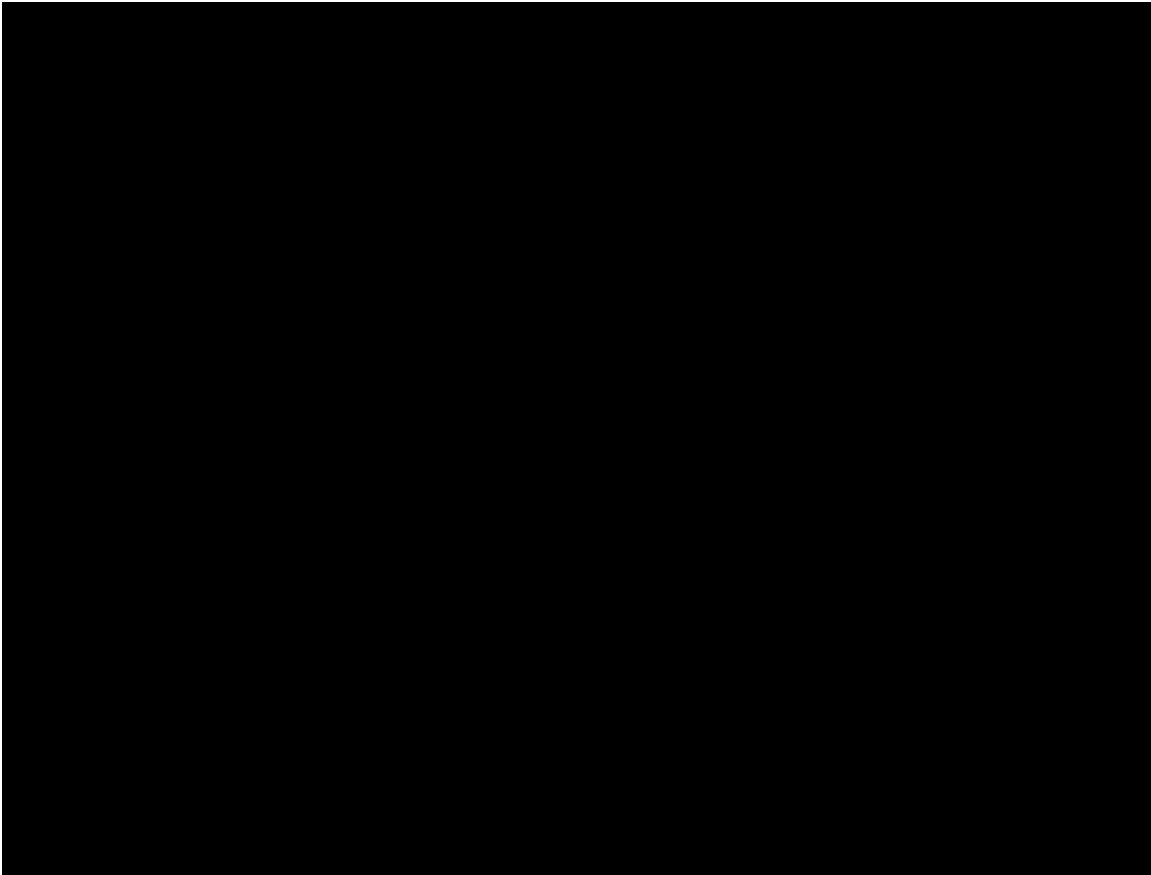(f) Vortex-vortex and vortex-tail interactions near tail trailing edge.

Figure 24. Continued.

Light-sheet location

(g) Wing and LEX vortex flows upstream of tails at $\beta = 5°$.

Figure 24. Continued.

Light-sheet location
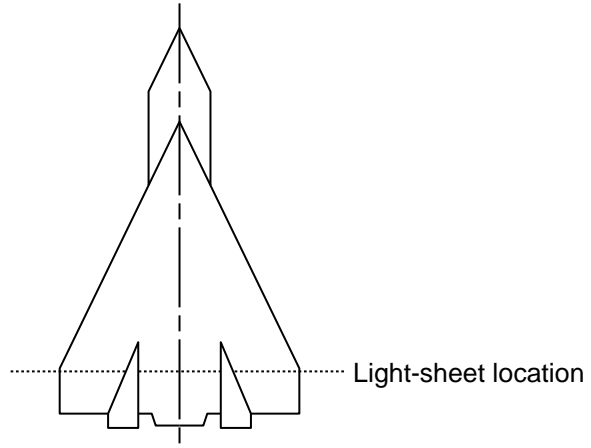
(h) Wing and LEX vortex flows at tails and $\beta = 5°$.

Figure 24. Continued.

δ_v, deg	α, deg
Off	25.27
30	25.13
0	25.16
-30	25.17
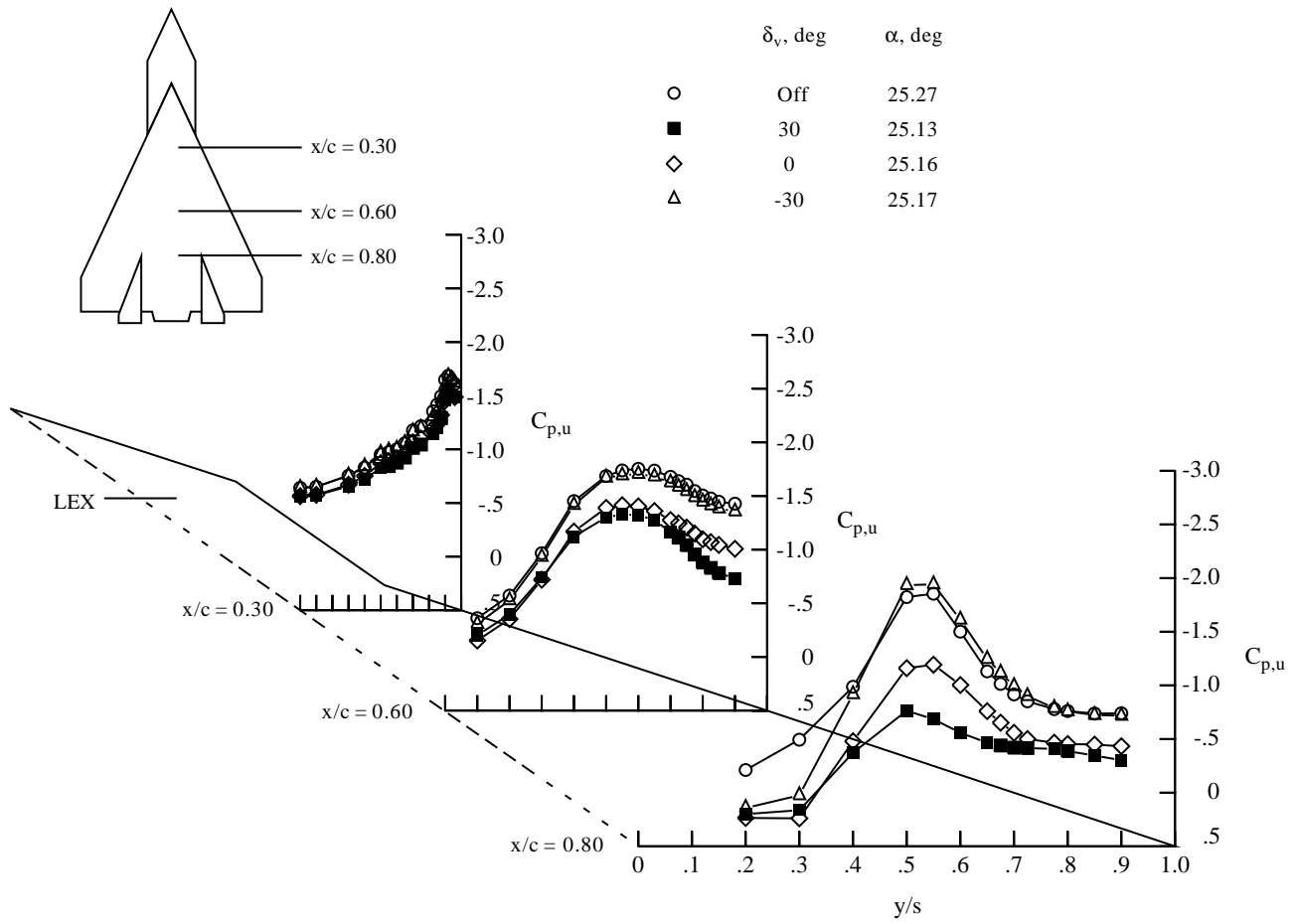
(i) Right-wing upper-surface static pressure distributions at $M_\infty = 0.50$.

Figure 24. Continued.

δ_v, deg

○   Off

■   30

◇   0

△   -30
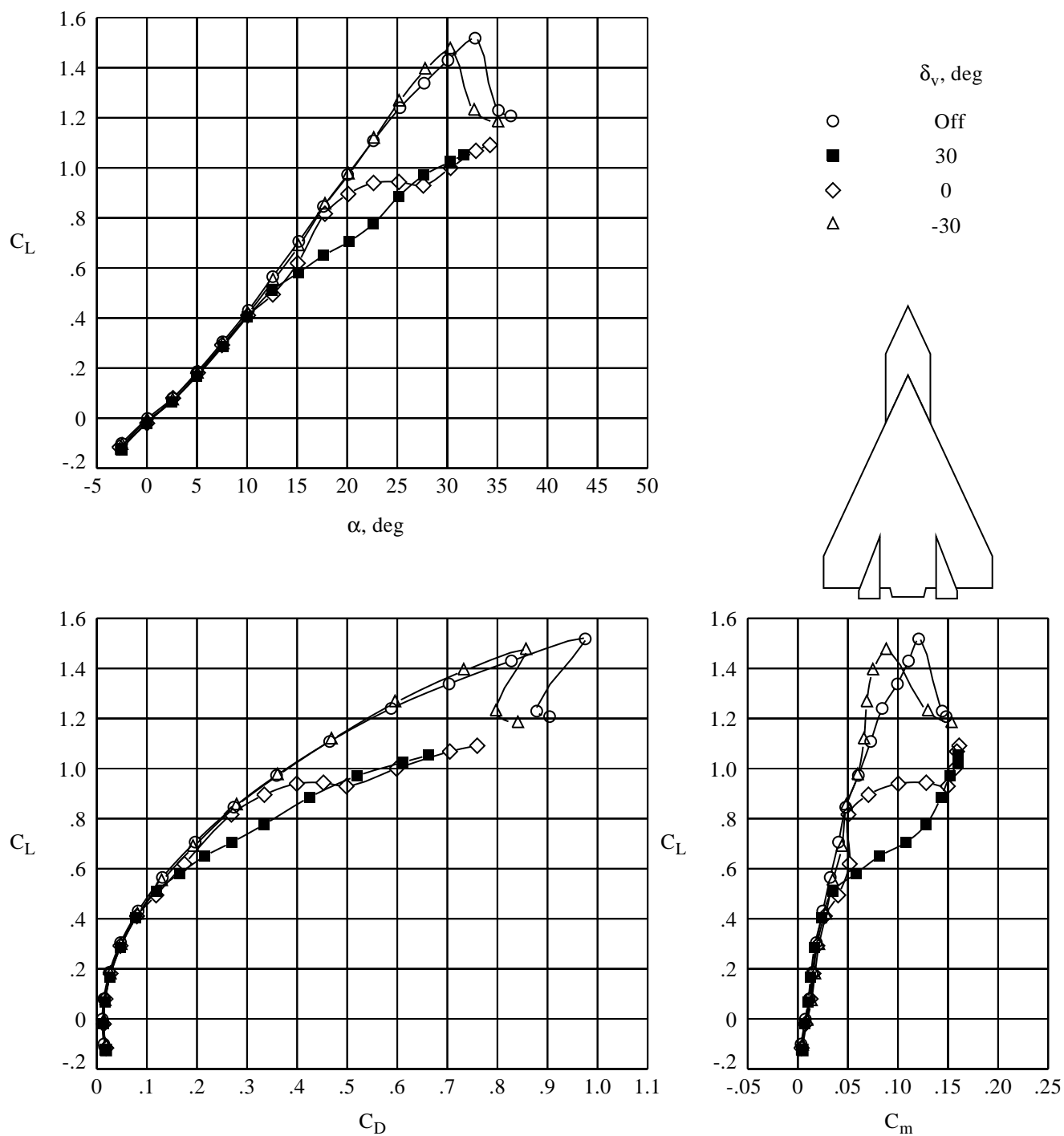
(j) Longitudinal characteristics at $M_\infty = 0.50$.

Figure 24. Continued.
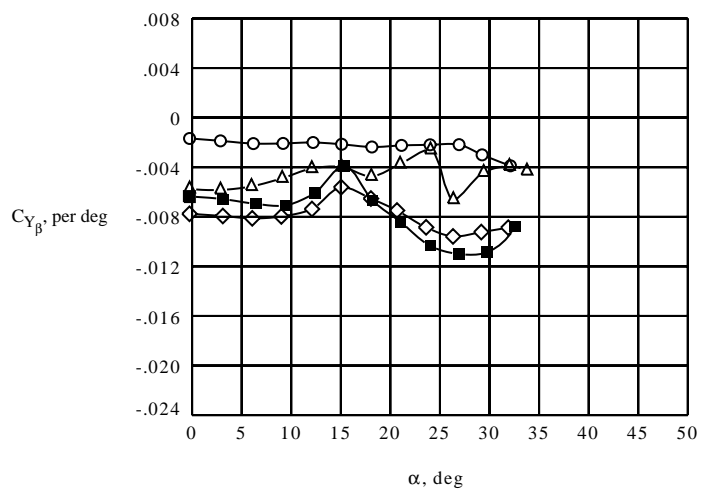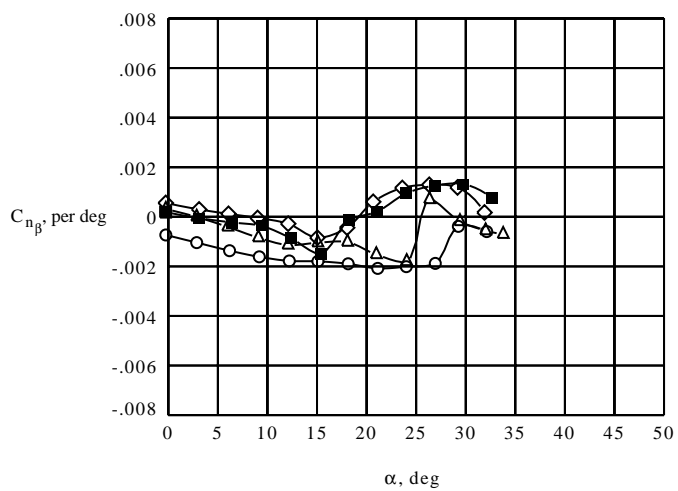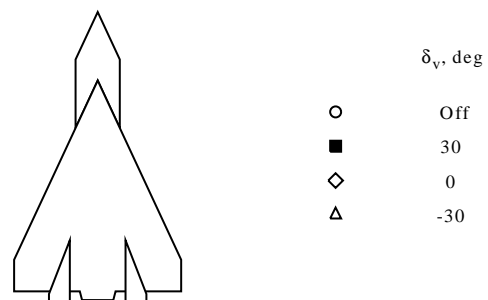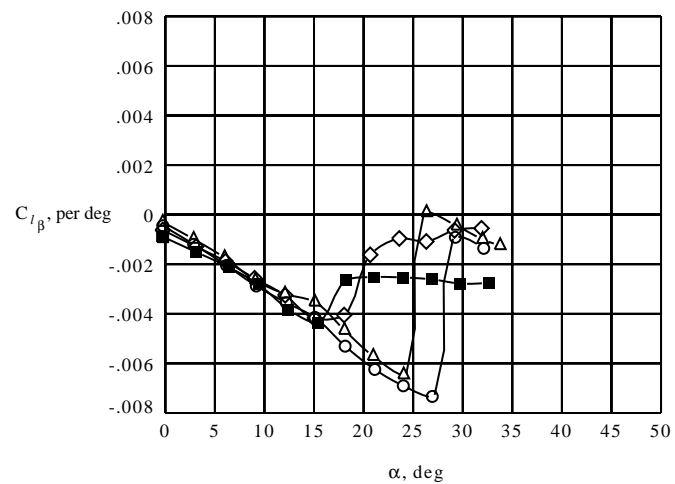
(k) Lateral-directional stability derivatives at $M_\infty = 0.50$.

Figure 24. Concluded.
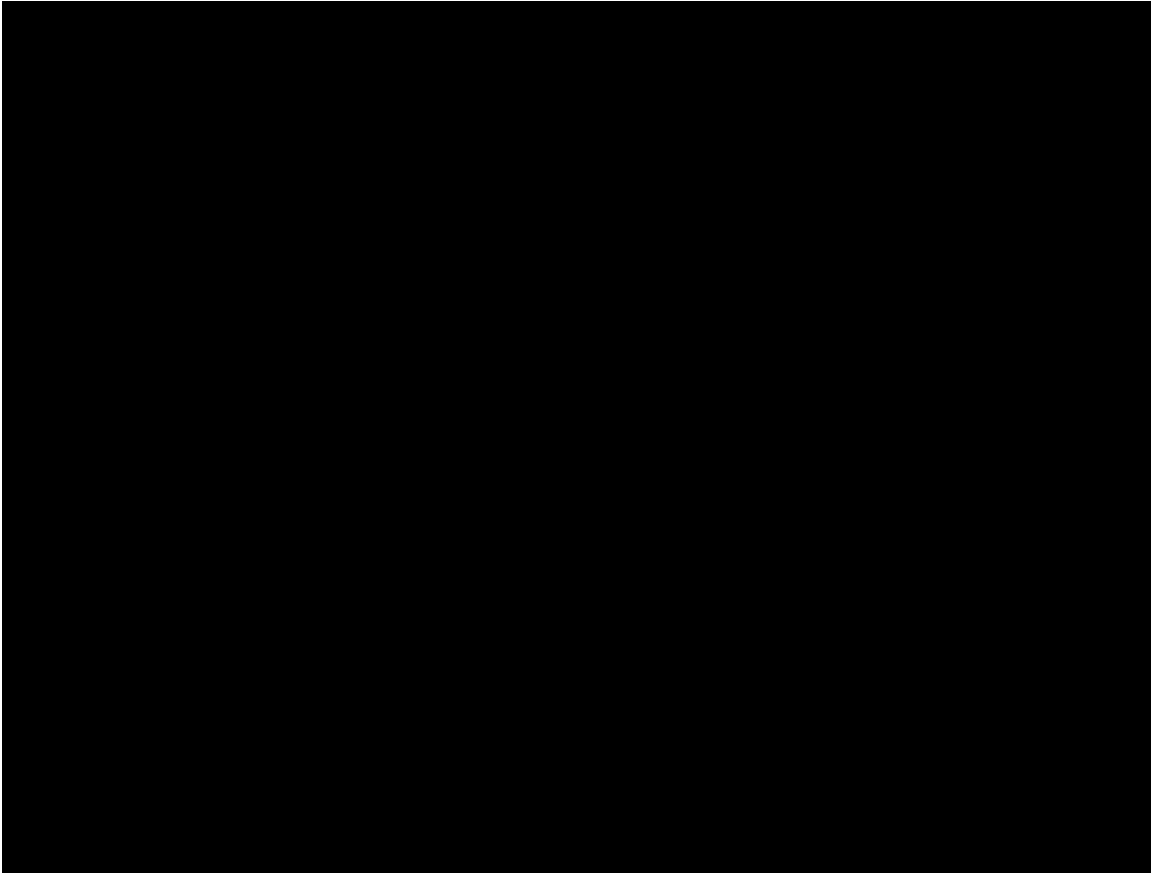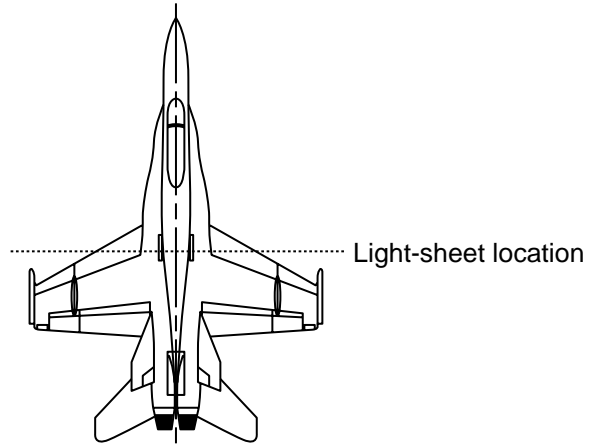
(a) LEX vortex flows.

Figure 25. LVS results on 0.06-scale F/A-18A model at $M_\infty = 0.45$ and $\alpha = 20°$ from Langley 7- by 10-Foot High-Speed Tunnel.

Light-sheet location
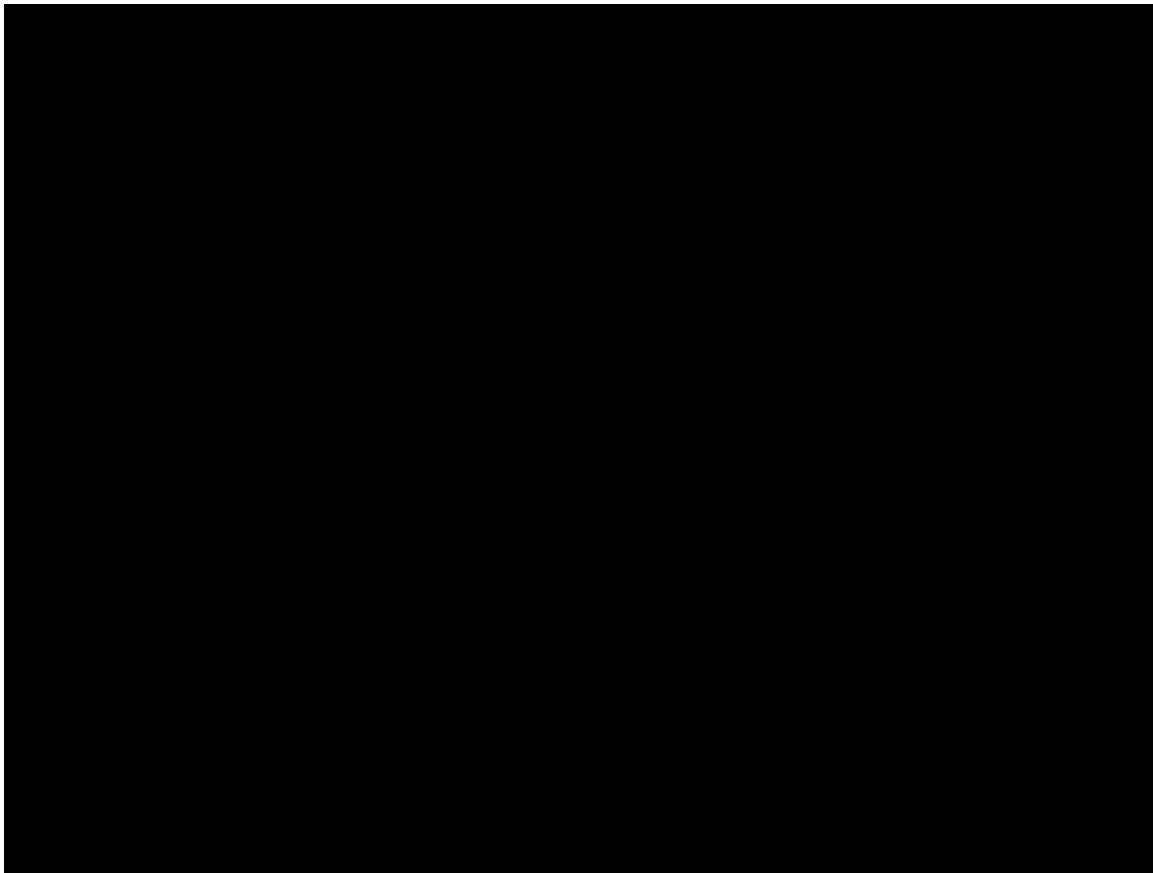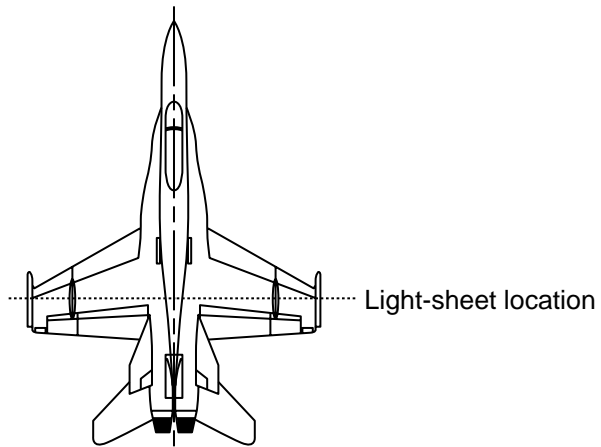
(b) LEX vortex-tail interaction.

Figure 25. Concluded.

Light-sheet location
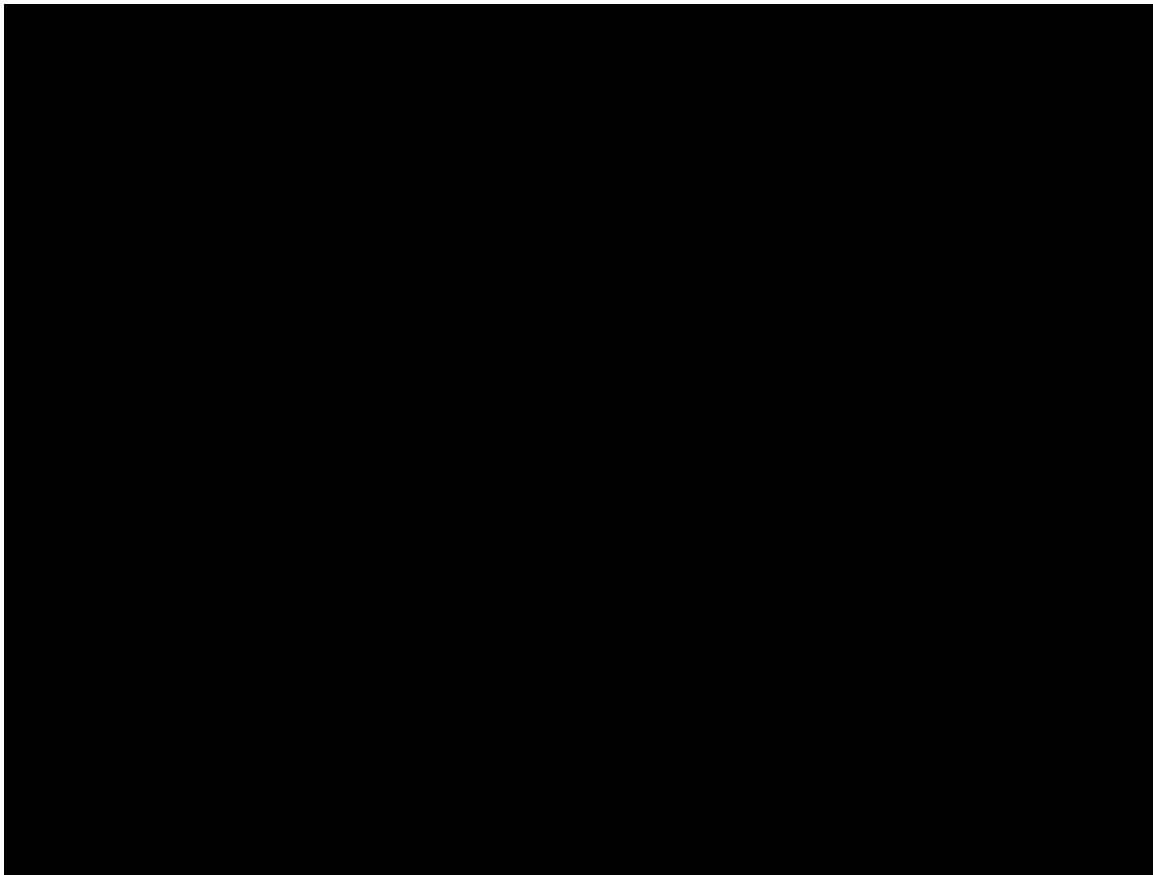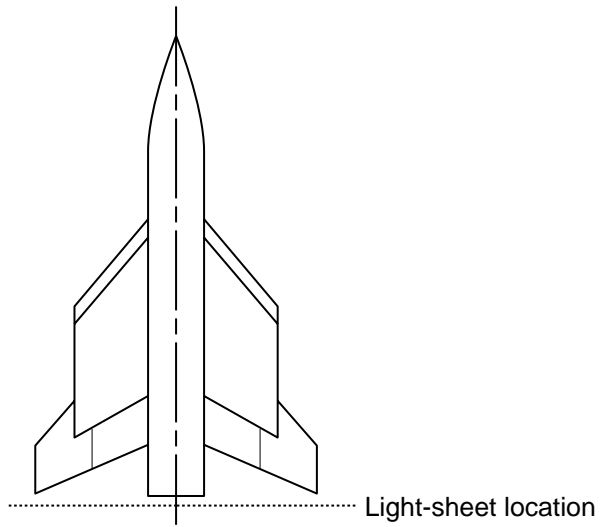
(a) $M_\infty = 0.50$; $\alpha = 20°$ (Langley 7- by 10-Foot High-Speed Tunnel).

Figure 26. LVS results on outboard control surface (OCS) model.
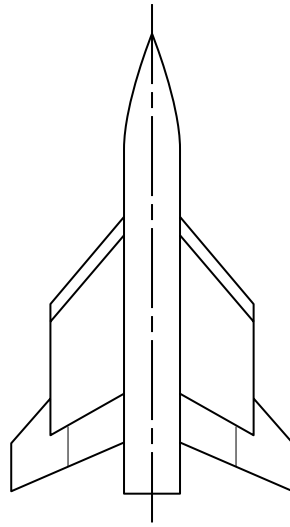
Light-sheet location
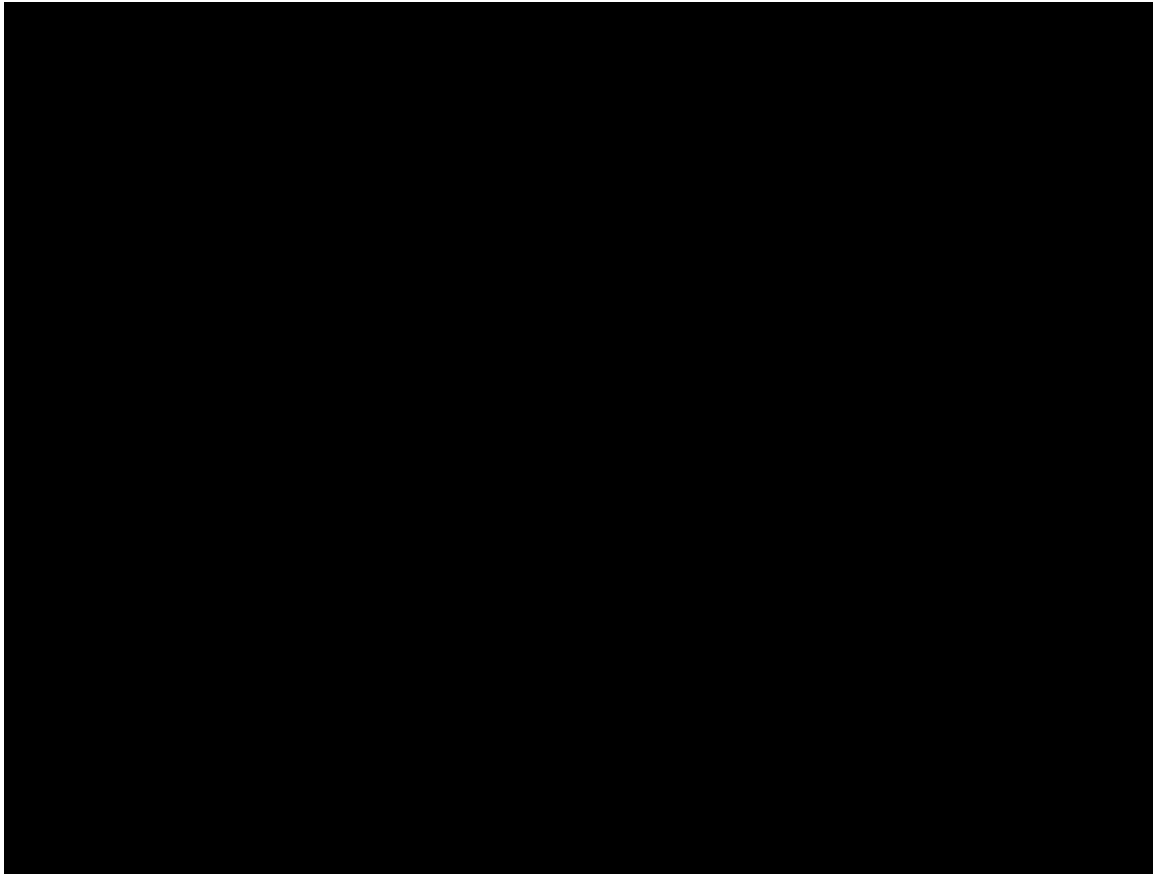
(b) $M_\infty = 1.20$; $\alpha = 20°$ (Langley 8-Foot High-Speed Tunnel).

Figure 26. Concluded.

Light-sheet location
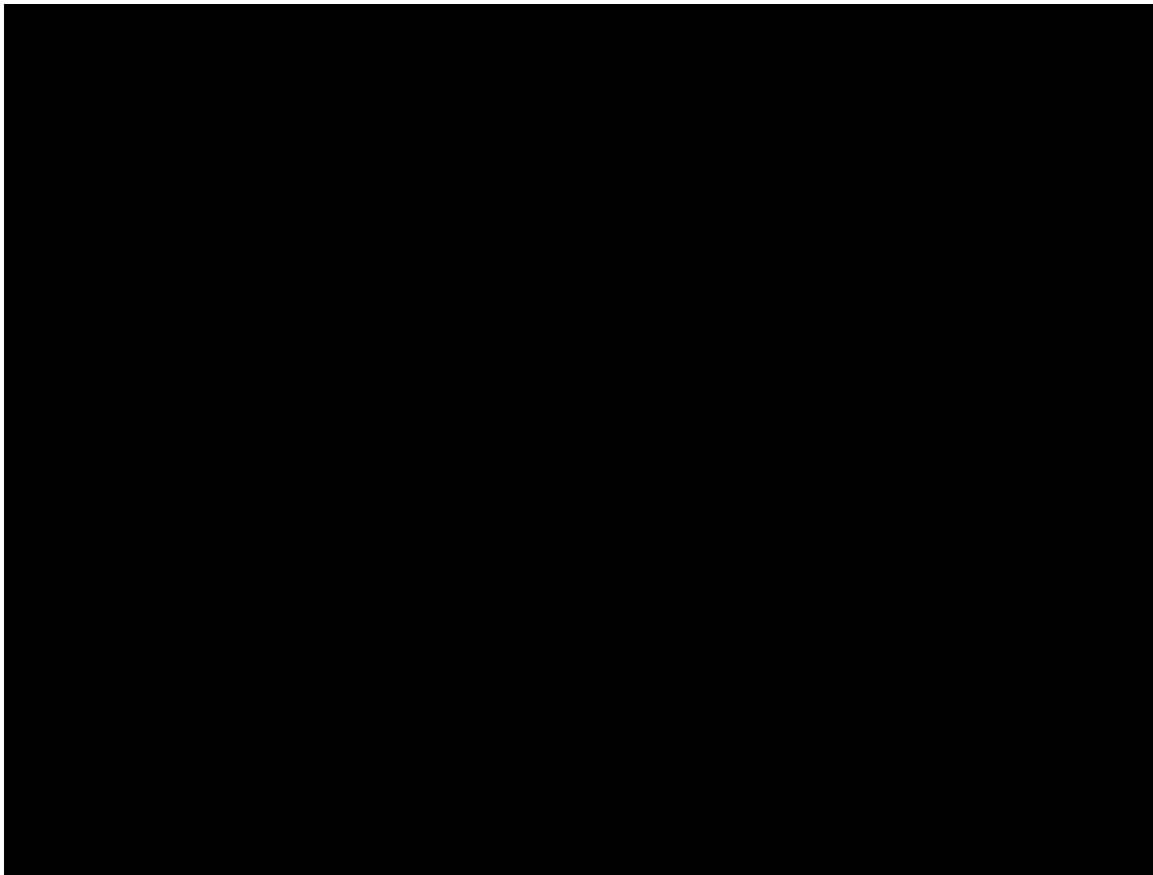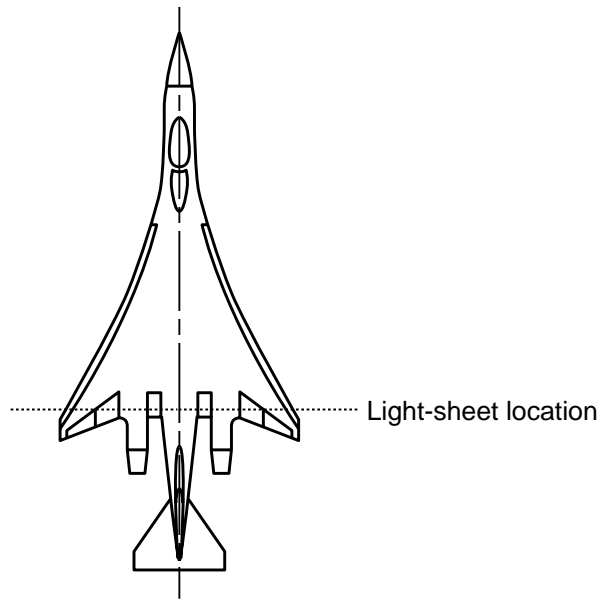
(a) Wing vortices; $M_\infty = 0.85$; $\alpha = 18°$.

Figure 27. LVS results on generic supersonic fighter/interceptor model from Langley 8-Foot Transonic Pressure Tunnel.
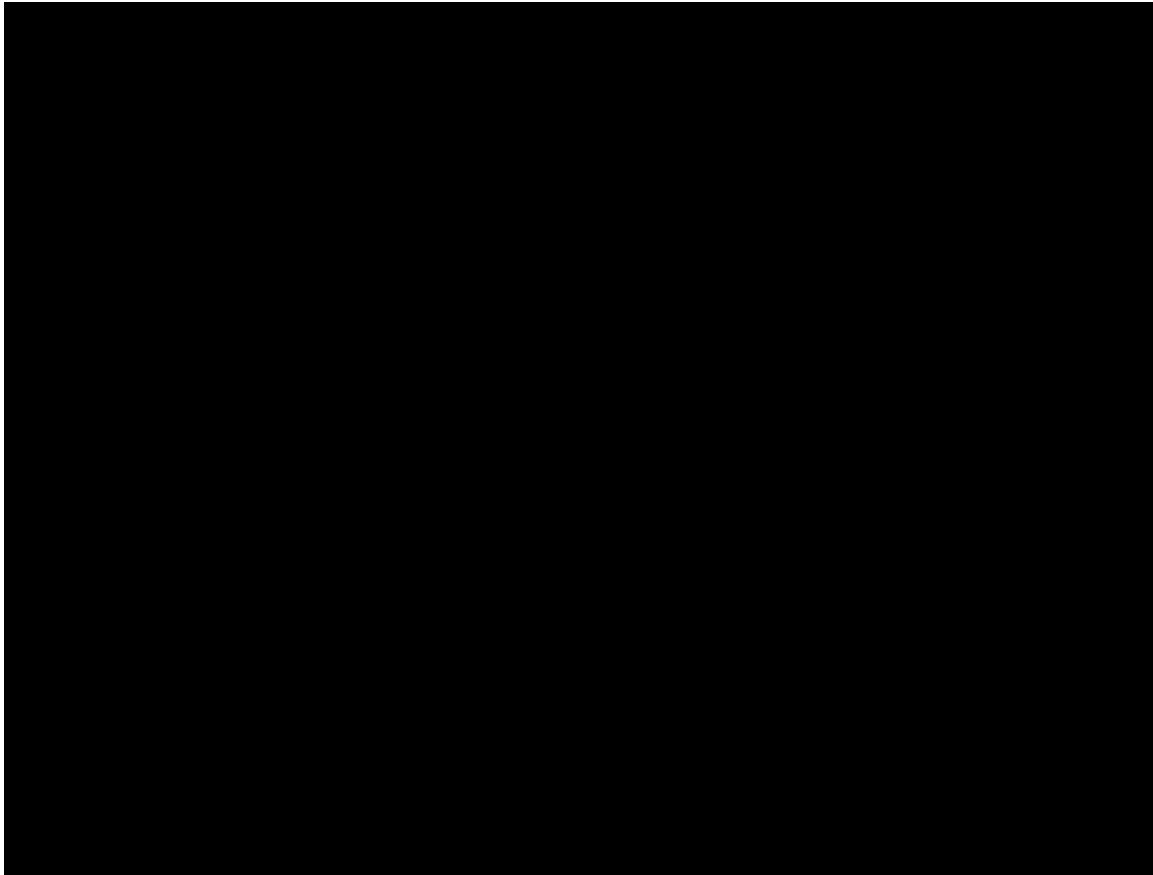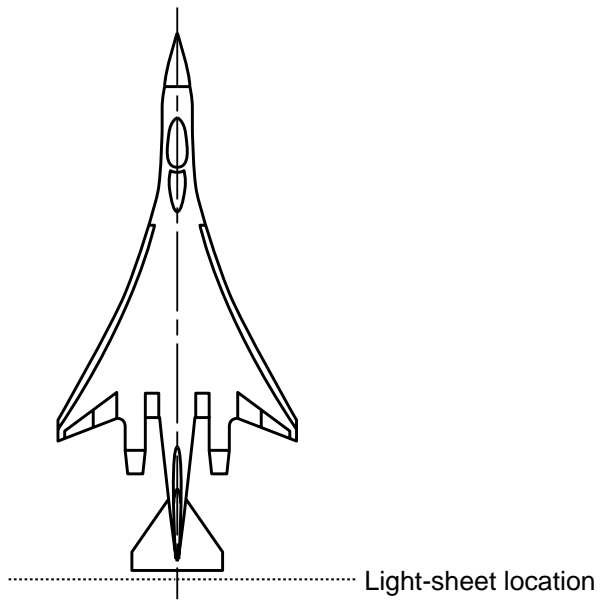
(b) Cross-flow pattern in near wake of model; $M_\infty = 1.19$; $\alpha = 9°$.

Figure 27. Continued.
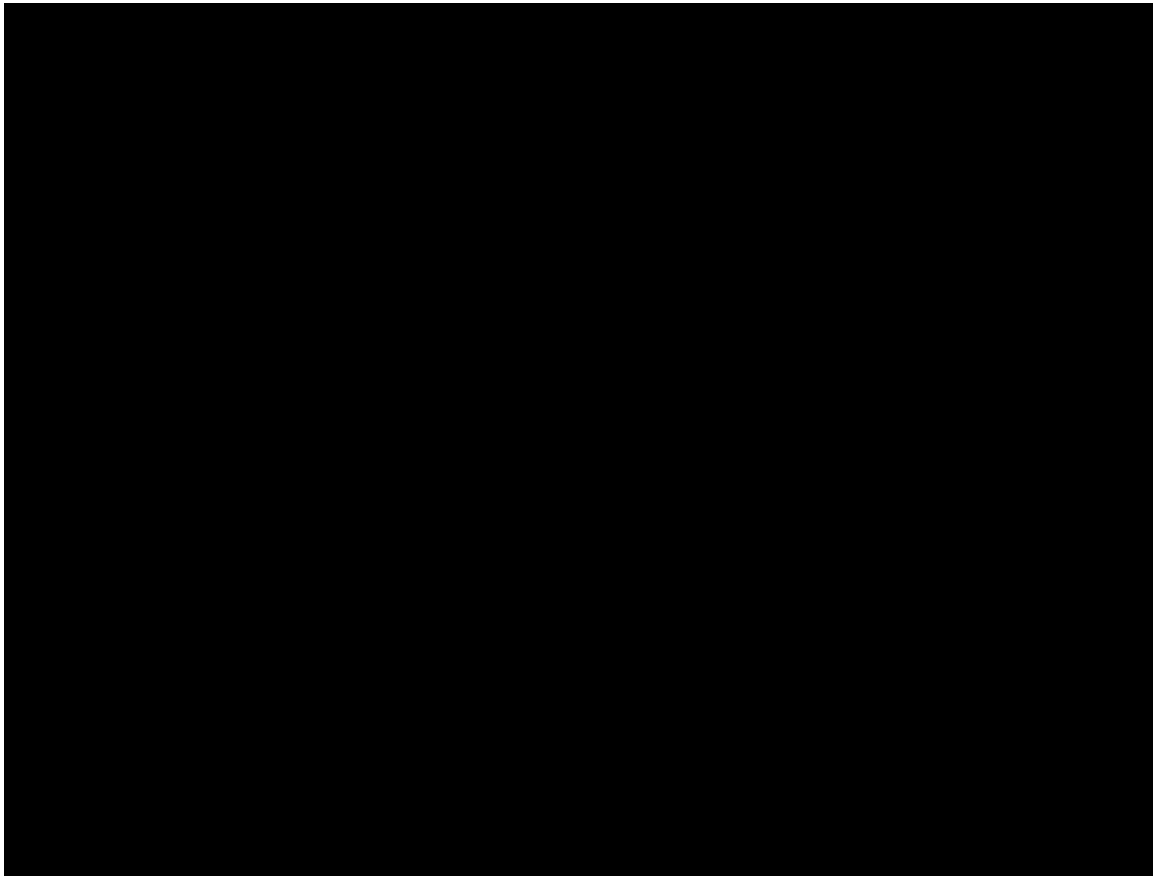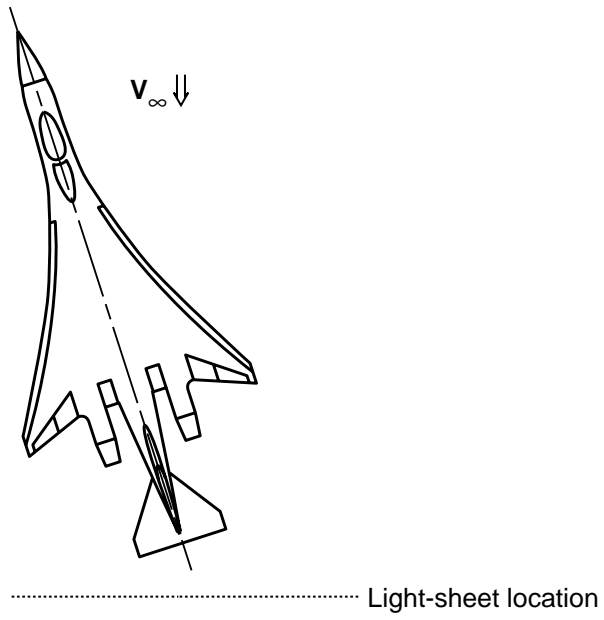
(c) Cross-flow pattern in near wake of model; $M_\infty = 1.19$; $\alpha = 18°$; $\beta = 8°$.

Figure 27. Continued.

$\mathbf{V}_\infty \Downarrow$

·· Light-sheet location
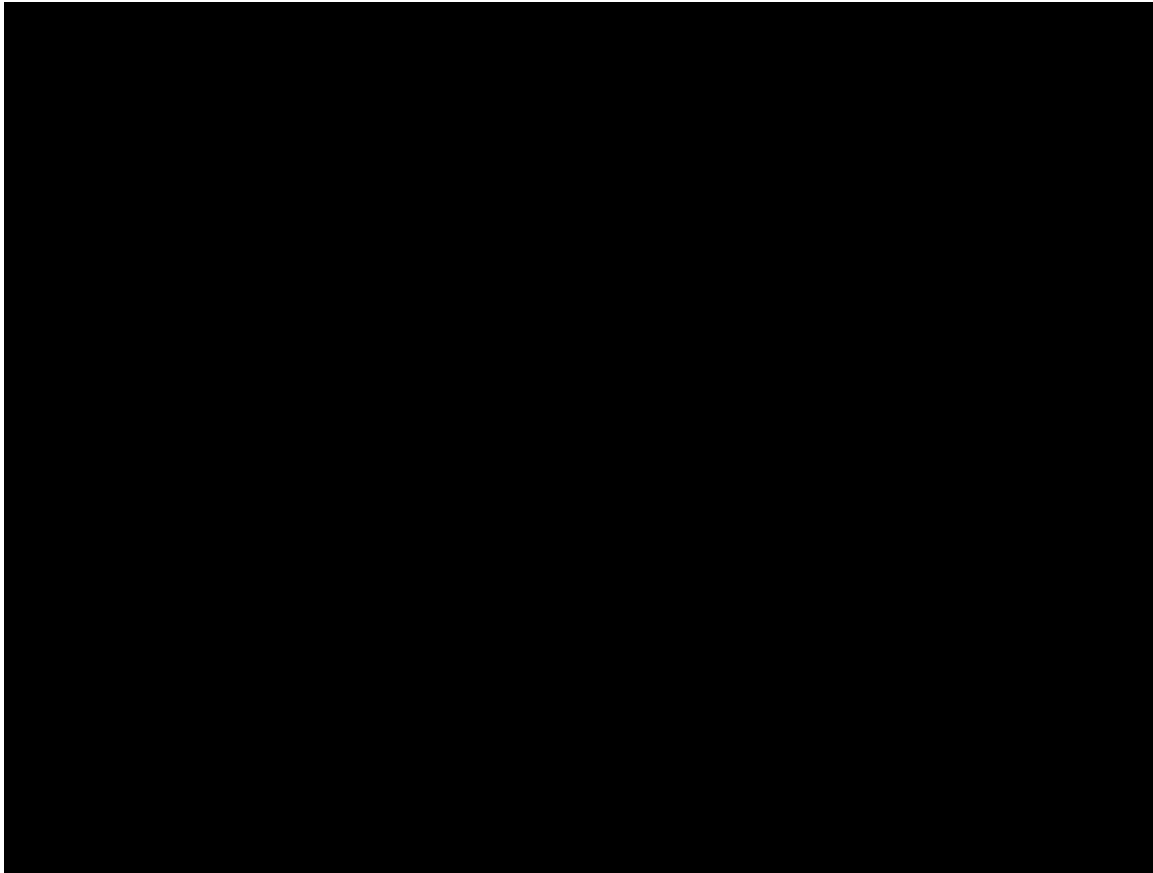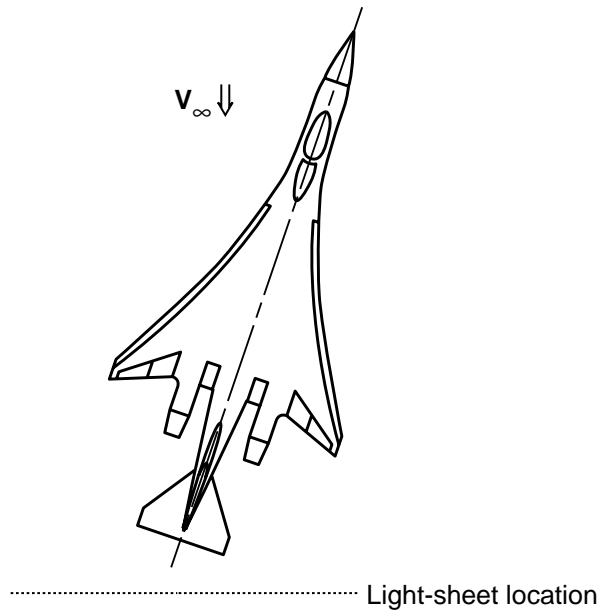
(d) Cross-flow pattern in near wake of model; $M_\infty = 1.19$; $\alpha = 18°$; $\beta = -8°$.

Figure 27. Concluded.

Light-sheet location
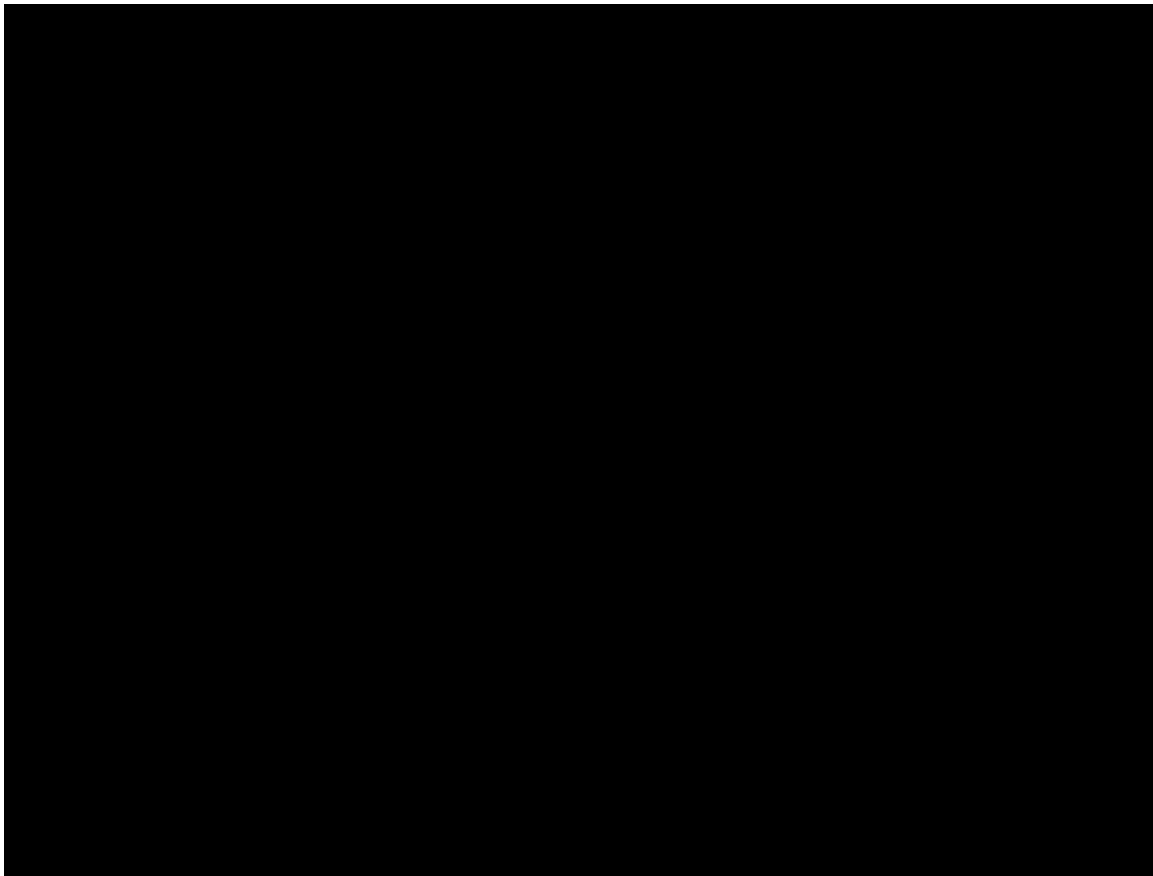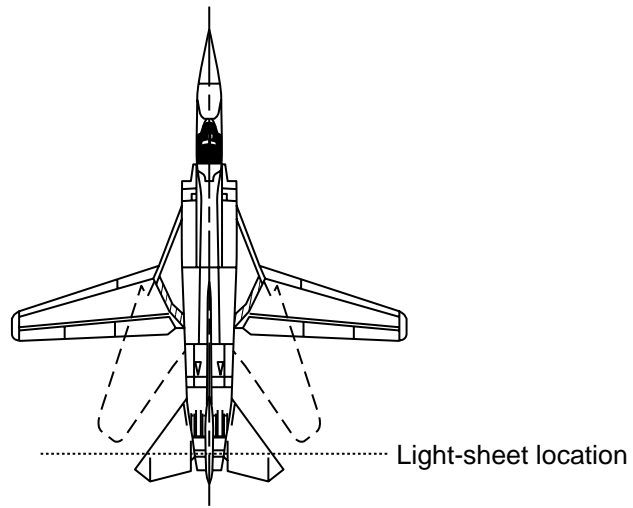
(a) Multiple vortices from wing; $M_\infty = 0.85$; $\alpha = 18°$; $\beta = 0°$.

Figure 28. LVS results on variable-sweep fighter/bomber model from Langley 8-Foot Transonic Pressure Tunnel.

V$_\infty$ ⇓

Light-sheet location
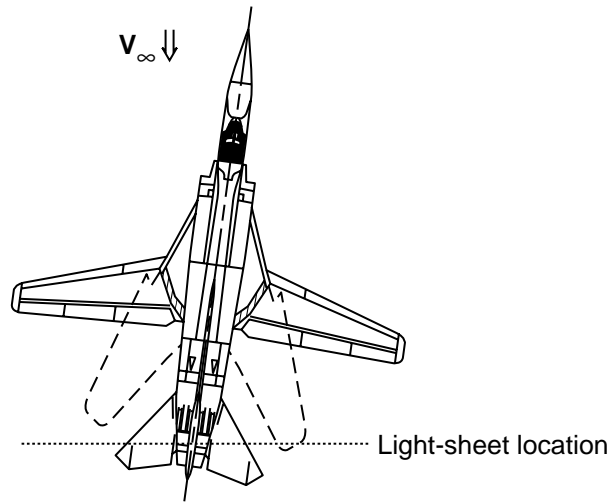
(b) Wing vortex flows in sideslip; $M_\infty = 0.85$; $\alpha = 18°$; $\beta = -4°$.

Figure 28. Continued.

Light-sheet location
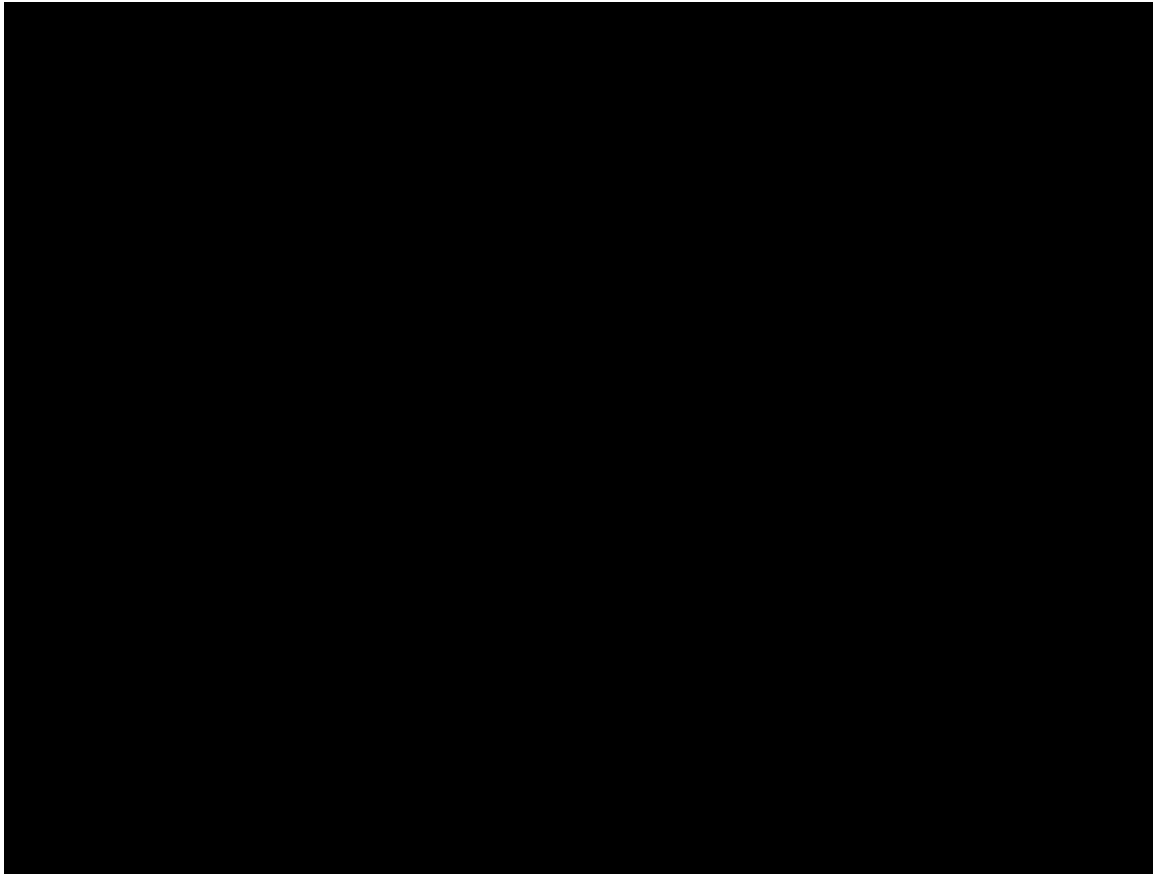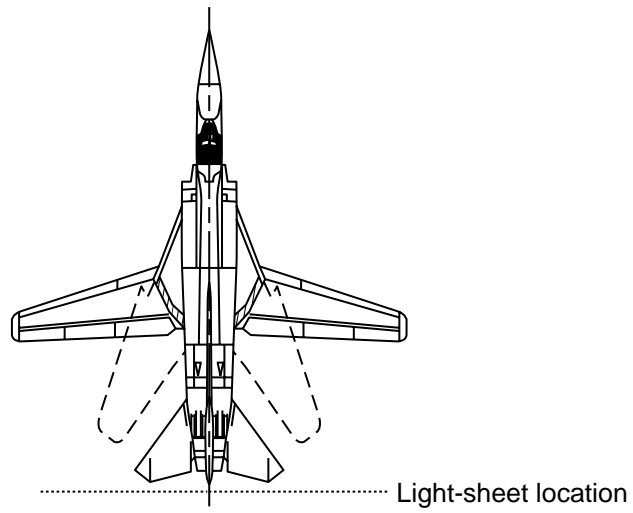
(c) Cross-flow pattern in near wake; $M_\infty = 1.20$; $\alpha = 22°$; $\beta = 0°$.

Figure 28. Continued.
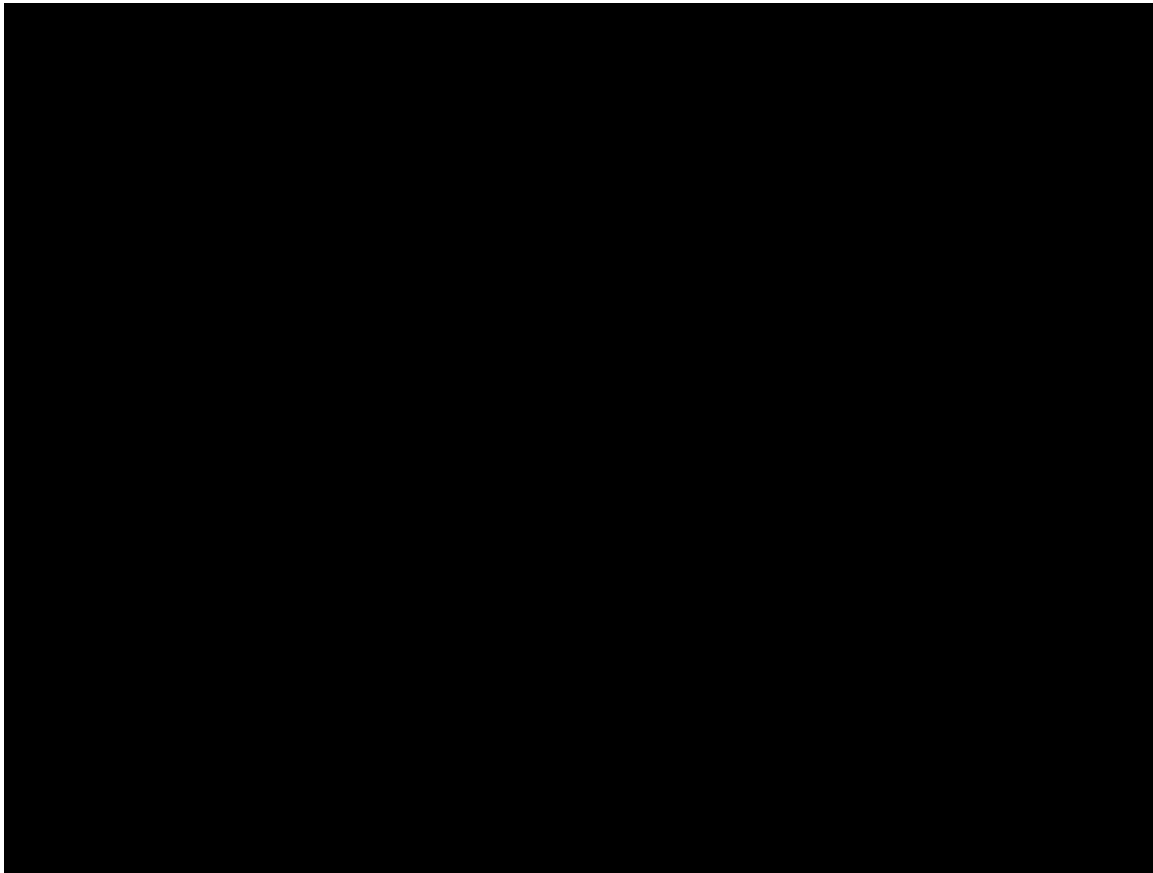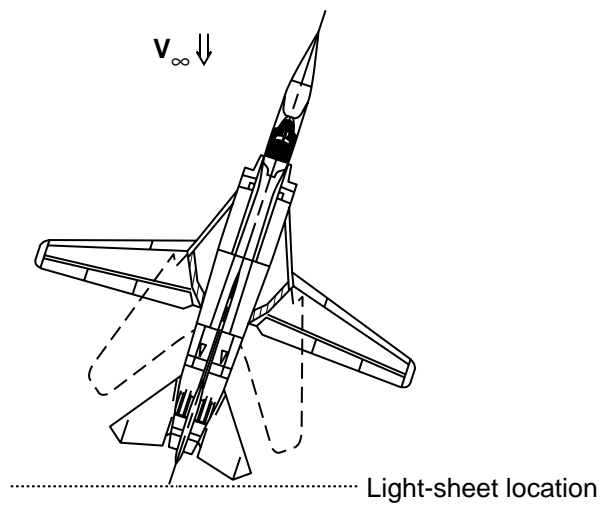
(d) Cross-flow pattern in near wake; $M_\infty = 1.20$; $\alpha = 22°$; $\beta = -8°$.

Figure 28. Concluded.

Light-sheet location
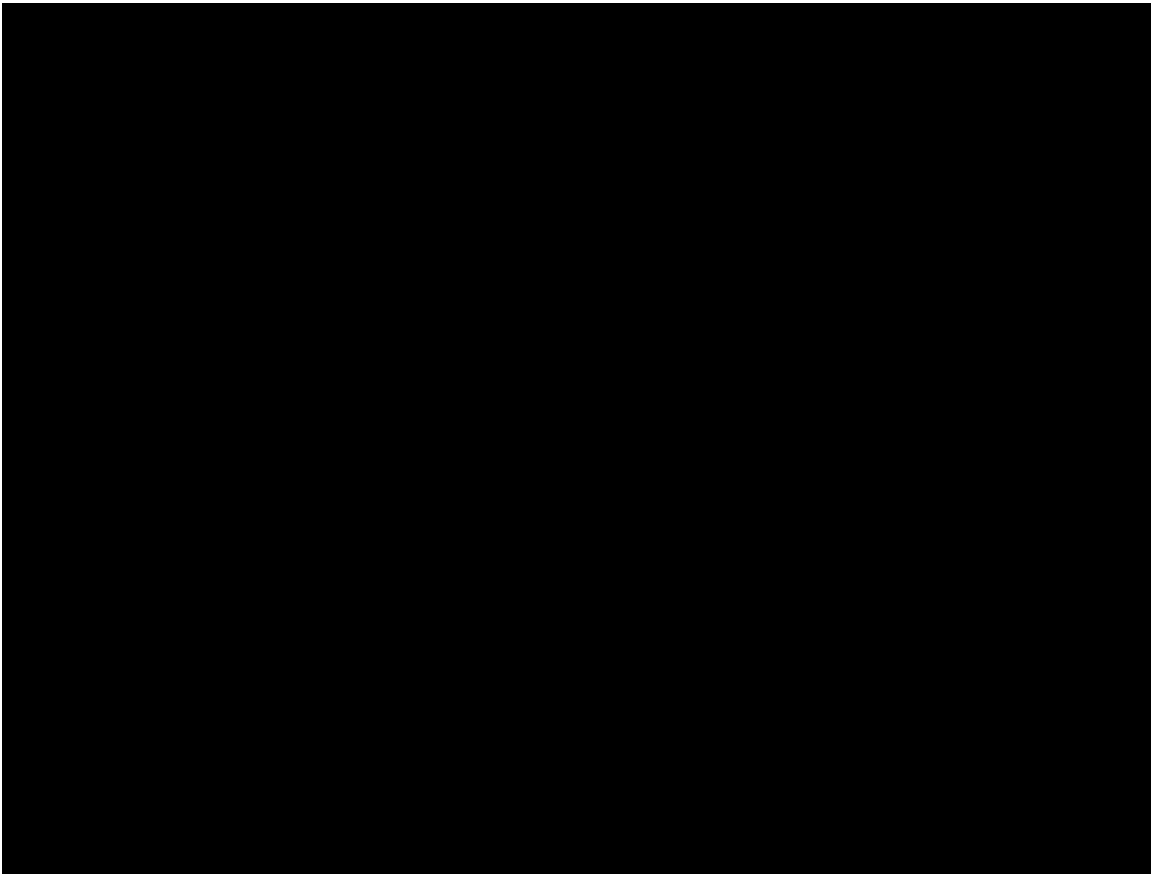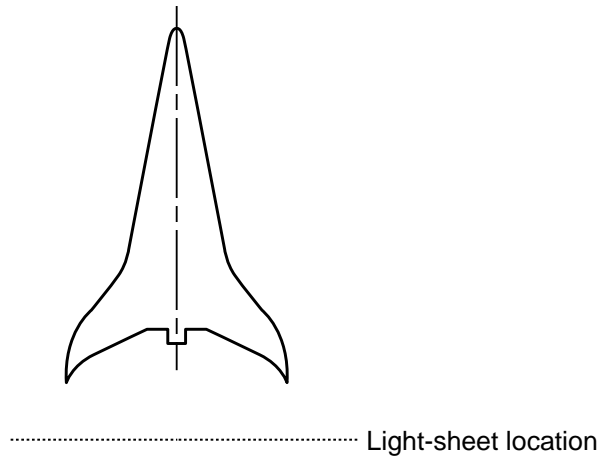
(a) Wing vortex cross flow in near wake of model.

Figure 29. LVS results on generic high-speed civil transport model at $M_\infty = 0.90$ and $\alpha = 9°$ from Langley 8-Foot Transonic Pressure Tunnel.
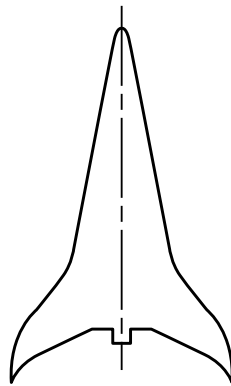
Light-sheet location
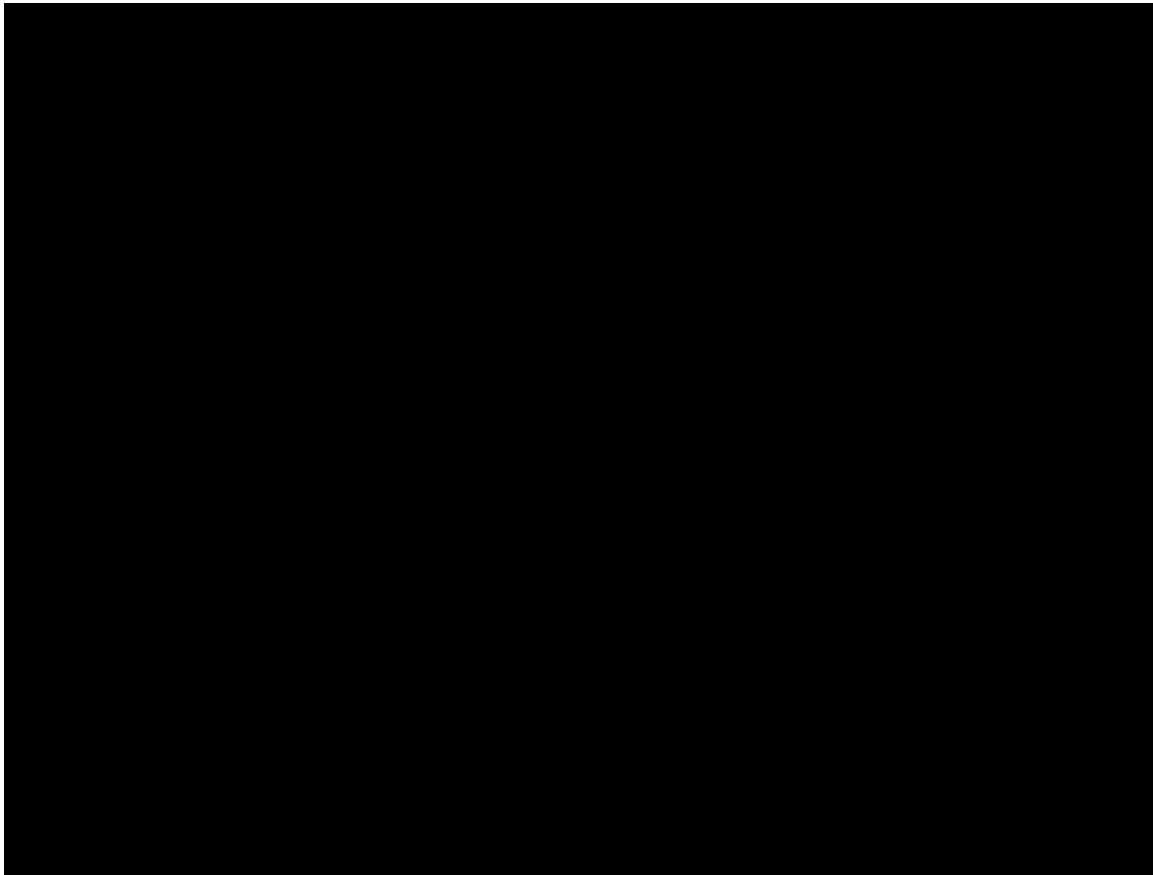
(b) Wing vortex cross flow in far wake of model.

Figure 29. Concluded.

Figure 8. Sketch of Langley 8-Foot Transonic Pressure Tunnel.

L-89-1339

(a) Laser-to-fiber coupler.

(b) Armored fiber optic cable.

Figure 13. Photographs of fiber-optic-based beam delivery system.

L-90-04449

L-90-04363

(c) Remote line projector unit with scanning mirror.

L-90-04355

(d) Motor controller.

Figure 13. Concluded.

L-90-04356

L-91-01725

(a) Argon-ion laser head.

(b) Argon-ion laser power supply.

Figure 11. Photographs of principal laser system components.

L-90-04450

L-90-04468

(c) Remote control module.

Figure 11. Continued.

L-90-04452

(d) Heat exchanger.

Figure 11. Continued.

L-90-04444

(e) City water supply system.

Figure 11. Concluded.

L-71-3976

Figure 6. Langley 8-Foot Transonic Pressure Tunnel.

L-85-13335

Figure 7. Langley 7- by 10-Foot High-Speed Tunnel.

L-90-4370

Figure 20. Photograph of miniature color video camera.

L-90-04459

Figure 21. Photograph of color video camera on tilt/pan table.

L-90-04463

Figure 16. Photograph of laser power meter and detector head.

L-90-01715

L-91-01717

(a) Fiber optic cable penetration into plenum.

(b) Fiber optic cable routing to light-sheet optics.

Figure 12. Photographs of fiber optic cable routing in Langley 8-Foot Transonic Pressure Tunnel.

Abstract

Laser vapor screen (LVS) flow visualization systems that are fiber-optic based have been developed and installed for aerodynamic research in the Langley 8-Foot Transonic Pressure Tunnel and the Langley 7- by 10-Foot High-Speed Tunnel. Fiber optics are used to deliver the laser beam through the plenum shell that surrounds the test section of each facility and to the light-sheet-generating optics positioned in the ceiling window of the test section. Water is injected into the wind tunnel diffuser section to increase the relative humidity and promote condensation of the water vapor in the flow field about the model. The condensed water vapor is then illuminated with an intense sheet of laser light to reveal features of the flow field. The plenum shells are optically sealed; therefore, video-based systems are used to observe and document the flow field. Operational experience shows that the fiber-optic-based systems provide safe, reliable, and high-quality off-surface flow visualization in smaller and larger scale subsonic and transonic wind tunnels. The design, the installation, and the application of the Langley Research Center (LaRC) LVS flow visualization systems in larger scale wind tunnels are highlighted in the present paper. The efficiency of the fiber optic LVS systems and their insensitivity to wind tunnel vibration, the tunnel operating temperature and pressure variations, and the airborne contaminants are discussed.

Introduction

The laser vapor screen (LVS) method of flow visualization was first employed in 1951 in the National Advisory Committee for Aeronautics (NACA) 1- by 3-Foot Supersonic Wind Tunnels at the Ames Aeronautical Laboratory to study the vortical flows about slender inclined bodies of revolution at high angles of attack (ref. 1). In this experiment, a small amount of water was injected downstream of the nozzle, and vaporization was nearly instantaneous. The temperature drop from the expansion in the supersonic nozzle caused the water vapor to condense into a fine fog. A light sheet (or screen) produced by a high-pressure mercury-vapor lamp was projected through a glass window in the side of the test section in a plane perpendicular to the axis of the tunnel. This light sheet was used to illuminate the fog as it was entrained in the flow field over the model. A representative installation of the vapor screen flow visualization is sketched in figure 1. The distribution of condensed water vapor and, consequently, the amount of scattered light within the plane of the light sheet were affected by the flow disturbances created by the model at a high angle of attack. This phenomenon permitted the observation and the documentation of body vortex cross sections, which appeared as black dots within a light background in the vapor screen image; these dots were caused by the absence of scattered light.

Similar experimental techniques and apparatus were used in reference 2 to visualize vortices, vortex sheets, lines of flow separation and reattachment, and shock waves at higher subsonic, transonic, and supersonic speeds. These tests were conducted, beginning in the late 1950's, in the 3-Foot Supersonic Wind Tunnel of the Royal Aeronautical Establishment (RAE). The studies suggested that the lowest free-stream Mach number at which the vapor screen technique was practicable was approximately 0.85. At lower Mach numbers, continuous injection of water was required to maintain a satisfactory visualization level, and dense white patches caused by local condensation about the model obscured the images when viewed from a downstream location.

Flow visualization using the vapor screen method was extended to lower subsonic Mach numbers ($M_\infty = 0.60$) in experimental investigations of symmetric forebodies initiated in the 1970's in the 6- by 6-Foot Supersonic Wind Tunnel (ref. 3) at the Ames Research Center. At subsonic Mach numbers, the body vortices appeared as white spots surrounded by a dark background; these white spots resulted from the water vapor condensing first near the vortex cores. Improved water injection control and more uniform free-stream temperature distribution compared with the experiments in reference 2 enabled the observation and the documentation of the vortices at Mach numbers of less than 0.85.

Lasers superseded the mercury-vapor lamps as the primary light-sheet source beginning in the late 1970's. Lasers provided a thinner, more intense sheet of light which enhanced the details of the vapor screen images. The flow visualization method was accordingly referred to as LVS. The LVS method is designed for use at high subsonic through supersonic speeds, and it is distinguished from low-speed laser light-sheet techniques that use different seeding particles to visualize the cross-flow patterns. References 4 through 6 are representative of the high-quality results obtained in low-speed wind tunnels ($M_\infty < 0.3$) using smoke or propylene glycol as the light-scattering medium.

The use of the LVS method as a standard tool to visualize the vortex-dominated flow fields about subscale models of fighter aircraft configurations at subsonic through supersonic speeds evolved from several experimental investigations conducted by NASA in cooperation with the United States Air Force and Navy beginning in the mid-1980's. The initial testing was conducted in the 6- by 6-Foot Supersonic Wind Tunnel at the Ames Research Center and the 7- by 10-Foot Transonic Tunnel (7- by 10-Foot TT) at the David Taylor Research Center (DTRC) using subscale models of generalized and specific fighter configurations. Representative results from these studies (refs. 7 through 9) are presented in figures 2 through 4. The LVS method was used successfully to establish a flow visualization data base on multiple-vortex development, vortex-tail and vortex-shock interactions, vortex breakdown, and vortex control concepts at free-stream Mach numbers from 0.30 to 1.80. Continuous injection of water was required at low Mach numbers to promote the desired condensation patterns, while intermittent injection of water in smaller amounts was sufficient at high Mach numbers. Consistent with earlier studies (refs. 1 through 3), researchers found that the vortices appeared as white regions surrounded by a dark background at the subsonic speeds and as dark regions in a white background at supersonic speeds. At transonic speeds, a combination of the two light-scattering patterns typically occurred.

The testing in NASA and Navy facilities revealed deficiencies in the LVS experimental setup employed in larger scale wind tunnels. A mirror-based system was used to direct, or steer, the laser beam to the light-sheet-generating optics located on the sidewall or the ceiling of the wind tunnel test section. The laser was located outside the pressure, or plenum, shell surrounding the test section of the DTRC facility because of laser operational considerations. As a result, the laser beam was directed over a large distance, and several mirrors were required to steer the beam to the light-sheet optics. Tunnel vibration at high speeds promoted a misalignment of the laser beam and optical components, while airborne contaminants (oil, for example) settling onto the mirror surfaces reduced the quality and the intensity of the light sheet at the model. These effects sometimes caused significant reductions in tunnel efficiency and productivity because access to the optics inside the plenum region was generally required to realign or clean the system. In most cases, 2 to 3 hours were required to vent the plenum region to atmospheric pressure, realign or clean the optics, and repressurize the plenum to the desired operating conditions. In addition, the exposed laser beam and the use of multiple mirrors posed a safety hazard, particularly during the alignment process, because the laser had to be aligned at high power.

Fiber optics (ref. 10) provided a solution to the inherent problems of mirror-based beam delivery systems. A fiber optic cable extending from the laser head to the light-sheet optics provided an effective beam delivery and containment system with enough power in the beam to produce a light sheet. A prototype system consisting of a 150-ft-long fiber optic cable and a continuous-wave (CW) argon-ion laser was installed and successfully applied by NASA in 1989 for use in a test of a 0.06-scale F/A-18 model with forebody yaw control strakes in the 7- by 10-Foot TT (ref. 11) at the DTRC. A nonpulsed laser is well suited for visualizing low-dynamic vortical flows, such as those generated by the F/A-18 configuration in steady-flow conditions. A pulsed laser is required to visualize high-dynamic flows as would be encountered, for example, about a helicopter rotor blade. Results from using this prototype system are shown in figure 5. The flow visualization results were obtained at $M_\infty = 0.80$ using a video camera that was mounted aft of the model on the sting support system and looking upstream along the model centerline. Figure 5(a) shows the interaction of the wing leading-edge extension (LEX) vortices with the twin vertical tails. The complex vortical flow features along the forward fuselage section with the left forebody yaw control strake installed are illustrated in figure 5(b). Permanent fiber-optic-based LVS flow visualization systems were developed after the DTRC testing and the systems were installed in 1990 in the Langley 8-Foot Transonic Pressure Tunnel (8-Foot TPT) and the Langley 7- by 10-Foot High-Speed Tunnel (7- by 10-Foot HST). Similar systems are now standard tools for aerodynamic research in several Langley Research Center (LaRC) wind tunnels. The present paper will describe the experimental

apparatus and its operation and show representative results from the 8-Foot TPT and 7- by 10-Foot HST facilities.

Symbols and Abbreviations

b	wing span, in.
C_D	drag coefficient, $\frac{\text{Drag}}{q_\infty S_{\text{ref}}}$
C_L	lift coefficient, $\frac{\text{Lift}}{q_\infty S_{\text{ref}}}$
C_l	body-axis rolling-moment coefficient, $\frac{\text{Rolling moment}}{q_\infty S_{\text{ref}} b}$
C_{l_β}	lateral stability derivative, $\frac{\partial C_l}{\partial \beta}$, calculated by $\frac{C_{l_{(\beta=+5^\circ)}} - C_{l_{(\beta=-5^\circ)}}}{10^\circ}$, per deg
C_m	pitching-moment coefficient referenced to $0.40\bar{c}$, $\frac{\text{Pitching moment}}{q_\infty S_{\text{ref}} \bar{c}}$
C_n	body-axis yawing-moment coefficient, $\frac{\text{Yawing moment}}{q_\infty S_{\text{ref}} b}$
C_{n_β}	directional stability derivative, $\frac{\partial C_n}{\partial \beta}$, calculated by $\frac{C_{n_{(\beta=+5^\circ)}} - C_{n_{(\beta=-5^\circ)}}}{10^\circ}$, per deg
$C_{p,u}$	wing upper-surface static pressure coefficient, $\frac{p - p_\infty}{q_\infty}$
C_Y	side-force coefficient, $\frac{\text{Side force}}{q_\infty S_{\text{ref}}}$
C_{Y_β}	side force caused by sideslip derivative, $\frac{\partial C_Y}{\partial \beta}$, calculated by $\frac{C_{Y_{(\beta=+5^\circ)}} - C_{Y_{(\beta=-5^\circ)}}}{10^\circ}$, per deg
c	wing centerline chord, in.
$\bar{c}$	wing mean aerodynamic chord, in.
M_∞	free-stream Mach number
p	local upper-surface static pressure, lb/in²
p_∞	free-stream static pressure, lb/in²
q_∞	free-stream dynamic pressure, lb/in²
S_{ref}	reference wing area, in²
s	wing local semispan distance from fuselage centerline to wing leading edge, in.
$\mathbf{V}_\infty$	free-stream velocity, ft/sec
x	distance along wing centerline chord measured from wing apex, in.
y	distance along wing local semispan measured from fuselage centerline, in.
α	angle of attack, deg
β	angle of sideslip, deg
δ_v	vertical tail cant angle, deg

Abbreviations:

CFD	computational fluid dynamics
CW	continuous wave
DTRC	David Taylor Research Center
HSCT	high-speed civil transport
HST	High-Speed Tunnel
LaRC	Langley Research Center
LEX	wing leading-edge extension
LVS	laser vapor screen
NACA	National Advisory Committee for Aeronautics
NASA	National Aeronautics and Space Administration
NIRC	Nonionizing Radiation Committee
OCS	outboard control surface
RAE	Royal Aeronautical Establishment
SMA	small/miniature/type A connector
TE	trailing edge
TPT	Transonic Pressure Tunnel
TT	Transonic Tunnel

Wind Tunnel Facilities

The two LaRC facilities discussed are the Langley 8-Foot Transonic Pressure Tunnel (8-Foot TPT) and the Langley 7- by 10-Foot High-Speed Tunnel (7- by 10-Foot HST). The 8-Foot TPT is a continuous-flow, closed-return, slotted-throat pressure tunnel (fig. 6) that is capable of operating at pressures between 0.25 and 2.0 atm over a Mach number range from 0.2 to 1.2. The 7- by 10-Foot HST is a continuous-flow, solid-wall, subsonic-transonic atmospheric wind tunnel (fig. 7). The Mach number range is from $M_\infty \approx 0.06$ to $M_\infty \approx 0.94$. The tunnel operates at ambient temperature and pressure and continuously exchanges air with the surrounding atmosphere. Detailed descriptions of the 8-Foot

TPT and the 7- by 10-Foot HST are provided in references 12 and 13, respectively.

These facilities are used primarily to conduct fundamental research related to the exploration of new aerodynamic concepts. The studies include concepts to improve the understanding and the control of flow phenomena associated with civil and military aircraft configurations and experiments to assist in the development and the validation of computational fluid dynamics (CFD) methods. These facilities are also used in cooperative programs with the United States Department of Defense and industry to develop and validate new aircraft designs as well as modifications to existing aircraft.

Laser Safety at LaRC

The LaRC safety policy is to (1) exercise centralized control over operations involving the use of hazardous radiation-producing equipment; (2) assure that exposure of personnel to nonionizing radiation from such equipment is kept to a safe level; and (3) assure that compliance with applicable Federal, state, and local regulations is maintained. Reference 14 describes the organization, the training, and the responsibilities for radiological health and safety activity at LaRC. This document also defines procedures and requirements for procurement, use, and handling of sources of nonionizing radiation. The procedures and the practices are intended primarily for the use of lasers and laser sources, although they are applicable to other hazardous noncoherent sources of nonionizing radiation, such as radar, solar simulators, and high-intensity arc lamps.

Personnel at LaRC established a Nonionizing Radiation Committee (NIRC) to review and approve all procurement, handling, and use of lasers and laser sources. The NIRC is also required to audit and inspect the possession and the use of lasers of each facility on an annual basis.

The responsibility for implementing the LaRC policies is divided among five safety and health functions. These functions include the organizational facility safety head for each facility, the radiation safety officer, the safety manager for LaRC, the occupational health officer, and the radiation workers. Procurement of any hazardous source of nonionizing radiation must be approved by the organizational facility safety head, the radiation safety officer, and the safety manager. In addition, safety permits are required for all class 4 lasers and for class 3b lasers where a significant possibility exists that its users and operators will be exposed to radiation levels in excess of the applicable maximum permissible exposure (ref. 14). Class 4 lasers are high-power systems

that not only produce a hazardous direct or specularly reflected beam but also a hazardous diffuse reflection and a significant skin hazard. Continuous-wave class 4 lasers are categorized as those that have wavelengths of 200 to 400 nm (the ultraviolet range), 1400 nm to 1 mm and 400 nm to 700 nm (the visible range), and 700 nm to 1400 nm (the near-infrared range) and that emit an average accessible radiant power of 0.5 W or greater for periods greater than 0.25 sec. Class 3b consists of lasers that can produce accidental injury if viewed directly. Intrabeam viewing of either a direct or a mirror-like (specular) reflection of the beam is also considered hazardous. For CW class 3b lasers, the average radiant power does not exceed 0.5 W for exposure time greater than 0.25 sec. The safety permit request is submitted by the organizational facility safety head, and the request is reviewed and approved by the radiation safety officer, the NIRC, and the safety manager. Personnel appointed to each facility laser system and identified in the safety permit must be educated, trained, and certified as radiation workers. Personnel must also be given an initial complete eye examination and subsequent annual laser eye examinations. Medical records are specifically identified for certified nonionizing radiation workers.

The high-power class 4 lasers require the most rigid control measures because of the greater likelihood of injury caused by specular and diffuse reflections. The entire beam path that is capable of producing hazardous diffuse reflections must be controlled. These controls rely primarily on positive methods, such as enclosures and interlocks, and secondarily on procedural safeguards. Class 4 lasers require isolation in an area designated for laser operations, and access to such an area requires appropriate authorization.

The electrical installation and connection to the power supply circuit must meet the American National Standards Institute National Electrical Codes (ref. 14). Class 3b and class 4 lasers and laser systems must also have appropriate warning labels and laser control area posting.

The fiber-optic-based LVS systems discussed in this report represent a significant improvement in laser system safety because the beam is always contained within the fiber cable or within the optically sealed plenum shell surrounding the wind tunnel test section. The simplicity and the reliability of the LVS systems also facilitate the education and the training of personnel. Details of the fiber optic LVS systems are provided in the next section.

Technical Discussion

Fiber-Optic-Based LVS Systems

The discussion of the fiber-optic-based LVS systems will focus on the 8-Foot TPT installation. The system components and setup in the 8-Foot TPT closely resemble those in the 7- by 10-Foot HST. Figure 8 presents a schematic of the 8-Foot TPT, and figure 9 shows a sketch of the major fiber-optic-based LVS system components. The major components include laser light source, fiber optic beam delivery system, light-sheet optics, water injection system to increase the wind tunnel humidity, and video equipment for observation and documentation of the LVS images.

A 36-ft-diameter plenum shell encloses the test section of the 8-Foot TPT. Because of laser operational considerations, the laser head is located outside the plenum region in an optically sealed room abutting the plenum shell (fig. 9). The layout of the laser room is sketched in figure 10. The laser system components, which are shown in the photographs in figure 11, include a 6-W argon-ion laser, a power supply, a remote control module, a heat exchanger for laser cooling, and a city water supply for heat exchanger cooling. (Note that fig. 11(e) is from the 7- by 10-Foot HST and that it more clearly shows the city water supply system.) A higher power laser was selected for use in the 8-Foot TPT and the 7- by 10-Foot HST on the basis of previous LVS wind tunnel testing by NASA (refs. 7 through 9 and 11). The level of water vapor condensate about any model depends on the wind tunnel test conditions and the associated flow field generated by the model. A strong leading-edge vortex shed from the wing of a fighter aircraft model, for example, induces large changes in local pressure, temperature, and relative humidity (ref. 15). Lower laser output power is required to illuminate features of the flow under these conditions. A transport model flow field may be characterized by less dramatic changes in the local flow conditions; therefore, this situation requires higher laser power to extract useful flow visualization information. NASA testing conducted in the 6- by 6-Foot Supersonic Wind Tunnel at the Ames Research Center (ref. 8) and the 7- by 10-Foot TT at the DTRC (refs. 7, 9, and 11) on generic and specific fighter aircraft models showed that laser output power from approximately 0.5 W to 5 W was required to provide adequate flow visualization at subsonic through supersonic speeds. Note that the specific application determines the selection of the laser. The laser optics are configured for all-spectral-lines, multimode operation to maximize output power. The laser head is positioned on an optical table mounted to four pneumatic vibration-isolation legs. This setup minimizes the effect of tunnel vibration on the laser optical alignment. The remote module features a 50-ft electronics cable extension to allow the control of the laser from a location such as the wind tunnel control room. The laser cooling water system consists of the heat exchanger with an internal 5-gal reservoir of deionized and deoxygenated water. The heat exchanger provides cooling water in a closed loop to the laser head. Cooling of the 5-gal reservoir is accomplished by routing city water to the heat exchanger. The city water is pumped into a 50-gal reservoir. The discharge flow from the 50-gal reservoir to the heat exchanger is augmented by a 1-hp pump. The city water supply is an open-loop system, and it is drained after thermal contact with the heat exchanger. The laser system features several safety interlocks among the city water supply, the heat exchanger, the laser room entry door, and the laser power supply to safeguard personnel and equipment. In addition, a voltage monitor unit continuously monitors the facility three-phase voltage supply to the laser room. An audible alarm system in the wind tunnel control room alerts the laser operator if the facility voltage supply is outside a specified range, as would occur in a power "brown-out" or over-voltage situation. The laser beam is contained in an armored fiber optic cable (fig. 11(a)) which penetrates the optically sealed plenum shell. As a result, the operating environment in the laser room is free of exposed laser radiation.

The photographs in figure 12 show the penetration of the fiber optic cable into the plenum region through an aluminum porthole blank installed in the plenum shell (fig. 12(a)). The armored fiber optic cable is contained in copper tubing for strain relief. The copper tubing is supported by a U-channel (fig. 12(a)) extending from the inside surface of the plenum shell to the top of the wind tunnel test section. The fiber optic cable and copper tubing assembly is then routed to a box beam in the test section ceiling (fig. 12(b)) which contains the light-sheet-generating optics. Note that the control room observation windows shown in figure 12(a) are optically sealed by metal shutters during laser operation.

The fiber-optic-based beam delivery system contains five principal components: laser-to-fiber coupler, armored fiber optic cable, remote line projector, scanning mirror, and motor controller. The components are shown in the photographs in figure 13, and they are sketched in figure 14. The system is designed to be used with virtually any argon-ion laser operating in either CW or multimode with beam diameters of 0.0315 in. to 0.0709 in. The beam is directed into

the fiber core via the laser-to-fiber coupler (fig. 15). This coupler has four knobs that provide vertical, horizontal, and angular adjustments of the beam relative to the fiber core. The range of vertical and horizontal adjustments is ± 0.05 in., and the angular adjustment range is $\pm 3°$. A small/miniature/type A (SMA) connector is used to anchor the fiber optic cable to the laser-to-fiber coupler as well as to house a focusing lens.

As indicated in reference 16, optical fibers are circular dielectric waveguides that can transport optical energy and information. In the present application, the objective is to transport optical energy as efficiently as possible. The optical fibers have a central core surrounded by a concentric cladding. The refractive index of the core is approximately 1 percent higher than the refractive index of the outer cladding. As a result, light will be confined to the core if the angular condition for total internal reflectance is satisfied (ref. 10). The cladding and the core are encased in a jacket and an armored sheath for protection. A multimode step-index fiber with fused silica core is used in the LaRC systems. The numerical aperture of the fiber is 0.22. Multimode step-index fibers have a 50- to 1000-μm-diameter core with a constant refractive index. The LaRC optical fibers have a 200-μm core diameter. This class of optical fibers is inexpensive, and their large core diameter is desirable for ease of use and good light collection efficiency. These fibers also provide a high-quality light sheet by forming a homogeneous beam at the output end of the fiber. The numerical aperture of the fiber refers to the sine of the half angle of the cone of light which enters or exits the fiber ends multiplied by the refractive index of the medium in which the cone is located. In the present case, the refractive index is 1. The numerical aperture can also be viewed as the largest angle that an incident ray can have for total internal reflectance in the core (ref. 16). A higher numerical aperture fiber features better light-gathering ability and facilitates coupling of light into the fiber. The cable length is 60 ft in the 8-Foot TPT. A 30-ft long cable is used in the 7- by 10-Foot HST because of the smaller plenum diameter and reduced distance from the laser head to the light-sheet optics. The fiber cable length is specific to the test facility and is determined by the proximity of the laser head to the test section and the required cable routing.

Alignment of the laser beam with respect to the fiber core is accomplished by connecting the output end of the fiber optic cable to a detector head and laser power meter assembly (fig. 16). The laser output power during the preliminary alignment is limited to 0.5 W or less. Operation at higher out-put power levels with an initially misaligned beam can scorch the outer sheathing and cause permanent damage to the fiber core. Beam alignment is obtained by adjusting the four translation and rotation knobs on the laser-to-fiber coupler in sequence until the output reading on the power meter is maximized. A throughput (the ratio of power out to power in) of 75 percent to 80 percent is typical and depends on the fiber optic cable length and the condition of the fiber. Figure 17(a) illustrates the transmission loss, or attenuation, in decibels versus the fiber optic cable length using the manufacturer's specification of 0.0073 dB/ft attenuation through a 0.22 numerical aperture fiber. The laser throughput can be estimated using the following relationship from reference 10:

$$\text{Attenuation} = -10 \log_{10} \left(\frac{\text{Power out}}{\text{Power in}} \right) \quad (1)$$

$$\frac{\text{Power out}}{\text{Power in}} = 10^{-[0.1(\text{Attenuation})]} \quad (2)$$

Figure 17(b) shows the effect of fiber optic cable length on the throughput. Additional sources of transmission loss are from the two ends of the fiber and from the front and back surfaces of the focusing lens in the fiber coupler. Laboratory testing at Aerometrics, Inc., Sunnyvale, California, indicates that a loss of approximately 4 percent is incurred through each end of the fiber. The transmission loss through the focusing lens can be reduced to approximately 2 percent per side by applying a suitable anti-reflective coating. These additional losses are accounted for in the second curve in figure 17(b). The actual throughputs achieved in the initial testing in the 7- by 10-Foot HST and the 8-Foot TPT at LaRC using 30-ft and 60-ft cables, respectively, and in the 7- by 10-Foot TT at the DTRC using a 150-ft cable (ref. 11) are also shown in figure 17(b). The actual throughputs for the 30-ft and 60-ft cables are very close to the estimates. The lower throughput of the 150-ft cable is probably the result of manufacturing flaws in the fiber end connections. The 150-ft cable was a "first-generation" cable fabricated for the DRTC testing prior to the development of the LaRC systems. Periodic checks of the throughputs of the 30-ft and 60-ft cables since 1990 have shown a decrease of approximately 1 percent per year. This decrease may be caused by microbending in the fiber core arising from frequent handling of the cable ends. Some deterioration of the fiber end faces may also be caused by a periodic cleaning process using lapping film and methanol.

Experience has shown that the laser-to-fiber coupler alignment is maintained indefinitely and is insensitive to large vibrations caused by wind tunnel operation at high subsonic and transonic speeds. This characteristic significantly improves the productivity of LVS flow visualization testing.

Test results at Aerometrics, Inc., show that the fiber optic cable can accept a beam with a maximum output power of 20 W. The maximum output power of the lasers used in the 8-Foot TPT and the 7- by 10-Foot HST is typically 10 W. Laser-to-fiber coupler alignment has been conducted to the maximum power without incident.

The output end of the fiber optic cable is anchored to the remote line projector unit using an SMA connector. The line projector is a compact, self-contained unit that generates the light sheet and provides control of the sheet divergence (spread angle) and sheet focus (thickness). The unit is portable, and it can be positioned wherever there is optical access to the test section. A ceiling location was selected in both wind tunnels to provide maximum illumination of the model upper-surface flow field. The line projector unit is installed in a window that is 4 in. wide and 16 in. long in the 8-Foot TPT and in a window that is 9.38 in. wide and 47.38 in. long in the 7- by 10-Foot HST. The unit can be positioned in any of three identical windows along the centerline of the 8-Foot TPT ceiling, depending on the model length and location in the test section. The unit can be positioned anywhere in the longer window of the 7- by 10-Foot HST or in a second window that has the same dimensions farther forward in the test section. The line projector optics consist of a three-lens system (fig. 18) featuring an achromatic doublet lens and two identical plano-cylindrical lenses. The output of the fiber optics in the present systems is an extended luminous source as opposed to a point source of light. Because of this characteristic, the diverging output of the fiber cannot be truly focused but only imaged to a waist. The imaging is accomplished using a special two-element lens, or an achromatic doublet. The 3.15-in. focal length achromatic lens also corrects for coma and cancels chromatic aberration (ref. 16). Translation of the achromatic lens relative to the plano-cylindrical lenses controls the laser light-sheet thickness, or focus (fig. 19(a)). The minimum thickness at the model surface is approximately 0.06 in. Refocusing is required at all model stations and model pitch attitudes. In practice, however, the minimum light-sheet thickness is obtained at a selected combination of model station and pitch angle, and refocusing of the light sheet is performed as needed during the testing. A thin light sheet is preferred because it provides better clarity of the flow features. This clarity is particularly important when viewing cross-flow details where the flow structure changes rapidly in a streamwise direction along the wing. For this reason, cross-flow images obtained using a thick light sheet may appear smeared. NASA testing suggests that fiber optics reduce the thickness of the light sheet at the model compared with a mirror-based beam delivery system in which the laser beam is unassisted or freely expanding. The plano-cylindrical lenses produce magnification or focus in one direction only (fig. 19(b)). The light-sheet divergence, or spread, is controlled through the use of two cylindrical lenses in tandem. By translating the first cylindrical lens relative to the second, fixed lens (fig. 19), the sheet half angle can be varied from 4° to 55°. To reduce back reflections, an anti-reflection coating is applied to the two exposed surfaces of each lens. The line projector optics are enclosed within a cylindrical cover to protect the lens surfaces and the end face of the fiber optic cable from airborne contaminants. Contaminants settling onto the end of the fiber optics can cause local scorching and may ultimately lead to the destruction of the fiber core.

Fore and aft scanning of the light sheet is produced by a 3- by 3-in. plane mirror positioned near the output end of the line projector (figs. 13(c) and 14). The mirror is mounted onto a rotational stage with 360° of continuous rotation. The mirror directs the light sheet through a glass window located along the centerline of the test section ceiling and to the desired station on the model. The light-sheet optics are located in the ceiling window at the beginning of a test such that the light sheet is perpendicular to the model surface at a selected model station and pitch angle. Because the light sheet sweeps in an arc along the model, it is generally nonorthogonal with respect to the model surface at all other conditions.

The motor controller (figs. 13(d) and 14) provides the light-sheet focus (thickness), divergence (spread), and sweep control from a remote station, which is usually the wind tunnel control room. The focus control is varied until the thickness of the light sheet projected onto the model surface is minimum. The light-sheet divergence is also "tailored" to the model, and it typically spans from wing tip to wing tip. The light-sheet characteristics are observed on a video monitor because the test area is optically sealed. The light sheet can be scanned continuously from the model nose to a position downstream of the model base, or it can be fixed at any desired model station. Model stations are typically identified using white correction fluid applied in thin, narrow

strips perpendicular to the model centerline. These identifier marks flash prominently during testing as the laser light sheet passes each station.

Vapor screen flow visualization is made possible by injecting water into the diffuser section of the wind tunnel circuit. A 150-gal tank of deionized water is located in a room atop the plenum shell of the 8-Foot TPT (fig. 9). A solenoid switch and a 1-hp pump positioned on the discharge side of the water tank are activated from the wind tunnel control room. The switch and the pump route the water through a high-pressure hose that penetrates the plenum shell. The water is directed to a manifold and then to an array of six atomizer spray nozzles installed in the ceiling of the wind tunnel diffuser (fig. 9). The nozzles emit full-cone spray patterns that encompass most of the diffuser cross section under static (wind-off) conditions. The diffuser section was selected because of the relatively high cross flow relative to the injected spray patterns that would assist in the atomization of the water particles. A video camera was installed during the initial LVS testing in the 8-Foot TPT to view the interaction of the diffuser flow and the water spray patterns. The camera was located in the floor of the tunnel just downstream of the arc sector (fig. 9) and viewed through a window along the floor centerline. The results were inconclusive, however, regarding the coverage and plumes of the spray patterns or whether the injected water particles vaporized in the diffuser. Incomplete vaporization is a concern because of possible water impact and erosion damage to the fiberglass fan blades in the 8-Foot TPT and the wooden fan blades in the 7- by 10-Foot HST. As a safeguard, the leading edges of the blades have been treated with a special erosion coating. The 8-Foot TPT dryer system is used immediately after the flow visualization to safeguard the facility electronic equipment and to reduce the risk of corrosion to the tunnel structure. A two-unit dryer system using silica gel as the dessicant is employed (ref. 12). Each unit has the capacity of 2500 ft^3/min at pressures up to 4 atm. The air output from the dryer has a dew point not exceeding $-70°\text{F}$. For initial drying of the tunnel and rapid drying of the test section and surrounding tank, a 10 000 ft^3/min compressor of compression ratio 4 is provided. Qualitative guidelines that help to establish the amount of water injection necessary for suitable flow visualization are shown by the onset of a visible plane of light in the test section or a local condensation within the vortex flows about the model. The LVS flow visualization is typically conducted in the 8-Foot TPT at free-stream Mach numbers from 0.60 to 1.20. Up to 25 gal of water may be required at $M_\infty = 0.60$ to achieve ade-

quate flow visualization for a range of angle of attack. This quantity diminishes to approximately 5 gal at $M_\infty = 1.20$. The approximate volume of the 8-Foot TPT circuit is 370 000 ft^3. Note that the required water injection will also depend on the flow field generated by the model. Relative humidity levels are determined in the 7- by 10-Foot HST from hygrometer measurements made in the settling chamber of the tunnel. The capability to conduct similar measurements in the 8-Foot TPT is a planned upgrade. These measurements provide an indication of (1) the possible need to inject water and (2) the efficiency of the water injection system to increase the humidity. In many applications where a model generates strong vortical flows, relative humidity levels measured in the settling chamber of the 7- by 10-Foot HST as low as 30 percent are sufficient to yield satisfactory flow visualization. The vortices can induce significant increases in the local relative humidity (ref. 15), and can thereby cause local condensation even at very low free-stream relative humidity levels. Water injection is frequently unnecessary in the 7- by 10-Foot HST. This facility exchanges up to 10 percent of the tunnel airflow by volume with the outside air. Exchange with humid outside air is often sufficient to increase the relative humidity in the test section to acceptable levels for flow visualization. As a result, LVS flow visualization has frequently been obtained on vortex-dominated models at M_∞ as low as 0.20 and up to $M_\infty = 0.85$ without water injection. The LVS flow visualization has been performed concurrently with the measurements of the model surface static pressures and forces and moments. However, this procedure has been employed only at subsonic speeds for models that develop strong vortex flows at high angles of attack. Experience has shown that model surface static pressures and force and moment data are unaffected by varying humidity levels where the flow field is dominated by vortices. Test data in reference 9 show that increased relative humidity has no observable effect on forebody and wing LEX surface static pressures and total forces and moments on an F/A-18 configuration at $M_\infty = 0.60$ and high angles of attack. In this case, water was injected into the settling chamber of the tunnel in a sufficient quantity to cause local condensation within the strong LEX vortices. The weaker forebody vortices were not visible. This procedure is not recommended on models that are dominated by attached flow or that develop shock waves at transonic and supersonic speeds because of the adverse effect of a "moist" tunnel on the boundary layer and shock behavior.

Observation and documentation of the laser light-sheet characteristics during the alignment process

and of the model flow field revealed by the laser light sheet during tunnel operation are accomplished exclusively with color video-based systems. A miniature video camera that has 360 television lines of horizontal resolution and a fixed focal length lens (fig. 20) is contained in a cylindrical housing that is mounted onto the model sting support system (fig. 9). This camera provides a perspective aft of the model which looks upstream along the model centerline. The video image perspective remains constant throughout the pitch angle range because there is no relative motion between the camera and the model. The video image perspective does change, however, throughout yaw angle and roll angle ranges. A second video camera (fig. 21) with 560 television lines of horizontal resolution and a variable focal-length lens is located outside the test section in approximately a right three-quarter rear position (fig. 9). The lens focal length, the focus, and the iris are remotely controlled. The camera head is mounted to a tilt/pan table that features remotely controlled angular displacement about two axes. Each camera is connected to a color video monitor and videocassette recorder. Title generators interface with the wind tunnel data acquisition system and provide real-time test conditions superimposed on the video images. Hard copies of any selected recorded video frame or real-time image are obtained using a color video printer unit. This unit allows the acquisition of only single frames. Digital cameras combined with imaging enhancement tools offer a significant improvement to the resolution obtained with the present video camera system. Still photography is available in the 8-Foot TPT and the 7- by 10-Foot HST. However, this capability has not been employed during LVS operation. The size of a still camera and its protective housing is prohibitive for installation on the model support system because of the flow disturbances that may propagate upstream to the model. A still camera mounted outside the test section is inaccessible for adjustments during tunnel operation to account for varying light levels or the movement of the model through the test section caused by varying pitch, roll, and yaw angles.

The fiber optics, the optically sealed plenum shell, and the video-based equipment provide an LVS system that isolates the user from the laser beam and from the laser light sheet during all phases of its operation. Application has shown that approximately 5 min are required to bring the LVS system on-line for observation and documentation of the flow field. The training required to operate the LVS systems is minimal. Furthermore, a single user can operate the entire LVS system. The laser remote module, the line projector and scanning mirror motor controller, the

camera controls, the video monitors and recorders, and the title generators are consolidated at a work station in the wind tunnel control room.

Representative LVS Results

The 7- by 10-Foot HST fiber-optic-based LVS system became operational in January 1990, whereas the 8-Foot TPT system was used for the first time in March 1990. Figure 22 presents planform sketches of several models that have been tested since 1990 in LaRC wind tunnels in conjunction with the LVS flow visualization technique. Representative LVS results obtained on these models are presented in figures 23 through 29. The test conditions correspond to free-stream Mach numbers from 0.40 to 1.20, tunnel total pressures ranging from approximately 0.25 atm to 1.0 atm, tunnel total temperatures from approximately 60°F to 100°F, and angles of attack between 9° and 22°. Whenever possible, LVS flow visualization is conducted at tunnel total temperatures of 100°F or less. The flow visualization quality diminishes at higher operating temperatures. Hot tunnel air can contain more water vapor before condensation occurs. As a result, greater quantities of water are required to promote condensation. Under these conditions, condensation can occur in the free stream as well as locally within the vortical flows. This condensation pattern provides a poor contrast and correspondingly decreases the flow details. The models are typically painted with a flat black paint to reduce glare and to increase the contrast between the illuminated cross-flow patterns and the model surface.

The first LVS results in the 7- by 10-Foot HST were obtained using a generalized fighter model featuring chine-like forebody strakes and a 55° cropped delta wing (figs. 22(a) and 23). The LVS photographs in figure 23 correspond to $M_\infty = 0.40$, $\alpha = 20°$, and two selected stations along the wing. The perspective is from a right, three-quarter rear position. Tunnel airflow exchange with humid outside air increased the relative humidity in the test section so that local condensation occurred in the vortex flows. Water was not injected through the atomizer nozzles in the diffuser section during this test. The strake and wing vortices are visible as regions of high scattered light with approximately circular cross section surrounding hollow cores. The interaction of the strake and wing vortices and the breakdown of the wing vortical flow are illustrated in figure 23(c). Onset of vortex breakdown is apparent in the real-time LVS images by the appearance of condensed water vapor in the core of the vortex and an expansion and unsteadiness of the vortex cross section. A laser output power of 1 W was sufficient to produce the

results shown in figure 23. This laser output power produces approximately 0.80 W at the output end of the fiber optic cable. The same model was tested in the 7- by 10-Foot TT (ref. 7) at the DTRC at $M_\infty = 0.40$ using a mirror-based beam delivery system. These preliminary results suggested that the fiber-optic-based LVS system provides a thinner and more uniform light sheet, yields flow features at lower laser output power, and is safer and more reliable compared with a mirror-based system.

The LVS results obtained in the 7- by 10-Foot HST at $M_\infty = 0.50$ and $\alpha = 25°$ on a $65°$ cropped delta wing model (fig. 22(b)) with LEX and twin canted tails are shown in figure 24. An objective of this test was to determine the effect of vertical tail cant angle δ_v on the vortex flow behavior and the overall aerodynamic and stability characteristics. The cant angle is measured relative to the wing surface normal and is positive outward. The photographs depict the cross sections of wing and LEX vortices observed from a three-quarter right rear position (figs. 24(a) through 24(d)) and from a position aft of the model which looks upstream along the model centerline (figs. 24(e) through 24(h)). The mutual interaction of wing and LEX vortices and the vortex interaction with the twin tails canted to $30°$ are shown in figures 24(a) through 24(f). The vortex-vortex and vortex-tail interactions in sideslip are revealed in figures 24(g) and 24(h). Note that a combination of model pitch and roll angles is used in this test to provide the desired angles of attack and sideslip. A typical application of LVS flow visualization is to assist in the interpretation of the model surface static-pressure distributions and six-component forces and moments in figures 24(i) through 24(k). The effect of δ_v on the right wing upper-surface pressure distributions at $M_\infty = 0.50$ and $\alpha = 25°$ is shown in figure 24(i). The spanwise pressure distributions display a single suction peak at all three model stations despite the presence of two primary vortices (i.e., data corresponding to $\delta_v = 30°$ which are shown by the square symbols). The LVS flow visualization near $x/c = 0.30$ (fig. 24(a)) indicates that the suction peak near the leading edge is caused by the wing vortex, while the LEX vortex is too high above the surface to induce a direct suction peak. The LVS result near the tail (fig. 24(c)) indicates that LEX and wing vortices are coiled about each other with the wing vortex situated directly above the LEX vortex. This flow situation is consistent with the single suction peak in the spanwise pressure distributions at $x/c = 0.80$. The tails canted to $30°$ are situated in the path of the interacting vortices (fig. 24(e)). This cant angle causes

an upward displacement of the vortices from the wing surface, which can be inferred from the LVS photographs at two stations along the tails in figures 24(c) through 24(f). Test results (not shown) also indicate that the tails canted outward $30°$ cause an early breakdown of the vortical flows. The vortex displacement diminishes the vortex-induced pressure signatures at $x/c = 0.60$ and 0.80 (fig. 24(i)) compared with the results obtained at the other cant angles. The diminished vortex-induced suction pressures and early vortex breakdown cause a reduction in lift, increased drag, and increased nose-up pitching moment as shown in figure 24(j). In sideslip, the tails canted to $30°$ promote vortex breakdown asymmetry. This asymmetry is shown in figures 24(g) and 24(h) at $\beta = 5°$. The photograph in figure 24(h) shows that vortex breakdown occurs at the windward tail (i.e., the right side in the photograph), while the vortices are stable and pass outboard of the tail on the leeward (left) side. This vortex-tail interaction causes an unstable break in the static lateral stability derivative C_{l_β} (fig. 24(k)) at an earlier angle of attack compared with the model that has other tail cant angles. The photograph in figure 24(h) suggests that the leeward tail is embedded in a favorable vortex flow field. The vortex-induced suction pressures on the outside surface of the leeward tail promote a negative increment to C_{Y_β} (i.e., negative side force acting to the left; fig. 24(k)) and a corresponding stable increment to the directional stability derivative C_{n_β}.

The LEX vortex flows about a 0.06-scale model of the U.S. Navy/McDonnell Douglas Corporation/Northrop Corporation F/A-18 (fig. 22(c)) at $M_\infty = 0.45$ and $\alpha = 20°$ are illustrated in figure 25. The LVS images correspond to a view aft of the model looking upstream along the model centerline. This experiment provided information on the LEX vortex flow behavior and vortex-tail interactions compared with flight and CFD results obtained in an on-going NASA High-Alpha Technology Program (ref. 17). Reference 9 shows that the LEX vortex breakdown characteristics observed in LVS wind tunnel testing of a 0.06-scale F/A-18 model compare well with in-flight flow visualization results obtained on the full-scale F/A-18 (ref. 18).

The flow features obtained in the 7- by 10-Foot HST at $M_\infty = 0.50$ and $\alpha = 20°$ and in the 8-Foot TPT at $M_\infty = 1.20$ and $\alpha = 20°$ on a generalized Northrop fighter configuration with outboard control surface (OCS) (fig. 22(d)) are shown in figure 26. The photographs reveal the combined wing and OCS leading-edge vortices in the near wake of the model. Symmetric and differential deflections of the OCS

panels were tested to determine their effectiveness as pitch, roll, and yaw control devices. The left-hand OCS panel was intrumented with a three-component strain-gauge balance to measure OCS normal force, bending moment, and hinge moment. The LVS flow visualization was particularly useful in evaluating the induced effects of wing and OCS vortices on OCS force and moment characteristics.

Figure 27 shows the vortex flows about a generalized supersonic fighter/interceptor model (fig. 22(e)) tested in the 8-Foot TPT and observed from the model support system. The photograph in figure 27(a) corresponds to $M_\infty = 0.85$ and $\alpha = 18°$ and reveals the vortices shed from the leading edges of the highly swept wings. Figure 27(b) illustrates the tip vortices from the horizontal tails and the wake from the wing-mounted engine nacelles at $M_\infty = 1.19$ and $\alpha = 9°$. Figures 27(c) and 27(d) illustrate the complexity of the cross flow in the near wake of the model at $M_\infty = 1.19$, $\alpha = 18°$, and $\beta = 8°$ and $-8°$, respectively. The LVS results assisted in the evaluation of a new aircraft design and provided flow-field features to guide CFD computations.

The complex vortex flow-field interactions about a variable-sweep fighter/bomber model (fig. 22(f)) are illustrated in the LVS photographs in figure 28. The flow visualization was conducted in the 8-Foot TPT at Mach numbers of 0.85 and 1.20. The perspective of the LVS images is aft of the model looking upstream along the model centerline. The photographs in figures 28(a) and 28(b) correspond to $M_\infty = 0.85$, $\alpha = 18°$, and $\beta = 0°$ and $-4°$, respectively, at a light-sheet location near the base of the model. The wing leading-edge sweep is approximately 71°, which is shown by the dashed lines in the planform sketch (fig. 22(f)). The vortices shed from forebody, engine inlets, wing gloves, and wing leading edges interact and form a complex cross-flow pattern near the model base. Nonuniform temperature distribution in the tunnel test section caused the vortices on the right side of the model to be brighter compared with those on the left side of the model, as shown in figure 28(a). Partial obstruction in the water flow through the tunnel cooling coils was identified as the source of the nonuniform temperature distribution. The flow-field interactions are also complex at higher Mach numbers. The photographs in figures 28(c) and 28(d) were obtained at $M_\infty = 1.20$, $\alpha = 22°$, and $\beta = 0°$ and $-8°$, respectively. The dark areas above the wings define vortex regions from engine inlet, wing glove, wing leading edge, and horizontal tail. The bright lines of condensation near the centerline vertical tail are caused by high flow veloc-

ities induced by the vortical flows. Condensation of water vapor in the free stream provides good definition of the outer edges of the laser light sheet in figures 28(c) and 28(d). The LVS results were used in the evaluation of aerodynamic, stability, and control characteristics of this aircraft configuration for a wide range of simulated flight conditions.

The wing leading-edge vortex cross sections in the wake region of a generic high-speed civil transport (HSCT) model (fig. 22(g)) at $M_\infty = 0.90$ and $\alpha = 9°$ are shown in figure 29. The flow visualization was performed in the 8-Foot TPT to assess the aerodynamics of a supersonic transport configuration at off-design conditions and to compare CFD-computed flow fields.

Concluding Remarks

Laser vapor screen (LVS) flow visualization systems that are fiber-optic based have been developed and installed for aerodynamic research in the Langley 8-Foot Transonic Pressure Tunnel and the Langley 7- by 10-Foot High-Speed Tunnel. These facilities feature a plenum shell that surrounds the test section and an operating environment within the plenum that poses severe operational concerns for a laser source. The use of fiber optics allows the laser source to be located outside the plenum and simultaneously provides a safe and reliable means of delivering the laser beam over a significant distance to the light-sheet-generating optics inside the plenum. The Langley Research Center LVS systems expand the use of fiber optics in conjunction with a laser light-sheet flow visualization method to larger scale subsonic and transonic facilities that have limited access to the test section and the harsh operating environments for laser-based systems. The LVS systems have been effectively used to visualize the vortex-dominated flows about numerous advanced aircraft configurations at low subsonic through supersonic speeds. Experience has shown that the LVS method works well when the local flow is in the compressible regime. The high local velocities induced by vortical flows, for example, promote good condensation patterns even at low subsonic free-stream speeds. The flow visualization results complement the model force and moment and surface static pressure measurements that are typically obtained in wind tunnel tests. The LVS results also improve the understanding of trends in aerodynamic, stability, and control characteristics.

Results from 3 years of operating experience in the Langley Research Center wind tunnels suggest that the use of fiber optics yields a thinner and more uniform light sheet and requires lower laser output power to achieve satisfactory flow features compared

with a free-expanding laser beam steered by mirrors. The alignment of the laser beam to the fiber optic core is maintained indefinitely. In addition, the fiber optic system is insensitive to large vibrations caused by tunnel operation at high speeds and to variations in tunnel temperature and pressure. These features increase wind tunnel productivity by decreasing setup time and eliminating problems during operation. The compactness of the fiber optics and light-sheet-generating package facilitates the installation and the implementation of LVS systems in larger scale wind tunnel facilities. Most importantly, the use of fiber optics represents a significant advancement in laser safety.

NASA Langley Research Center
Hampton, VA 23681-0001
November 2, 1993

References

1. Allen, H. Julian; and Perkins, Edward W.: *A Study of Effects of Viscosity on Flow Over Slender Inclined Bodies of Revolution.* NACA Rep. 1048, 1951. (Supersedes NACA TN 2044.)

2. McGregor, I.: The Vapor-Screen Method of Flow Visualization. *J. Fluid Mech.*, vol. 11, pt. 4, Dec. 1961, pp. 481–511.

3. Keener, Earl R.: *Flow-Separation Patterns on Symmetric Forebodies.* NASA TM-86016, 1986.

4. Verhaagen, N. G.: An Experimental Investigation of the Vortex Flow Over Delta and Double-Delta Wings at Low Speed. *Aerodynamics of Vortical Type Flows in Three Dimensions*, AGARD-CP-342, July 1983, pp. 7-1–7-16.

5. Payne, F. M.; Ng, T. T.; Nelson, R. C.; and Schiff, L. B.: Visualization and Flow Surveys of the Leading Edge Vortex Structure on Delta Wing Planforms. AIAA-86-0330, Jan. 1986.

6. Kjelgaard, Scott O.; Sellers, William L., III; and Weston, Robert P.: Flowfield Survey Over a 75° Swept Delta Wing at an Angle of Attack of 20.5°. AIAA-86-1775, June 1986.

7. Erickson, Gary E.; and Rogers, Lawrence W.: *Effects of Forebody Strakes and Mach Number on Overall Aerodynamic Characteristics of Configuration With 55° Cropped Delta Wing.* NASA TP-3253, 1992.

8. Erickson, Gary E.: *Wind Tunnel Investigation of the Interaction and Breakdown Characteristics of Slender-Wing Vortices at Subsonic, Transonic, and Supersonic Speeds.* NASA TP-3114, 1991.

9. Erickson, Gary E.: *Wind Tunnel Investigation of Vortex Flows on F/A-18 at Subsonic Through Transonic Speeds.* NASA TP-3111, 1991.

10. Hecht, Jeff: *Understanding Fiber Optics.* Howard W. Sams & Co., 1987.

11. Erickson, Gary E.; and Murri, Daniel G.: Forebody Strakes for High-Angle-of-Attack Vortex Flow Control: Mach Number and Strake Planform Effects. *High-Angle-of-Attack Technology*, Volume I, Joseph R. Chambers, William P. Gilbert, and Luat T. Nguyen, eds., NASA CP-3149, Part 1, 1992, pp. 381–480.

12. Staff, Performance Aerodynamics Section: *A Description of the NASA-Langley Eight-Foot Transonic Pressure Tunnel.* NASA Langley Research Center, Nov. 1973.

13. Fox, Charles H., Jr.; and Huffman, Jarrett K.: *Calibration and Test Capabilities of the Langley 7- by 10-Foot High Speed Tunnel.* NASA TM X-74027, 1977.

14. *Nonionizing Radiation.* LHB 1710.8, NASA Langley Research Center, Sept. 1982.

15. Campbell, James F.; Chambers, Joseph R.; and Rumsey, Christopher L.: Observation of Airplane Flow Fields by Natural Condensation Effects. AIAA-88-0191, Jan. 1988.

16. *Precision Laser & Optics Products.* Newport Corp., c.1989.

17. Gilbert, William P.; and Gatlin, Donald H.: Review of the NASA High-Alpha Technology Program. *High-Angle-of-Attack Technology*, Volume I, Joseph R. Chambers, William P. Gilbert, and Luat T. Nguyen, eds., NASA CP-3149, Part 1, 1992, pp. 23-59.

18. Fisher, David F.; Del Frate, John H.; and Richwine, David M.: *In-Flight Flow Visualization Characteristics of the NASA F-18 High Alpha Research Vehicle at High Angles of Attack.* NASA TM-4193, 1990.